The role of mergers in the formation of boxy galaxies

A Master's Thesis

presented for a Master's Degree

in

Theoretical Physics

from the

Universität Zürich

by

Rebekka Bieri

Supervised by

Prof. Dr. Benjamin Moore
Dr. Romain Teyssier
Dr. Davide Martizzi

Zürich 2013

Contents

Place a rubber duck on your monitor and describe your problems to it. There is something magical about stating your problems aloud that makes the solution more clear[1]

My trusted rubber duck would sometimes even nod or say a few words.

[1] Also called **Rubber Ducking**. From 'The Pragmatic Programmer: From Journeyman to Master rubber ducking.'

Acknowledgements

Firstly, I would like to thank **Ben Moore** for giving me the opportunity to work on this project. One of Ben's first decision was assign the direct supervision of **Davide Martizzi**. This was one of the best decisions ever made regarding this thesis. I owe Ben a great deal more, but since he knows it I am not going to go into further detail. I would like to thank him for his support and also the trust he has given me. I also would like to thank **Romain Teyssier** who has provided constant support and help, especially for questions related to the code used in this thesis, but also for his general open ear and eye for various other problems—often until late at night. If something is suspicious Romain is the guy to detect it and very often solve it. My daily man was **Davide Martizzi**. He is a hero! I stopped counting the number of times per day I came into his office to ask various questions. I guess our e-mail exchange while he was away at a conference that peaked at about 50 e-mails in one day is pretty epic (feedback mechanism we beat you...). His patient support, his sharing joy when I was happy about something and his moral support when I was less happy is deeply valued. I think we have been a great team! Related to this I would also thank and apologise to his office mates **Volker bla** for enduring me during my visits to the office. I also have to thank **Markus Wetzstein**, a temporarily office mate of Davide. That his computer was broken and that he needed to stay in Davide's office was a lucky strike. Without him, Davide and I would probably still sitting at the office table trying to debug the initial condition code and figure out what on earth was going wrong. His knowledge into the deep deep pond of FORTRAN helped to proceed with this thesis. I also have to thank him however for letting me stay at his place a few times and supporting me while writing up this thesis. I thank **Andreas Bleuler** for answering my various PYMSES related questions; **Doug Potter** without whom this Institute would not run at all and who answered my thousand e-mails regarding the many computer and hardware problems I came across; **Regina Schmidt** for being the angel of the Institute. Her uncomplicated support, positive outlook on life, and her ability to move away problems help the whole Institute, including me. I also thank all the various Institute members who help to make this Institute what it is and providing it with this amazing spirit probably unique in the world. I am super grateful to my parents **Barbara**, and **Ueli** as well as my amazing sister **Elisabeth** who constantly supported me during my whole studies and phases while doing so. They also endured my stay at their home at the end stage of this thesis. I also have to thank them for the various times they brought me back to the real world and provided me with a necessary reality check. Without my family I guess I would not have started to study Physics and probably would not have finished one year of studying. And this means very much to me! I am most grateful to my boyfriend **Jonathan Coles**. He provided constant support during this thesis, often late into the night, even after moving away to Paris. He is the best rubber duck I

came across, silently listening to my grumbling about my code, smiling when I figured out the problem on my own, asking some questions or nodding to help me figure out the problem, and sitting down and helping me when nothing of the above worked. I also have to thank him for his amazingly patient correcting of the text of this thesis (probably even parts of this acknowledgement). What else is left to say other than that we work together like Peas and Carrots.

As I tend to get emotional I stop writing this acknowledgements and apologise if I have forgotten anyone.

1. Introduction

The night sky has always fascinated mankind and it comes with no surprise that astronomy is one of the oldest sciences. Prehistoric cultures could only use their imaginations to explain what they saw in the night sky, but it was not until the 16th and 17th century that astronomers like Galilei, Kepler, and later Newton began to develop a mathematical based theories to explain their observations. The concept of galaxies being *rotating bodies of a huge number of stars held together by gravitational forces* was first introduced in 1750 by the English astronomer Thomas Wright and further developed by the German philosopher Immanuel Kant in 1755 who referred to them as *island universes*. The dispute over the nature of what were once named spiral nebulae stands as one of the most significant in the development of astronomy, and can be marked as the beginning of the study of galaxies. The existence of external galaxies outside of our Milky Way was confirmed by Heber D. Curtis, Knut Lundmark and Edwin Hubble in the early 1920s.

Galaxy formation has played an important role in answering questions about structure formation, by providing an observable, natural testing ground for theories about the origin and evolution of the Universe. The modern galaxy formation theory is set within the larger scale cosmological model, where cosmology is the field of astronomy that studies the origin, dynamics, and evolution of the universe. It is an important requirement for any theory of structure formation to reproduce the observed properties of galaxies, such as spatial distribution, stellar properties, and morphology. Within these constraints a theory has emerged in which the formation of structure in the Universe is seeded by tiny perturbations in the primordial cosmic density field which expanded to larger scales by a rapid expansion. The success of that model lies in largely explaining the **cosmic microwave background** (CMB). It makes an assumption that there exists an invisible, collisionless, self-gravitating kind of matter, also called **dark matter**, that strongly affects the gravitational evolution of the Universe. There are many reasons to suspect the existence of dark matter, such as the observed rotation curves of galaxies, gravitational lensing effects, and the velocity distribution of galaxies in clusters. The dark matter component behaves like a collisionless fluid which is often modeled as a pressureless fluid. Fluctuations in the dark matter density field at very early times are assumed to grow because of their self-gravity and then undergo gravitational collapse.

The fully analytical linear theory of cosmological perturbations of dark matter is well understood and provides an accurate description of the early stage of its evolution. Once the evolution leads to complicated structure formation, the linear perturbative calculations break down as the perturbations become non-linear. The only way to study their further evolution is through numerical calculations. Empirical models, together with N-body simulations, show that these perturbations start to cluster to-

gether to form a gravitationally pressure-supported collapsed system called a **halo**. In the standard picture of cosmology it is predicted that small halos form before lager halos, evolving hierarchically to form a network of sheets and chains called the **cosmic web**. Halo mergers and accretion of satellite halos are also thought to play a very important role in shaping the properties of the most massive halos.

Gravity alone does not, however, provide a complete description of the universe. In particularly, dark matter does not interact with the luminous matter we are able to see, other than gravitationally. The luminous matter is generally referred to as **baryonic matter** as leptons provide a negligible contribution to the total mass. It includes standard particles, nucleons, and photons. A combination of experimental measures paint a picture in which the energy density of the Universe is shared between dark energy (68.3%), dark matter (26.8%), and baryonic matter (4.9%). Taking into account the baryons, simulations become even more challenging because of the collisional nature of the baryonic matter as well as the complexity of the physics involved in the processes. From the structure formation point of view it is believed that baryons are dragged along by the gravitationally dominant dark matter and concentrate in the deep potential wells of the halos forming a hot gaseous halo. How much baryonic material the dark matter is able to accrete depends upon the depth of the potential well and the pressure of the baryons. The hot gas in the halo is able to cool down by radiative cooling. The cooling reduces the pressure support and causes the accretion of cold gas from the halo onto a central disc and stars star to form. There are however still many open questions. The role of many feedback mechanisms such as galactic winds, momentum feedback from supernovae, and feedback provided by the accretion of gas onto a supermassive black hole in the center of the galaxy (**AGN**) still has to be explored in greater detail. Also the processes of star formation within the picture of galaxy formation, the baryonic structure and evolution has to be better understood.

A reasonable galaxy formation theory not only has to explain how and where structure arise, it also has to explain the physics involved before star formation and the shape of galaxies. There is an enormous variety of galaxies to be found in nature, from scattered dwarfs to impressive large spirals. The individual structure of a galaxy depends on how it was formed and evolved. The amount of activity taking place inside the galaxy also varies with each galaxy. Where some act like star-producing sites, others have shut down star production long ago. Despite the huge variety of galaxies, the overwhelming majority of bright galaxies exist in one of three main forms, namely, **spiral galaxies** such as our own Milky Way in the shape of a flattened disk hosting a spiral pattern, **lenticular galaxies** also in the shape of a circular disk but hosting a central bulge, and **elliptical galaxies** shaped something like an ellipsoidal football. The remaining few are lumpy and irregular in appearance and are usually categorised as **irregular galaxies**.

In March 2012 a discovery of a rare, rectangular-shaped galaxy (LEDA 074886) was reported (Graham et al., 2012). In addition to being rectangular, LEDA 074886 also features a prominent disk inside it, aligned edge-on to our line-of-sight, and is thought to be a star formation region. This special rectangular galaxy opens questions about its formation. It is already known that mergers play an important role in the formation and evolution of a galaxy. It is suspected that LEDA 074886 is also formed by a

merger of two galaxies. Because of its boxy outer part and discy stellar central region, the galaxy shows characteristics of two types of galaxy mergers. Generally, elliptical galaxies lack the ingredients to form new stars. N-body simulations have shown that boxy shaped galaxies can form by mergers but they generally show little star forming activity. However, simulations have also shown that gas rich mergers usually do not build boxy galaxies, whereas they do have traces of a central star forming region. The purpose of this thesis is to study the role of mergers in the formation of boxy galaxies and to better understand the processes that can lead to a star formation region in the middle of the galaxy.

In this thesis a number of galaxy merger simulations have been performed to try to understand the conditions required to reproduce galaxies like LEDA 074886. In order to make these simulations, and their subsequent analysis, possible, several new software tools were also developed.

In section 2 we introduce in more detail the theoretical basis of cosmology and galaxy formation. We then discuss the observations of LEDA 074886 in section 4. The computational techniques used to perform simulations are described in section 3. Our methods for running the particular simulations of our galaxy mergers are detailed in section 5 and a discussion of the results are provided in section 9. The new computer code that was developed over the course of this work is described in section 7 and the verification tests in section 8. We conclude with a summarising discussion in section 9.

2. Theory

In this Chapter we first describe the theoretical framework which is able to explain the way in which primordial homogeneous and isotropic Universe is able to evolve and form structures. Because dark matter is the main constituent of the cosmic structure it is important to understand how dark matter behaves. It is explained how gravitational instabilities lead to dark matter halos forming a cosmic web, which is important for the stability of galaxies. It then continues to explain the structure and morphology of the Galaxies. A special emphasis is made in explaining the gravitational interaction of the Galaxies as results discussed in those sections are used to set up the simulations done for this thesis.

2.1. From Cosmological Perturbations to the Formation of Dark Matter Halos

Broadly speaking, the Universe consists of an immensely varied array of galaxies, nebulae, and other baryonic objects. The distribution of this structure is clearly inhomogeneous and anisotropic. However, on scales larger than 100 h^{-1} Mpc we will assume that the Universe is actually homogeneous and isotropic. Under these assumptions, also known as the **Copernican principle**, the universe looks the same irrespective of the location and direction in which one looks. The **Einsteins field equations**

$$G_{\mu\nu} + \Lambda g_{\mu\nu} = 8\pi G T_{\mu\nu} \tag{2.1}$$

relate the energy-density tensor $T_{\mu\nu}$ to the Einstein space-time tensor $G_{\mu\nu}$ and a metric $g_{\mu\nu}$. Here we also include a **cosmological constant** Λ to account for the expansion of the Universe. From the assumption of the Copernican principle we can write down the so-called Friedmann, Lamaitre, Robertson, Walker (**FLRW**) metric

$$ds^2 = -dt^2 + a^2(t)\left[\frac{dr^2}{1-Kr^2} + r^2 d\Omega^2\right] \tag{2.2}$$

where a is the scale factor.

From these equations we can already say much about the evolution of the Universe. Combining the Einstein field equations and the FLRW metric we can derive the **Friedmann equations**

$$\frac{\ddot{a}}{a} = -\frac{4\pi G}{3}(\rho + 3p) \tag{2.3}$$

$$\left(\frac{\dot{a}}{a}\right)^2 = \frac{8\pi G}{3}\rho - \frac{K}{a^2} \tag{2.4}$$

where ρ is the energy density, and p is the pressure, which govern the expansion rate of the Universe. The equations can be simplified by defining the **Hubble parameter** $H := \frac{\dot{a}}{a}$. They form the base of our current cosmological model and successfully describe the average expansion of the universe on large scales. In addition, rho can be expressed as a combination of densities corresponding to different components such as photons, dark matter, and dark energy. This model also is successful in describing the evolution of the Universe from a hot, dense initial state dominated by radiation to the cool, low density state dominated by non-relativistic matter and vacuum energy at the present day. This standard model depends upon a few important observational quantities such as the expansion rate $\dot{a}$, the temperature of the present microwave background radiation ($T_{CMB} = 2.75\ K$), the density of visible matter (4.9%), dark matter (26.8%), and dark vacuum energy (68.3%).

Since the assumption of homogeneity is incorrect on small scales owing to the presence of the stars and galaxies in our Universe, there therefore must be small inhomogeneities present at a certain time in the history of our Universe. Observations of the **cosmic microwave background** (CMB) greatly support this idea. The CMB was created at the point where photons stopped interacting with electrons and the opaque Universe became, to first order, transparent to radiation. This event is imprinted in the Universe on the **last scattering surface** or the cosmic microwave background. The photons which were released during this recombination could travel relatively undisturbed through space to us at the present time and cooled down through the expansion of the Universe to give a homogeneous blackbody radiation field with a mean temperature of $T_{CMB} = 2.75\ K$. Small temperature deviations on the order of 10^{-5}K have been observed in the temperature field. These fluctuations are coupled by the Boltzmann equation $\rho \propto T^4$ to perturbations in the matter field which possibly have quantum mechanical origins. The primordial fluctuations are thought to have been amplified to macroscopic scales by a rapid expansion of the Universe known as inflation. Inflation is believed to be produced by the presence of a quantum scalar field slowly rolling down from a false to a true vacuum. While doing so, the field maintains an approximately constant energy density and causes the Universe to expand exponentially for a brief period of time. Current theories of inflation predict the fluctuation field to be distributed as a **Gaussian random** field. In this case, the linear density is completely determined by its power spectrum, or equivalently its two-point correlation function. The primordial power spectrum is assumed to change during the evolution in the early Universe due to various processes such as gravitational collapse, the effects of pressure on particles, and dissipative processes. In general, modes of short wavelength reduce their amplitudes relative to the change of the modes of long wavelengths. This effect can be described with the transfer function, $T(k)$, which gives the ratio of the later-time amplitude of a mode with its initial value:

$$T(k) = \frac{\delta_k(z_0)}{\delta_k(z)D(k)} \tag{2.5}$$

where $D(z)$ is the linear growth factor extrapolated to the present. This, in turn, is

related to the power spectrum though

$$P(k,z) = P_0(k)T^2(k)\frac{D(z)}{D(z_0)}. \tag{2.6}$$

Determining the transfer function is therefore a very valuable and powerful tool for understanding the large scale structures of the Universe. The currently best publicly available code to calculate accurate results of transfer functions is thought to be CMBFAST (Seljak & Zaldarriaga, 1996).

2.1.1. Linear Perturbation Approach

To describe and understand the evolution of the density inhomogeneities at early times a perturbative approach is usually used. In this approach, the homogeneous and isotropic FLRW model is usually used as a background solution and the dark matter is approximated as a fluid with density ρ but without pressure. This approach was first applied by Jeans (1902) to study the instabilities in evolving clouds of gas in the context of a static background fluid. Such a fluid evolves according to the following coupled differential equations

$$\begin{aligned} \frac{\partial \rho}{\partial t} + \nabla \cdot (\rho \mathbf{v}) = 0 \qquad & \text{Continuity} \\ \frac{\partial \mathbf{v}}{\partial t} + (\mathbf{v} \cdot \nabla)\,\mathbf{v} = -\nabla\phi \qquad & \text{Euler} \\ \nabla^2\phi = 4\pi G\rho \qquad & \text{Poisson} \end{aligned} \tag{2.7}$$

Working in the **comoving coordinates** $\mathbf{r} = a(t)\mathbf{x}$ and perturbing the density and potential as

$$\begin{aligned} \rho &= \langle\rho\rangle\,(1+\delta) \\ \nabla^2\hat{\phi} &= \nabla^2\phi - 4\pi G\langle\rho\rangle a^2 \end{aligned} \tag{2.8}$$

and only keeping the small quantities $\dot{x}$ and δ up to first order, the fluid equations become

$$\begin{aligned} \frac{\partial \delta}{\partial t} + \nabla\dot{\mathbf{x}} = 0 \qquad & \text{Continuity} \\ \ddot{\mathbf{x}} + 2H\dot{\mathbf{x}} = \frac{\nabla\hat{\phi}}{a^2} \qquad & \text{Euler} \\ \frac{\nabla^2\hat{\phi}}{a^2} = 4\pi G\langle\rho\rangle\delta \qquad & \text{Poisson} \end{aligned} \tag{2.9}$$

By taking the divergence of the Euler Equation and substituting $\nabla\dot{\mathbf{x}}$ and $\nabla\ddot{\mathbf{x}}$ using the Continuity and Euler equations we obtain the first order perturbation growth equation for a pressureless fluid

$$\ddot{\delta} + 2H\dot{\delta} = 4\pi G\langle\rho\rangle\delta \tag{2.10}$$

or written in terms of the density parameter $\Omega = \frac{8\pi G}{3H}\rho$,

$$\ddot{\delta} + 2H\dot{\delta} = \frac{3}{2}H^2\Omega\delta \quad . \tag{2.11}$$

Here, the Hubble expansion H gives rise to a drag term preventing exponential growth of the perturbations. This second order differential equation has two solutions corresponding to a growing mode and a decaying mode. We are only interested in the growing mode solution, since if the decaying mode exists it would decay with time. We can write this growing mode as

$$\delta(t) = \delta_0 D(t) \tag{2.12}$$

where $D(t)$ is the growth factor of the perturbations. For example, for a flat $\Omega_m = 1$ Universe together with the Friedmann equations,

$$D(a) \propto t^{2/3} \propto a \quad . \tag{2.13}$$

This equation is approximately valid at early times where $\Omega_m \to 1$. In a low density Universe the growth of the perturbations slows as Ω_m decreases.

Taking the Fourier Transformation of each overdensity term

$$\delta = \sum_{\mathbf{k}} \delta_{\mathbf{k}} e^{-i\mathbf{kx}} \tag{2.14}$$

one can show that each $\mathbf{x}$-mode evolves independently and follows the differential equation

$$\ddot{\delta_{\mathbf{k}}} + 2H\dot{\delta_{\mathbf{k}}} = 4\pi G\langle\rho\rangle\delta \tag{2.15}$$

2.1.2. Gravitational Clustering of Dark Matter

Above we have discussed the origin of small fluctuations and their expansion in time. The above derivations have all been made with the linearised perturbation equations. At some point, however, gravity eventually will cause the collapse of overdensities to form non-linear gravitationally bound objects. For the equations where $\delta \gg 1$, the non-linearity of Einstein's equations becomes evident, making a fully analytical explanation much more difficult. However in limiting cases, notably the large scale limit, it is possible to extend some of the simple results of linear theory to higher order.

A useful special case is the Zel'dovich approximation which can also be used to set up initial conditions for a cosmological N-body simulation. Another simple but different approach is the spherical collapse model which also provides a useful insight in understanding the general case of structure formation. In the cold dark matter scenario, large scale structures, as well as galaxies, are though to be built by a process of hierarchical clustering: Initial overdensities are amplified by gravitational growth and eventually become bound objects. An important factor for theories of structure formation is the abundance of such bound dark matter clumps. To first order the

abundance of a halo of mass M will be a function of mass only. The Press-Schechter theory (Press & Schechter, 1974), which uses the spherical top collapse model and linear growth theory, gives an intuitive and useful analytic description of this mass function.

Zel'dovich approximation

The Zel'dovich approximation (Zel'dovich, 1970) provides a simple analytical model of the gravitational evolution of density inhomogeneities. It also provides a convenient way of setting up the initial conditions of a cosmological N-body simulation. The ZA arises from Newtonian theory but it has been shown that the approximation, as well as its second order improvements, can be derived in a general relativistic framework for cosmology (Rampf & Buchert, 2012; Rigopoulos & Valkenburg, 2012). Rather than observing a continuum quantity such as pressure or density, the ZA looks at the time varying Lagrangian motion of a fluid element from the point of view of a particle. In addition, the motion of the particle is studied in a comoving coordinate system rather than working out the development of the perturbation in some external Eulerian reference frame. If the comoving coordinate of a particle at the center of the perturbation is $\mathbf{q}$, the Eulerian position $\mathbf{x}$ at time t is given by

$$\mathbf{x}(t) = \mathbf{q} + \Psi(\mathbf{q}, t) \tag{2.16}$$

where Ψ is the displacement of the particle and satisfies the Lagrangian equation of motion

$$\frac{\partial^2 \Psi}{\partial t^2} + 2H\frac{\partial \Psi}{\partial t} = -\nabla_x \phi \quad . \tag{2.17}$$

The density contrast $\delta(\mathbf{x}, t) = \det\left(\partial x_i / \partial q_j\right)^{-1} - 1$ is determined with equation 2.17 as well as the Poisson equation now written in terms of the density parameter Ω

$$\nabla_x^2 \phi = \frac{3}{2} H^2 \Omega \delta \tag{2.18}$$

The ZA approach now makes the assumption that the displacement Ψ scales with the linear growth factor (to first order)

$$\Psi \propto -D \nabla_x \phi_0 \tag{2.19}$$

where the ϕ_0 is the potential at the initial time t_0. It is important to note that with this approximation an assumption about the dynamics of the particles is made whereas the geometry is left to be chosen freely. With this assumption it can be shown that the displacement Ψ follows the equation

$$\frac{\partial^2 \Psi}{\partial t^2} + 2H\frac{\partial \Psi}{\partial t} = \frac{3}{2} H^2 \Omega \Psi \tag{2.20}$$

The two equations 2.19 and 2.20 provide an approximation for the gravitational collapse. They are only valid as long as the fluid elements from different positions never

coincide in Eulerian coordinates. This approximation therefore breaks when shell crossings occur.

The above description is often used to construct initial conditions for an N-body simulation (Doroshkevich et al., 1980; Bertschinger, 1998). The ZA is also an important tool in understanding N-body simulations. For this we slightly rewrite equation 2.16 as

$$x(t) = a(t)\mathbf{q} + b(t)\mathbf{P}(\mathbf{q}) \tag{2.21}$$

where the displacement is now parameterised by some function $\mathbf{P}(\mathbf{q})$. The Zel'dovich approximation to the displacement manifests itself now in describing the motion of each particle by a linearised **deformation tensor**

$$S = |dx_i/dq_i| = a(t)\delta_{ij} + b(t)\partial x_i/\partial q_j \quad . \tag{2.22}$$

Transforming S into the coordinate system of the principal axes S is diagonalised:

$$S = \begin{bmatrix} a(t) - \alpha b(t) & 0 & 0 \\ 0 & a(t) - \beta b(t) & 0 \\ 0 & 0 & a(t) - \gamma b(t) \end{bmatrix} \tag{2.23}$$

where here $\mathbf{P}(\mathbf{q})$ is now represented by three constants α, β, and γ related to the principal axes of the local ellipsoid. Due to mass conservation the evolution of the density is described by

$$\rho\left[a(t) - \alpha b(t)\right]\left[a(t) - \beta b(t)\right]\left[\gamma b(t)\right] = \langle\rho\rangle a^3(t) \tag{2.24}$$

where $\langle\rho\rangle$ is the mean density of the matter in the Universe. The density will approach a singularity along the largest of the principle axes. The ZA therefore shows that collapse first occurs along one direction into a planar configuration forming the so-called **pancakes**. Shell crossings occur when the value inside one of the brackets of equation 2.24 vanishes e.g. $a(t) - \alpha b(t) = 0$. At this point the density formally goes to infinity and the ZA breaks down. In reality, the density does not go to infinity since conservation of angular momentum in the dark matter particles prevents singular collapse. Angular momentum is conserved because of the nondissipative nature of dark matter. Results of numerical N-body simulations have shown that the ZA is remarkably accurate until shell crossing happens (Coles et al., 1993).

Spherical Top-Hat Collapse Model

The spherical top-hat collapse model is an alternative way to develop a better understanding of the formation of structures from the evolution of perturbations in the nonlinear regime. As shown above, the ZA model makes an assumption and approximation to the dynamics but makes no restriction on the particular geometry of the system. The spherical collapse model takes a completely different approach by assuming a spherical symmetric region with an uniform overdensity δ_0 at initial time t_0 in an otherwise critical density matter dominated Universe. It makes no assumptions on the dynamics of the system. With the help of Birkhoff's theorem the spherical

overdense region can be treated as a separate Universe where its radius is a function of time evolving with Friedmann's equations. For the evolution of the perturbations we therefore can look at the Friedmann equation for the overdensity

$$\dot{a}^2 = \frac{\Omega_i}{a} + \Omega_i - 1. \tag{2.25}$$

where the index i denotes different density components. This differential equation has a parametric solution as a function of $\theta \in [0, 2\pi)$

$$a = \frac{a_{\max}}{2}(1 - \cos\theta) \tag{2.26}$$

$$t = \frac{t_{\max}}{\pi}(\theta - \sin\theta) \tag{2.27}$$

where $a_m ax = a_0\Omega_i(1-\Omega_i)^{-1}$. For early times, when θ is small, we can expand the function to first order and obtain a linear theory for the development of the overdense region

$$a_{\rm lin}(t) = \frac{1}{4}\left(\frac{6\pi t}{t_{\max}}\right)\left[1 - \frac{1}{20}\left(\frac{6\pi t}{t_{\max}}\right)^{2/3}\right] \tag{2.28}$$

The first term on the right hand side corresponds to the background expansion of the critical density of the Universe. It scales for early times as $\delta \propto t^{2/3}$. If we now assume that the initial mass of the system is $M = \frac{4\pi}{3}\langle\rho\rangle r^3$ and enhance the density by an overdensity δ then we can argue that the radius must shrink by δr in order to conserve the enclosed mass:

$$M = \frac{4\pi}{3}\langle\rho\rangle r^3 (1+\delta)(1+\delta r)^3 \tag{2.29}$$

For the equation to balance, we must have that $(1+\delta)(1+\delta r)^3 = 1$. Expanding to first order we derive a prediction for the density contrast

$$\delta \approx -3\delta r = \frac{3}{20}\left(\frac{6\pi t}{t_{\max}}\right) \tag{2.30}$$

Using the equations above, a few key events in the history of the density perturbations can be quantified. At the beginning, overdense regions grow with the Hubble expansion. At a specific time this expansion stops under its own self gravity, reaching a maximum expansion at $\theta = \pi$. This turnaround occurs when the linear density contrast is $\delta_{\rm turnaround} \approx 1.06$. Hence, shortly after a perturbation's overdensity exceeds unity, it turns around and begins to contract. The final collapse occurs when $\theta = 2\pi$. The overdensity at this point is $\delta_{\rm collapse} \approx 1.69$. It is at this turnover where the spherical collapse model starts to become invalid and it can be shown that the actual overdensity will become infinite at $t_{\rm end}$. Clearly, the assumption of a perfectly spherically symmetric, pressureless overdensity is ideal and we do not really expect the collapse to continue to a singularity. In fact, the overdense regions virialise rather than collapsing to a point because dark matter accumulates a net angular momentum from torques in the last scattering surface. Because of the collisionless nature of dark

matter it cannot dissipate this angular momentum which halts the collapse. The dark matter particles eventually obtain virial equilibrium through dynamical friction which results in a pressure-supported virialised collapsed structure commonly known as a **halo**. The average density within the virialised object is usually estimated by assuming a virialized radius of half of the turnaround radius. The density of the spherical region will therefore increase by a factor of eight until virilisation whereas the density of the non-virialised region increases only by a factor of four. This occurs when the density reaches

$$\delta_{\rm vir} = 18\pi^2 \approx 178 \tag{2.31}$$

This number is important for defining a bound object in N-body simulations. Typically an overdensity of $\delta_{\rm vir} = 200$ is assumed.

The Halo Mass Function

The two models above suggest that initial overdensities will be amplified by gravitational growth and later build virialised objects called halos. The so-called Press-Schechter theory provides an analytic formalism for the process of structure formation once the overdensities have collapsed into a halo. It provides insight into the evolution of the halo mass function, discussed below, and succeeds in describing the hierarchical clustering seen in N-body simulations.

The idea of the Press-Schechter theory is that the halos form at peaks of matter density fluctuations in the early Universe. Those fluctuations are described by spheres of mass M and the density distribution is assumed to be Gaussian. We therefore make the assumption that the probability distribution and overdensity of M can be described by a Gaussian function with zero mean

$$p(\delta) = \frac{1}{\sqrt{2}\sigma(M)} \exp\left(-\frac{\delta^2}{2\sigma^2\,(M)}\right) \tag{2.32}$$

where $\delta = \delta\rho/\rho$ is the overdensity associated with M, and $\sigma(M)$ is the standard deviation. The root mean square overdensity within sphere of radius R is monotonically decreasing as a function of mass. Large scales therefore correspond to a smaller standard deviation and hence are smaller in amplitude than those on small scales. This results in a **bottom up** picture of structure formation as small structures are believed to form before large structures. In the Press-Schechter theory we assume the linear theory of the spherical collapse model is valid until the density reaches the threshold of $\delta_c = 1.69$ and then collapses immediately afterwards. This seemingly unphysical approximation can somehow be justified by the fact that gravitational instability operates very quickly.

At any given time, all regions that have a density over δ_c are believed to collapse and form halos. The fraction of a sphere of radius R that exceeds a threshold at a given time t is given by

$$f(\delta > \delta_c) = \frac{1}{2}\mathrm{erfc}\left(\frac{\delta_c}{\sqrt{2}\sigma(R)}\right) \tag{2.33}$$

with

$$\mathrm{erfc}(x) = \frac{2}{\sqrt{\pi}} \int_x^\infty \exp\left(-x^2\right) dx \quad . \tag{2.34}$$

[1] If we mistakenly assume that this fraction can be identified with the fraction of particles which are part of collapsed lumps with masses greater than M then we run into a problem. For small masses M the mean square function goes to infinity and therefore the fraction of points f converges to 1/2. Hence the formula above predicts that only half of the particles are part of lumps of any mass. In other words, the negative part of the Gaussian distribution has been left out as it corresponds to underdense regions. The so-called "swindle" in the Press-Schechter approach is to multiply the mass fraction by an arbitrary factor of 2.

The fraction of mass that is in halos between mass M and $M + dM$ is given by df/dM. The number density of collapsed lumps is the number density of all halos ρ_0/M times the fraction of mass in halos in the range $M \to M + dM$

$$\begin{aligned} \frac{dn(M,t)}{dM} &= -2 * \frac{\rho_0}{M} \frac{\partial f}{\partial R} \frac{dR}{dM} \\ &= -2\sqrt{\frac{2}{\pi}} \frac{\rho_0}{M} \frac{\delta_c(t)}{\sigma^2} \exp\left(-\frac{\delta_c^2(t)}{2\sigma^2}\right) \end{aligned} \tag{2.35}$$

where $\delta_c(t) = \delta_c/D(t)$ is the critical overdensity linearly extrapolated to the present time. The normal procedure to find the number density is to calculate σ and its derivative from the linear theory matter power spectrum.

The Press-Schechter formula for dn/dM agrees remarkably well with N-body simulations, despite some of the unphysical assumptions made above. The formula is known to deviate in detail at both high and low mass ends as it tends to systematically under predict large-mass halos and over predict small-mass halos. Refinements to this theory have since been made. In particular, a better fit to the mass function in N-body simulations has been proposed by Sheth & Tormen (1999) by assuming that the halos are elliptical instead of spherical. This approach seems to provide a more accurate fit to some N-body simulations (Reed et al., 2003; Jenkins et al., 2001).

Bond et al. (1991) proposed an alternative approach bases on excursion sets to statistically estimate how many small halos would be subsumed into larger ones. This approach reduces the number of small-mass halos compared to Press-Schechter and increases the number of large-mass halos and is therefore in better agreement with simulations. Another advantage of this excursion set approach is that it also allows a characterisation of the merger rate of dark matter halos.

To derive the number density of the halos we consider a spherical region of mass M_2 with a linear overdensity $\delta_c/D(t_2)$ which forms a collapsed object at time t_2. The fraction of halos in collapsed objects of a certain mass at an earlier time $t_1 < t_2$ is

[1] The complimentary error function $\mathrm{erfc}(a/\sigma\sqrt{2})$ is the probability that the error of a measurement drawn from a standard Gaussian distribution lies outside the region $-a$ to a.

given by

$$f\left(S_1, D_1|S_2, D_2\right) dS_1 = \frac{1}{\sqrt{2\pi}} \frac{\delta_1 - \delta_2}{\left(S_1 - S_2\right)^{3/2}} \exp\left[-\frac{\left(\delta_1 - \delta_2\right)^2}{2\left(S_1 - S_2\right)}\right] dS_1 \quad , \tag{2.36}$$

where $S_1 = \sigma^2\left(M_1\right)$, $S_2 = \sigma^2\left(M_2\right)$, $\delta_1 = \delta_c/D(t_1)$, and $\delta_2 = \delta_c/D(t_2)$.

Halo Structure

Within the framework of the cold dark matter cosmology, dark matter halos are predicted to have triaxial shapes (Barnes & Efstathiou, 1987; Frenk et al., 1988; Dubinski & Carlberg, 1991; Warren et al., 1992; Cole & Lacey, 1996; Thomas et al., 1998; Jing & Suto, 2002). Simulations have revealed that prolate haloes form via mergers with low angular momentum where oblate halos form via mergers with high angular momentum. N-body simulations have shown that the final haloes formed via mergers with varying amounts of angular momentum leading to haloes with arbitrary triaxiality where the triaxiality also varies with radius (Moore et al., 2001; Vitvitska et al., 2002). Numerical experiments of isolated equilibrium models are thought to be very useful for studying the evolution of self-gravitating systems in a controlled way.

Many techniques exist to construct N-body realisations of spherical haloes and multicomponent galaxies (Hernquist, 1993; Kazantzidis et al., 2004b), but it is more complicated to build triaxial equilibria models. Triaxiality can generally arise from a number of ways. A popular way to construct a numerical model of triaxial galaxies is by the study of merger simulations. There are a number of examples throughout the literature which include binary mergers of spherical halos (e.g., White, 1978; Fulton & Barnes, 2001) as well as disk galaxies (e.g., Gerhard, 1981; Barnes, 1992; Barnes & Hernquist, 1996; Naab & Burkert, 2003; Kazantzidis et al., 2004a). Multiple mergers of systems have also been studied (e.g., Weil & Hernquist, 1996; Dubinski, 1998). A major result of their studies is that the structure of the merger remnant of two component models sensitively depend on the orbital geometry (Naab & Burkert, 2003) as well as the inclination and internal properties of the disks (Kazantzidis et al., 2004a). Merritt & Fridman (1996) constructed a fully self-consistent model of triaxial galaxies with central density cusps. They used a triaxial generalisation of Dehnen's spherical mass models which had densities that vary as $r^{-\gamma}$ near the center and r^{-4} at large radii. Their attempts to construct self-consistent solutions using the regular orbits failed for both mass models with $\gamma = 1$ ("weak cusp") and $\gamma = 2$ ("strong cusp"). Instead they constructed quasi-equilibrium solutions that include stochastic orbits. A general technique for constructing such cuspy axisymmetric and triaxial N-body halos would however be preferable. Based on the way in which structures form in hierarchical cosmological simulations Moore et al. (2004) explored the generation of triaxial structures. They demonstrated that major mergers between two isolated equilibrium spherical cuspy haloes form similarly cuspy triaxial merger remnants where higher angular-momentum mergers produce systems with lower concentrations. They found that radial mergers produce prolate systems, while mergers on circular orbits produce oblate systems. This method presents a way to construct cuspy axisymmetric and

triaxial N-body haloes. It specially has the benefit that it is based on the observations of how haloes are formed in cosmological N-body simulations.

Cosmological N-body studies (Navarro et al., 2004; Merritt et al., 2005; Prada et al., 2006) showed that density profiles of dark matter halos have an approximately universal form which is better described by the Einasto profile (Einasto, 1965) than the Navarro-Frenk-White (NFW) profile (Navarro et al., 1996, 1997). The Einasto density profile is given by

$$\rho(r) = \rho_{-2} \exp\left(-\frac{2}{\alpha}\left[\left(\frac{r}{r_{-2}}\right)^{\alpha} - 1\right]\right) \tag{2.37}$$

where r_{-2} is a characteristic radius at which the logarithmic slope of the density profile equals -2 and α is a parameter which controls how rapidly the logarithmic slope varies with the radius. The NFW density profile is given by

$$\rho(r) = \frac{\rho_s}{(r/r_s)\,(1 + r/r_s)^2} \tag{2.38}$$

where ρ_s is the characteristic inner density and r_s is the scale radius. They are tightly correlated with the halo virial parameters, via the concentration, $c = r_{\rm vir}/r_s$, and the virial overdensity $\delta_{\rm vir}$. The NFW corresponds to a cummulative mass distribution that diverges when $r \to \infty$. The profile has a simpler form and is still good to within 10-20% when defining an exponential cut-off for $r > r_{\rm vir}$ which sets in at the virial radius and turns off the profile on a scale $r_{\rm decay}$ which is a free parameter and controls the sharpness of the transition

$$\rho(r) = \frac{\rho_s}{c(1+c)^2}\left(\frac{r}{r_{\rm vir}}\right)^{\epsilon} \exp\left[-\frac{r - r_{\rm vir}}{r_{\rm decay}}\right] \tag{2.39}$$

The concentration c was found to depend weakly on halo mass and on redshift and can be predicted from the formation history of a halo (Wechsler et al., 2002). Simple algorithms to approximately determine concentrations have been proposed by various authors (Navarro et al., 1997; Eke et al., 2001; Bullock et al., 2001) More accurate power-law fits have also been proposed by several authors (Prugniel & Simien, 1997; Gao et al., 2008; Zhao et al., 2009; Stadel et al., 2009).

2.2. Taking Baryons into the Picture

The night sky we see generally consists of electromagnetic radiation emitted by matter like stars and galaxies. In the previous sections we have only discussed the evolution and formation of dark matter structures. Gravity alone does not provide a complete description of the observations made, especially since dark matter does only interact gravitationally with luminous matter. For the understanding of the processes that shape galaxies and their evolution it is crucial to introduce baryons into the picture. In the standard picture of cosmology it is predicted that small halos form before larger halos evolving hierarchically to form a cosmic web. Intuitively it is assumed that baryons concentrate towards the potential wells of the dark matter halos and

that these halos would be the sites of galaxy formation. This standard picture of hierarchical galaxy formation was introduced by White & Rees (1978) and has since then been extended. In this picture the baryons fall into the potential wells of the haloes forming a hot gaseous halo for which the self-gravity of the fluid is balanced by pressure gradients. The hot gas in this halo is able to cool through cooling mechanisms involving the physics of the plasma and the atomic structure of its components. The cooling however reduces the pressure support and causes the accretion of cold gas from the halo onto a central disc. Stars form as a function of the gas density on a characteristic time-scale, which results in a rotating stellar disc and stars start to form. The star formation time-scale is proportional to the local free-fall time. A fraction of the newly formed stars is short-lived and these stars explode in supernovae which again feedback heat into the surrounding gas. This can in turn again result in reducing the efficiency of star formation and in some cases blow gas out of the galaxy in a so-called galactic wind. These supernovae-driven winds are thought to suppress the formation of low-gas galaxies. Another potential source of feedback is provided by the accretion of gas onto a supermassive black hole in the center of the galaxy, called active galactic nuclei (AGN). All these processes explained above are however not fully understood. There are still many open questions left to be answered. The baryonic structure of the galaxies, the processes such as star formation, momentum feedback from supernovae, and AGNs, just to name a few still, have to be better understood.

Due to the hierarchical nature of the formation of the cosmic web, dark matter halos constantly accretes new material and merge with other galactic systems. Such a merger can trigger new star formation and at the same time angular momentum is transferred to the stars in the disc. In this way galaxy mergers are extremely important in affecting the morphology of galaxies and shape their properties. An important goal of galaxy formation is to understand the correlation of the internal properties of a galaxy with their formation history and environment.

2.2.1. Galaxy Morphology

Nature has provided an immensely varied array of galaxies, ranging from faint, diffuse dwarf objects to brilliant spiral-shaped giants. These variations result from the way in which the systems were formed and subsequently evolved. In order to classify these variations, Edwin Hubble (Hubble, 1926) invented a morphological scheme still often used today. The **Hubble sequence** was later expanded by Gerard de Vaucoulerus and Alland Sandage.

Hubble's scheme divides the regular galaxies into three main forms:

- **Elliptical galaxies**: These galaxies have a smooth, featureless light distribution and appear as ellipses in photographic images. They are classified by the letter E, followed by an integer n which represents their degree of ellipticity on the sky. By definition n is ten times the ellipticity of the galaxy, rounded to the nearest integer. The ellipticity is usually defined as:

$$e = 1 - \frac{b}{a} \tag{2.40}$$

where a, and b represent the major axis, and minor-axis of the ellipsoid, respectively.

- **Spiral galaxies**: These consist of a disk, hosting a spiral pattern of stars. They are represented by the symbol S. Roughly half of all spirals are observed to have a bar-like structure which extends from the central bulge. Such barred spirals are given the symbol SB. Both types of spiral galaxies can also be further subdivided according to the detailed appearance of their spiral structures.

- **Lenticular galaxies**: These consist of a bright central bulge and are similar in appearance to an elliptical galaxy. In addition they are also surrounded by an extended, disk-like structure similar to the spiral galaxies. They are given the symbol S0. In contrast to the spiral galaxies the lenticular galaxies do not show any spiral structure in their disc.

These three classes can be further extended into finer distinctions, in particular, by defining a fourth class which contains all of the galaxies that do not show any obvious regular structure, called **irregular galaxies**.

The de Vaucouleurs system for classifying galaxies is often used as an extension to the Hubble sequence and was first described by its name sake Gerard de Vaucouleurs in 1959. To complement Hubble's scheme, de Vaucouleurs introduced a more elaborate classification for spiral galaxies based on three main characteristics: **Bars**, **Rings**, and **Spiral arms**. To fully describe the galaxy, the three elements of the classification scheme are combined. To assign each galaxy class to the formation time in the history of the Universe, de Vaucouleurs also introduced numerical values to each class of galaxy. Early-type galaxies, such as ellipticals and lenticulars, received a negative number where late types such as spirals and irregulars received a positive number.

2.2.2. Galaxy Interactions

While many galaxies seem to be evolving in isolation there are many indications that some galaxies are interacting with other galaxies or their environment. Galaxy interactions are also thought to affect the morphology of galaxies and are play an important role in their evolution.

Galaxy Orbits

As discussed above, the dark matter halos are built hierarchically where the halos merge with each other to build even larger ones. It is generally found that during the coarse of various mergers with varying amounts of angular momentum, haloes with arbitrary triaxiality can be formed where the triaxiality varies with radius (Moore et al., 2001; Vitvitska et al., 2002). N-body simulations such as (Tormen et al., 1998; Moore et al., 1999; Klypin et al., 2008) found that halos can persist as subhalos within larger halos into which they merge. Each subhalo is thought to be the formation site of a galaxy. Many of the subhalos therefore contain a galaxy which became a satellite

in the host potential. These subhalos are usually gravitationally bound to their bigger host halo and as such orbit within it.

Despite the fact that simulations predict triaxial dark matter halos, observations have found quite round halos. This change can most likely be explained by taking into account the baryons, where it is thought that the condensation of baryons leads to rounder halos. Triaxial halos are generally supported by box orbits, which pass arbitrarily close to the density center. It is assumed that the decrease in triaxiality caused by the baryons is due to the scattering of these orbits. Debattista et al. (2008) tested this hypothesis and found that the central condensation of baryons does not destroy enough box orbits to cause the shape to change. Rather, the box orbits become rounder along with the global potential. If however angular momentum is transferred to the halo, either via satellites or via bars, then the irreversible changes in the halo distribution are substantially larger. This ability of satellites to alter the phase space distribution of the halo is also of special interest to galaxy formation simulations since they obviously can affect the properties of any galaxy that it may contain. It is especially thought to influence the evolution of disks.

Gravitational Interactions

Mergers

Mergers are thought to play an important role in the formation and evolution of a galaxy. Since orbiting subhalos are gravitationally bound to their host and therefore rarely encounter other subhalos at velocities that result in a bound interaction (Somerville et al., 2008, and reference therein), such interactions require a dissipative process to reduce the orbital energy of the galaxies. Dynamical friction is, for example, such a process. It causes the galaxy to loose energy and drags the subhalos down towards the center of the host halo where they in turn might merge with other subhalos.

Over the last few years the effect of mergers on galaxies has been intensely studied. In particular, the question whether elliptical galaxies have formed from mergers, first proposed by Toomre & Toomre (1972), has been widely tested with simulations. Elliptical galaxies can be divided into objects with boxy and disky isophotal shapes. A wide variety of N-body simulations have shown that merger remnants mimic important features of elliptical galaxies such as photometric and global kinematic properties, kinematic misalignments, or kinematically decoupled cores (Barnes, 1992; Hernquist, 1992, 1993; Naab et al., 2006b; Burkert & Naab, 2004). Several authors studied the orbital content of simulated merger¡ remnants. One of the main results was that the centre of the remnants is dominated by box orbits whereas minor-axis tubes dominate at larger radii. Jesseit et al. (2005) performed a large number of collisionless simulations and analysed the orbital content of the merger remnants. In their work they found that the number of minor axis tubes increases with increasing mass ratio. This indicates that in unequal mass mergers it is more difficult to destroy the orbit population of progenitor discs. At the same time they found that the boxlet and box orbit fractions decrease with increasing mass ratio. They also show that for identical merger symmetries but with larger pericentral distance, the minor axis tubes are pop-

ulated more strongly than for the close encounter sample. This confirms the studies of Barnes & Hernquist (1996) where they claimed that a central mass concentration destroys the box orbits. Additionally they confirm the work of Barnes & Hernquist (1992) claiming that different orbit classes dominate at different radii inside the merger remnants. They also demonstrate that different disc inclinations generally lead to different orbital structures while pericentre distance and mass ratio are identical. They, however, do not make a quantitative assumption of which disc inclination causes more boxy galaxies.

It is of no surprise that the presence of gas in mergers has a significant impact on the orbital structure. Gas generally is assumed to destroy the box orbits at the centre of the galaxies and minor axis tubes become more populated. Naab et al. (2006b) presented simulations of a large set of mergers of early type disc galaxies inclined by 30 degrees with different mass ratios. They found out that in contrast to the collisionless case, equal mass mergers with gas do not result in very boxy remnants. This is caused by the suppression of box orbits and the change of the projected shape of minor-axis tube orbits in the more axisymmetric remnants. This stands in agreement with the results of Moore et al. (2004) where they studied the change of the halo structure in presence of baryons. Naab et al. (2006b) found that generally major mergers are slowly rotating, whereas minor mergers with a mass ratio of 3:1 are fast rotating and discy. They have also shown that after the galaxies have merged between 40% and 85% of 1:1 merger of the gas has accumulated at the centre.

The intrinsic shape of a triaxial mass distribution is defined by the ratio of its three principal axes. The principal axes are determined by diagonalising the moment of inertia tensor of the galaxy. The triaxiality parameter is defined as

$$T = \frac{a^2 - b^2}{a^2 - c^2} \tag{2.41}$$

where a,b, and c are the long-, intermediate- and minor axis, respectively. Jesseit et al. (2005) found out that the shape of merger remnants is closely related to their intrinsic orbital structure. Looking at pure collisionless mergers they found that the peak of the box orbit abundance is located at $T = 0.5$. They also found that the minor axis tube fraction rises strongly with decreasing T to 60% for oblate shapes ($T = 0$) and drops to values as low as 20% for very prolate shapes ($T = 1$). When taking the gas into account Naab et al. (2006b) found that the presence of gas influences the intrinsic shape of the stellar components of the merger remnants. They found that the triaxiality is lowered for almost every remnant due to the influence of gas. Although the triaxiality of their major merger remnants is also lowered substantially the effect is smaller than that for 3:1 remnants. Comparisons of the population of each orbit class averaged over all 1:1 and 3:1 mergers respectively for all merger remnants with and without gas they showed that gas drastically reduces the fraction of box orbits while the fraction of minor axis tubes increases by a factor of two to three. When comparing the orbits with the intrinsic shape of the remnants they found that, generally, box orbits appear to be box shaped with the exception of the projection along the major axis where we look edge on and the box orbits do not extend much. This suggests one should study of the viewing angle and the intrinsic shape of the galaxy. Franx (1988)

suggested that whether or not the isophotal shape appears discy or boxy depends not only on the intrinsic structure of the galaxy but also on the viewing angle. This was confirmed in simulations of collisionless disc-disc mergers by Heyl et al. (1994). Naab et al. (2006b) also studied the influence of the viewing angle and examined only the projections along the principal axes of the merger remnants. They claimed that this would result in the most extreme values of the boxiness of all possible projections. The boxiness is usually measured by approximating the isophotes of the galaxy with a Fourier series

$$I(\theta) = I_0 + \sum_{n=1}^{\infty}(A_n \cos(n\theta) + B_n \sin(n\theta) \quad . \tag{2.42}$$

where θ is the azimuthal angle and I_0 is the average intenisty over the ellipse. The A_4 coefficient to the $\cos 4\theta$ component is used to quantify the isophotal deviation from an ellipse. It is positive (negative) when the isophotes are discy (boxy). Naab et al. (2006b) found that the projection along the major axis is the most sensitive to the orbital content of the merger remnants. Remnants with negative a_4 were found to have indeed a dominant box orbit population while the most discy remnants were dominated by minor axis tubes. In their study they found that the projection along the intermediate axis is the most complicated one. Where almost none of the remnants could be identified as boxy. Finally the projection along the short axis is found to be more sensitive to the orbital content. Building on the work of Jesseit et al. (2005) and Naab et al. (2006b), Hoffman et al. (2010) simulated seven different major disk mergers at seven different initial gas fractions ranging from 0% to 40% including radiative heating and cooling, star formation, and feedback from supernovae and active galactic nuclei. They show that equal mass mergers of such disk galaxies can in the presence of 15%-20% gas, generate early-type slowly rotating galaxies with kinematically distinct cores. They also noted that as the gas fraction increases, the box orbits within 1.5 R_e, where R_e is the half light radius, get increasingly replaced by sharp embedded disks. They however have also shown that the outer parts of the remnants (outside $\sim 1.5R_e$) are less relaxed than the inner parts, and are therefore largely unaffected by the gas content of the disks. This suggests that if boxy orbits exist at large radii they are not affected.

Tidal Destruction

When a subhalo is orbiting in a bigger host halo its galaxy will experience tidal forces. This strips away the outer regions or, in extreme cases, results in the entire disruption of the subhalo, creating a stellar stream. The removing of the galaxy's gas prevents any new star formation. The external tidal perturbations are strongest during the subhalo's pericenter passages. It is found that particles in an orbiting satellite that are on prograde orbits are more easily stripped than those on radial orbits which are in turn more easily stripped than those on retrograde orbits (Read et al., 2006). The tidal perturbations can also trigger a disk instability which generates a bar-like component while kinematically heating many stars out of the disk plane. The disk therefore undergoes different morphological stages. The disk, and then the bar, puff out and partially evaporate which in turn lowers the average stellar density and can

result in the galaxy looking somewhat rectangular (Mayer et al., 2007; Łokas et al., 2010).

Harassement

When tidal forces are not strong enough to eventually strip material from the galaxy one generally talks about harassment. The harassment process works via so called **tidal shocking** where the stars in a galaxy experience a rapidly changing tidal field along its orbit. Harassment has been used to explain the presence of some dwarf spheroidal galaxies within galaxy clusters Moore et al. (1996b, 1998, 1999). Through this process, close encounters can result in pure disk galaxies which causes the galaxy to develop a strong stellar bar (e.g., Noguchi, 1988; Gerin et al., 1990). This stellar bar remains intact while the remaining outer disk can get stripped away by various high-speed encounters with other galaxies. Even though less strong, the rapidly changing tidal forces can transfer energy from the orbit to internal motions of stars in the galaxy which can eventually heat the galaxy. As a result of such a heating, the galaxy expands and starts to destroy cold, ordered structures (Moore et al., 1996a, 1998; Mayer et al., 2001a,b; Gnedin, 2003). Such a destroying of the ordered structures can, in the presence of a triaxial potential, lead to boxy galaxies (Naab et al., 2006a).

Hydrodynamical Interactions

Dark matter is only affected by gravity because of its small interaction cross section. The baryonic content however can be strongly affected by hydrodynamical forces such as pressure, and temperature. The orbital motion of a subhalo through the hot atmosphere of a host halo leads to a large ram pressure. The characteristic magnitude of this pressure is defined as

$$p_{\rm ram} = \rho_{\rm host} V_{\rm orbit}^2 \quad . \tag{2.43}$$

This pressure can exceed the binding energy of the hot gas in the subhalos as well as the interstellar medium (ISM) gas in the galaxies. The ram pressure can therefore remove the hot atmospheres of satellite galaxies. The first quantification of this process was made by Gunn & Gott (1972). In their work they showed that the ram pressure force indeed can remove material from a galactic disk if it exceeded the gravitational restoring force.

In many cases this mass loss caused by the ram pressure can be further enhanced by similar effects such as turbulent viscous stripping (Nulsen, 1982).

3. Computational Techniques

Historically, the study of galaxy formation was based on nothing more than direct observation. Unlike other fields of physics it is difficult to perform experiments that test astrophysical theories.

While observations are still necessary to compare with predictions and provide scientists with new experimental discoveries, computers have allowed theorists to perform numerical experiments in order to better understand the processes which govern galaxy formation. The timescale of structure formation in general and galaxy formation in particular is so high that any theories and predictions have to be tested with simulations. Not only this, but the complexity of the different processes and phenomenas also motivates the need for simulations.

Gravity is the dominant force that drives structure formation at all scales, ranging from galaxy clusters to stars and planets. Unless an accurate description of the very early Universe, or near massive black holes is needed, gravity can be well described by Newtonian theory. Calculating the gravitational forces of systems with many bodies and evolving the motion of the bodies involved in the interaction is computational challenging. Specially, large scale structures and the study of halo formation are largely determined by the dynamics of cold dark matter which is, to first order, described by so-called pure N-body simulations. The process of galaxy formation, however, as well as many other processes, such as star and planet formation, involves a wide range of baryonic processes where pure N-body simulations would not be sufficient to describe observation. Numerical methods have to be developed that solve the wide range of physical processes such as hydrodynamical phenomena, production of relativistic particles, magnetic fields, and stellar feedback mechanisms, to name a few. When the collisional component is included in the simulations, the complexity of the problem obviously increases as does the computational time needed. A consequence of this complexity is that cosmological hydrodynamical simulations usually do not reach the same spatial resolution as pure N-body runs.

There are two major approaches that have been developed: 1) N-body simulations that attempt to directly and numerically solve the full non-linear equations involved in galaxy formation and 2) semi-analytic models that attempt to construct a full set of analytic approximations which describe the same physics. So far, such a full set of equations has not (yet) been developed and proves to be challenging given the huge range of physics involved in the galaxy formation process. It is important for the two approaches to work together as they both provide a test case for each other. Approaches to combine the advantages of N-body simulations such as high resolution and numerical treatment of gas physics with semi-analytic models have also been shown (Moster et al., 2011).

3.1. Collisionless N-body systems

As explained above, simulating cold dark matter (CDM) is important for the understanding of the formation of structures in our Universe. The CDM is thought to be a collisionless particle that interacts only through gravity. It can be described as a smooth fluid by the smooth differentiable distribution function $f(\mathbf{x}, \dot{\mathbf{x}}, t)$ which obeys the collisionless Boltzmann equation:

$$\frac{df}{dt} = \frac{\partial f}{\partial t} + \dot{\mathbf{x}}\frac{\partial f}{\partial \mathbf{x}} - \nabla\phi\frac{\partial f}{\partial \mathbf{v}} = 0 \tag{3.1}$$

Observables are extracted from f by taking moments of the Boltzmann equation. We therefore get for the density and the gravitational potential:

$$\rho = \int f d^3\mathbf{v} \tag{3.2}$$

$$\phi = -G\int d^3\mathbf{x}\frac{\rho(\mathbf{x}')}{|\mathbf{x}-\mathbf{x}'|} \tag{3.3}$$

One runs quickly into fundamental problems if equation 3.1 would be attempted to be solved directly[1] in addition to the problem being six dimensional and therefore computational hard. It nevertheless has been recently tried and some low resolution simulations have been successfully run (**?**).

If, however, the distribution function f is not completely accurately solved but rather approximated by a discrete set of N points such problems disappear. Such points are advanced by the equations of motion $\ddot{\mathbf{x}} = -\nabla\phi$, where the gravitational potential ϕ is the solution of the Poisson equation $\Delta_x\phi = 4\pi G\rho$. In this method, the particles do not represent physical self-gravitating bodies. They are a discrete sampling of the smooth distribution function f which move with the flow according to the equations of motion.

Many N-body numerical techniques have been developed to compute this evolution, some of which approximate distant forces to reduce the N^2 problem into a more manageable form. Such methods that can be used for the calculation of the force include:

- **Direct summation**: The direct summation method calculates the gravitational field **exactly**. It attempts to solve the equations 3.2 and 3.2 with a N^2 summation over all the particles. While doing so it is important to use an appropriate force softening to avoid the singularity of sample points occupying the same spatial position. The importance of a correct softening is discussed in Dehnen (2001) and references therein. In general, it is important to use a force softening which converges to the right results. This force softening is also important for the methods explained below. The direct summation method is obviously very

[1] winding problem

slow and usually not qualified for large simulations. It is therefore wise to approximate the force calculations provided the force errors are random and small enough. Since the force field is often noisy anyway, small random errors will not significantly reduce the relaxation time of the system.

- **Particle-Mesh** (PM) method: The key idea of this method is that Poisson's equation can be solved in real-space by a convolution of the density field with a Green's function:

$$\phi(\mathbf{x}) = \int g\left(\mathbf{x} - \mathbf{x}'\right) \rho\left(\mathbf{x}\right) d\mathbf{x}' \tag{3.4}$$

  In Fourier-space, the convolution becomes a simple multiplication:

$$\hat{\phi}\left(\mathbf{k}\right) = \hat{g}\left(\mathbf{k}\right) \cdot \hat{\rho}\left(\mathbf{k}\right) \tag{3.5}$$

  The only remaining unknown $\hat{\rho}\left(\mathbf{k}\right)$ can be found by using the **Fast Fourier Transforms**. The potential can be solved with the following steps:

  – Fourier transform the density field forward with FFT
  – Multiply it with the Green's function
  – FFT backwards to obtain the potential

  There are some additional complications in how the particles are initially mapped onto the grid cells and how the forces are mapped on to the particles. A more detailed description of this technique is found in Binney & Tremaine (2008). Using these mapping techniques a PM algorithm usually consists of the following four main steps:

  1. Mapping the mass density ρ on the mesh
  2. Compute the potential described above
  3. Compute the force field on the mesh
  4. Mapping the forces to the particles

  A big advantage of this method is its speed and simplicity. The most complicated step, the FFT, can be computed in $O(N \log N)$ time. There are however also some problems. If a fixed grid is used the spacial resolution is limited by the grid size. High density regions are therefore poorly resolved resulting in inaccurate force calculations. Because of this problem **adaptive meshes** are often employed rather than a fixed grid to put resolution only where it is needed (Teyssier, 2002). Another disadvantage of the fixed grid is that the force errors are unevenly distributed on the scale of the cell size. Because of this, it is, for example, difficult to perform simulations on large cosmological scales which still resolve internal structures of halos.

- **Tree method**: Another idea is to expand the potential into it's multipole moments and solve those equations. In practice this is often combined with a **tree** technique. The tree technique partitions the mass distribution into a recursive structure where at the root of the tree contains all of the particles. This is then

subdivided into cells, or branches, of the tree which are again subdivided until one arrives at one particle per cell, called leaves of the tree. In this way each node of the tree provides a full description of the matter within some spatial volume. The tree can be built by dividing the space in different ways. When computing forces, distant particles are generally mapped into a large group of cells whereas the force for close particles might be calculated with a direct summation technique depending on a particular acceptance criteria. The forces on the bodies is then computed during a single recursive scan of the entire tree. This method requires $O(N \log N)$ operations per force calculations and gives therefore a significant improvement to the direct summation method. Another advantage is that the tree algorithm has no intrinsic restriction for its dynamical range. It also gives no restriction on the geometry, which allows arbitrary configurations to be calculated. The force accuracy however largely depends on the level of the multipole expansion and therefore presents only an approximation of the true force.

- **Hybrid methods**: A modification to the PM scheme is the **Particle-Particle PM schemes** (P^3M). The idea behind this scheme is to supplement the particle-mesh scheme with a direct summation short-range force at the scale of the mesh cells. This offers a solution to the problem with the PM scheme on small scales and therefore allows higher dynamical range simulations. With those methods, problems generally appear in highly clustered regions where the simulations significantly slow down. Another modification is the **TreePM** force calculation algorithm where the potential of a single particle is split in Fourier space into a long-range and a short-range part, which are computed separately with the particle-mesh and tree algorithms, respectively. With this approach the tree is only walked locally. An important advantage of this method is the accurate and fast long-range force and that, in contrary to tree algorithms, the computational speed is insensitive to clustering as it is calculated with a different method.

3.2. Collisional systems

Although gravity is the important force in the Universe it is crucial to introduce the baryons in the simulations especially for studying galaxy formation and evolution processes. As previously discussed, the baryons introduce important properties such as feedback mechanisms, cooling, and heating, which are thought to influence the distribution of the baryons in galaxies. The baryons are usually treated as an astrophysical inviscid fluid and are therefore coupled to cold dark matter by the Poisson equation. Such a fluid is described by the Euler equations which in the absence of sinks or sources

can be written in their conservative Lagrangian form:

$$\begin{aligned} \frac{\partial \rho}{\partial t} + \nabla \cdot (\rho u) &= 0 \\ \frac{\partial}{\partial t}(\rho u) + \nabla \cdot (\rho u \times u) + \nabla p &= -\rho \nabla \phi \\ \frac{\partial}{\partial t}(\rho e) + \nabla \cdot [(\rho e + P)\, u] & \end{aligned} \tag{3.6}$$

where ρ, v, and u are the mass density, velocity and internal energy per unit mass of the flow, respectively. The equations are closed by the ideal gas equation of state:

$$p = (\gamma - 1)\, \rho \left(e - \frac{1}{2} u^2 \right) \tag{3.7}$$

where γ is the adiabatic index. The gravitational potential is added to the momentum equation 3.6 to couple the baryons with the dark matter.

In astrophysics, a huge range of fundamentally different numerical methods for hydrodynamical simulations are used but they can be mostly divided into three fundamental methods.

- **Grid-based Methods**: In the Grid-based, or Eulerian, methods the Euler equations 3.6 are numerically evolved on a discrete spacial mesh, where the differential operator is calculated using a second order finite difference approximation. The fluid quantities are advected across the grid. To capture the large density ranges often found in galaxy formation simulations or around shocks, an adaptive method is used which recursively refines high density cells (Teyssier, 2002).

- **SPH**: Smoothed Particle Hydrodynamics (SPH) was first introduced as a tool for studying stellar structure (Gingold & Monaghan, 1977; Lucy, 1977). The SPH code is a mesh-free Lagrangian particle method where the fluid elements, such as density and pressure, are traced by particles. It is a Lagrangian scheme as the geometry of the flow is closely followed by the particles. An average of a particular quantity such as mass, energy, pressure, or density is calculated by considering the local neighborhood within a smoothing length of each particle. Mathematically this is done by a **kernel** function where some fluid quantity $A(x)$ is expressed as

$$\begin{aligned} A(\mathbf{x}) &= \int d^3x' A'(\mathbf{x}') \delta \left(|\mathbf{x} - \mathbf{x}'| \right) \\ &\approx \int d^3x' A'(\mathbf{x}') W \left(|\mathbf{x} - \mathbf{x}'| \right) \end{aligned} \tag{3.8}$$

  where W is a positive definite smoothing kernel, and h is called the smoothing length. For the approximation to be valid the kernel obviously must satisfy

$$\begin{aligned} \int W d^3\mathbf{x}' &= 1 \\ \lim_{h \to 0} &\to \delta \end{aligned} \tag{3.9}$$

A good description of the kernel function and its advantage and disadvantage is given by (Dehnen, 2001). A huge advantage of SPH is that it is closely related to N-body codes since both are particles based. While both codes consider long range gravity forces, a fluid also has a pressure and viscosity which has to be considered in an SPH code. SPH codes provide accurate results for problems involving strong shocks and complex geometries. In addition the computational time is significantly reduced in low density regions which allows more computational time available for high density regions. Furthermore, SPH deals with free boundaries more easily than grid based codes.

- **Moving-Mesh Techniques**: Recently, a published, but non-public code, AREPO has been presented (Springel, 2010). This code tries to retain the accuracy of mesh-based hydrodynamical methods while at the same time using the advantages of the Galilean-invariance and geometric flexibility of the SPH codes. The principal idea for achieving such a convergence is by allowing the mesh itself to move. See Springel (2011) for further detail.

A number of comparison tests for the different codes have been performed in the last few years (Agertz et al., 2007; Khokhlov, 1998; Scannapieco, 2013). It has been shown that both SPH and AMR suffer problems that make them less accurate in certain regimes. In fact, those methods sometimes even yield conflicting results (Agertz et al., 2007). SPH codes have relatively poor shock resolution compared to AMR codes, while AMR codes suffer from problems due to their inherent non-Galilean-invariance and numerical diffusion. Comparisons between AREPO and SPH codes have also been made extensively in the last few years (Kereš et al., 2012, and references therein).

It is important to note that since the test of Agertz et al. (2007) improvements in the SPH methods have been made to stress the problems shown in the tests made in this paper (Read & Hayfield, 2012). If subgrid physics such as feedback mechanisms are involved even more discrepancy can appear (Scannapieco et al., 2012). Subgrid physics, however, is an important topic itself where a lot of discussions and improvements still have to be made. Current effort is focused on implementing more realistic subgrid models, while future computing power will also help in resolving important physics used to calibrate and test the various subgrid models.

3.2.1. RAMSES

RAMSES is a N-body and hydrodynamical code that is used for the simulations presented in this thesis. The code uses a grid with adaptive mesh refinement and the data structure is based on a tree which allows to calculate the forces and the grid refinements in one recursive scan. Up until now two time-stepping techniques have been implemented: a single time step scheme and an adaptive time step scheme. The code is able to simultaneously follow a collisionless fluid which is gravitationally coupled with an inviscid fluid. The N-body solver is mainly based on the ART code (Kravtsov et al., 1997) with some variations in the implementation. The basic computation follows the four main steps for the PM-technique described above. An adaptive mesh,

however, makes the problem more complicated to keep track of. In RAMSES, the Euler equations are solved in their conservative forms which has the advantage that energy is perfectly conserved and therefore the flow is not altered by some energy sinks. The hydrodynamical solver is a second-order Godunov scheme made for perfect gases. The collisionless and collisional fluids are coupled by considering the total density field when solving the Poisson equation to compute the gravitational potential and the force field.

The RAMSES code has been extensively tested under various conditions (e.g., Dubois & Teyssier, 2008a; Dubois et al., 2012). It has proven to be extremely suitable to study problems related to galaxy formation and their dynamics as both collisionless and collisional fluids have to be taken into account. Many additional physical processes such as heating and cooling, feedback mechanisms, magneto hydrodynamics, and AGN have been implemented in the code (Dubois & Teyssier, 2008b). The cooling function introduced by Sutherland & Dopita (1993) is implemented and also used for the simulations shown in this thesis. The functions implemented cover a wide grid of temperature and metallicities using published atomic data and processes. Various feedback mechanisms have been implemented into RAMSES over the last few years (Dubois & Teyssier, 2008c; Agertz et al., 2007; Teyssier et al., 2013). The feedback mechanism used by Dubois & Teyssier (2008c) accounts for star formation, supernova thermal feedback, and supernova kinetic feedback. The star formation feedback is calibrated to the observed star formation rate in local galaxies. The supernova thermal feedback is accounted for by using a polytropic equation of state, where it is assumed that a quasi-equilibrium thermal state is quickly reached after the interstellar medium (ISM) is disturbed by small scale effects such as turbulence, thermal instability and other effects. In this case, it can be assumed that the average temperature is a function of the mass density alone. The supernova kinetic feedback is accounted for by adding a spherical blast wave solution to each flow variable (density, momentum, and total energy). By doing so, the kinetic energy is injected into the disc which results in a turbulent gaseous disc and often in a large scale outflow.

4. Observations

Nature has provided an immensely varied array of galaxies differing from one another in shape. They range from faint diffuse dwarf objects to brilliant spiral-shaped giants. These variations result from the way in which the systems were formed and subsequently evolved. The majority of the bright galaxies can be divided into three general classes: ellipticals, spirals, and irregulars. A significant number of galaxies look ellispsoidal where most of the rest are highly irregular assemblages of luminous matter.

In March 2012, a discovery of a rare, rectangular-shaped galaxy was reported (Graham et al., 2012). LEDA 074886 was detected in a wide field-of-view image taken with the Japanese Subaru Telescope (Miyazaki et al., 2002) for a different project. This image was later provided to us for the purpose of testing the program written to analyse the simulated galaxies. While working with the image another remarkably rectangular-shaped galaxy was found. Throughout this thesis this galaxy is now named BM^2 (**B**ieri-**M**artizzi and **B**en **M**oore Galaxy). A 120×120 i-band picture of LEDA 074886 is seen in 4.2, and a 50×50 i-band picture of BM^2 is seen in 4.3.

Both galaxies lie within a group of 250 galaxies more than 70 million light years away. The positions of the two galaxies is shown in figure 4.1. It can be seen that LEDA ($\alpha = 03h40m43.3y$, $\delta = -18d38m43s$) and BM^2 ($\alpha = 03h41m18.2s$, $\delta = -18d39m39.6s$) both reside within the hot gas halo of the massive, spherical galaxy NGC 1407 (E0), with a projected separation of $\sim$ 50 kpc, and $\sim$ 100 kpc from the giant galaxies core.

4.1. LEDA 074886

As easily seen in picture 4.2, LEDA 074886 has a unusual rectangular shape. In figure 4.2 a surface brightness profile with histrogrammic light binning is shown. For the galaxy to be seen, the bright light of the NGC 1407 had to be subtracted by modelling background gradient of halo light.

The resultant light profile for LEDA 074886 is shown in figure 4.4. It can be seen that the galaxy is not a single one-component galaxy and therefore cannot be described by a single-component Sersic model. It is also shown that the inner disk component is well described with a Sersic $R^{1/n}$ model. Since, however, the disk in the center of the galaxy is slightly inclined and, given the tendency for dust to be usually concentrated in the center for at least large-scale galaxies, it is not surprising that the Sersic index is $\sim$ 0.4 and therefore less than 1. The outer part of the galaxy is found to be well described with an $n = 1$ Sersic profile. In the discovery paper, the ELLIPSE task

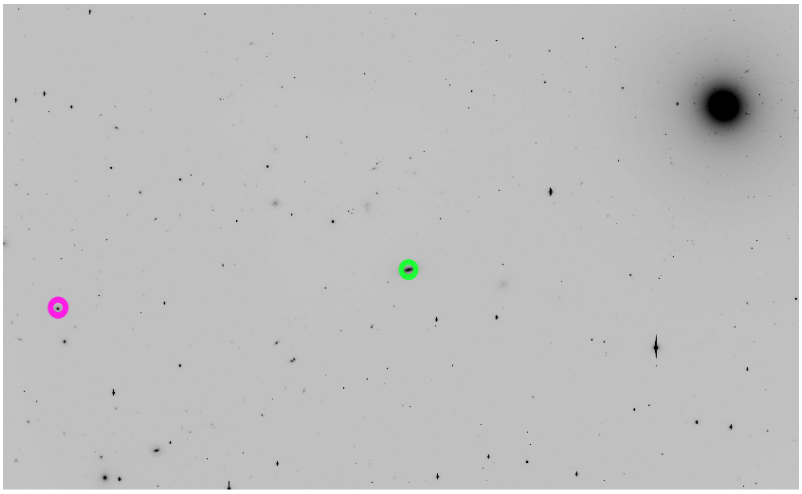

Figure 4.1.: The giant massive galaxy seen in the picture is the spherical galaxy NGC 1407 (E0). The projected separation between the giant galaxy and LEDA (green) is shown to be around 50 kpc. The projected separation between the host galaxy and BM^2 (pink) is around 100 kpc.

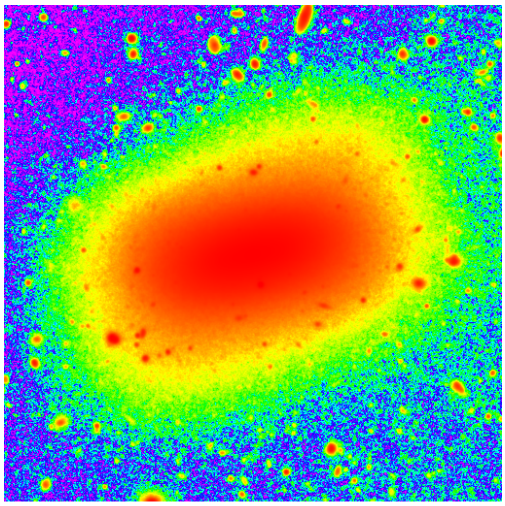

Figure 4.2.: A 120×120 arcsecond (∼12×12 kpc) i-band image of LEDA 074886. North is up and East is left. NGC 1407 is located ∼50 kpc to the NW.

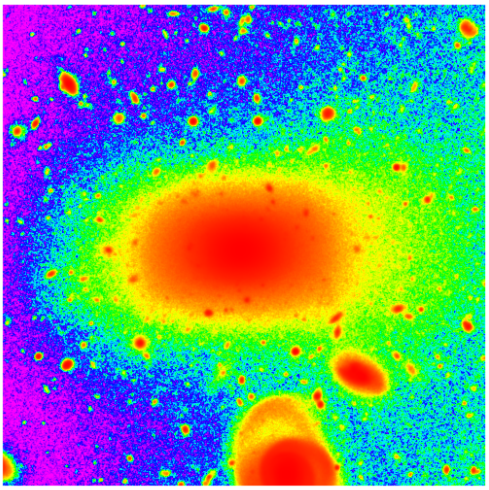

Figure 4.3.: A 50×50 arcsecond (∼5×5 kpc) i-band image of BM^2. North is up and East is left. NGC 1407 is located ∼100 kpc to the NW.

was used to approximate the isophotes using a Fourier series approach similar to the method used by the program BELLE. In this technique the isophotes found in the galaxy are approximated with a Fourier series

$$I(\theta) = I_0 + \sum_{n=1}^{\infty} (A_n \cos n\theta + B_n \sin n\theta) \tag{4.1}$$

where θ is the azimuthal angle and I_0 is the average intensity over the ellipse. The A_4 coefficient to the $\cos 4\theta$ Fourier component is used to quantify the isophotal deviation from an ellipse. It is positive (negative) when the isophotes are discy (boxy). In this paper they 'normalised' the A_4 coefficient to the $\cos 4\theta$ Fourier component by the semi-major axis length a to give A_4/a. It is not quiet understood why they write about normalisation since A_4/a clearly does not give a dimensionless number as the variable A_4 must be in units of luminosity and a is in units of length. The parameter A_4/I_0 however is a unitless number. It has been used in the analysis of the boxiness of the simulations presented in this thesis as well as the observations since it appears to be a more natural choice. The authors find that the inner disk in LEDA 074886 has a peak ellipticity of 0.65 and isophotes with A_4/a peaking at +0.022 at 3.5" (see figure 4.4). Beyond the inner disk around 8" the A_4/a term becomes increasingly negative and therefore boxy. The boxiness parameter reaches values of -0.05 by 30" and -0.08 by 53" at which point the galaxy light appears to truncate rapidly.

The Observations with the giant Keck Telescope in Hawaii, revealed a rapidly spinning, thin disc which reaches a rotation velocity of 33±10 km s^{-1} by a radius of ∼5 arcseconds.

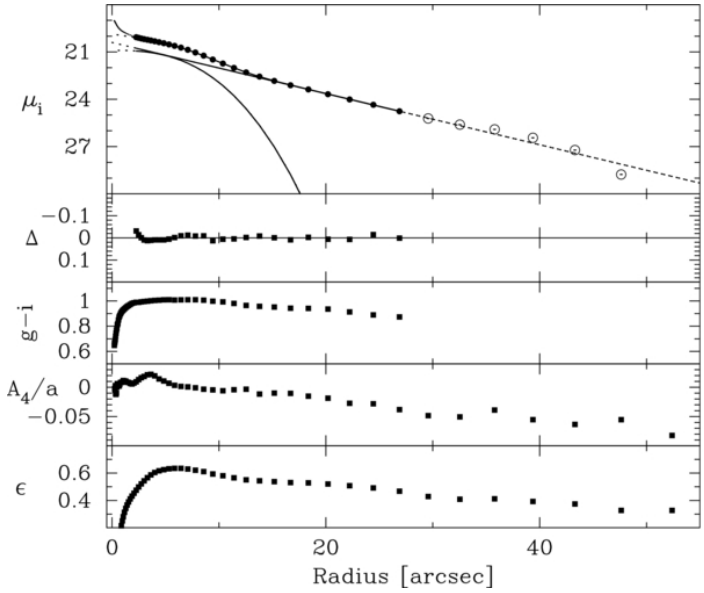

Figure 4.4.: Major-axis, *i*'-band light profile for LEDDA 074886 fit with a Sersic model ($n_{\text{inner}} = 0.4$, $R_{\text{e, inner}} = 5.8''$, $\mu_{\text{e, inner}} = 21.4$ mag arcsec^{-2}) for the inner embedded disk, plus an exponential model for the outer host galaxy ($h_{\text{outer}} = 6.7''$ $\mu_{0,\text{ outer}} = 20.4$ mag arcsec^{-2} $\rightarrow$ $R_{\text{e, outer}} = 11.2''$, $\mu_{\text{e, outer}} = 22.2$ mag arcsec^{-2}. An additional nuclear component is present, but has been excluded from the fit over the inner $2''$. The residuals Δ about the fit are shown in the second panel. The $g' - i'$ colour, A_4/a boxiness parameter, and ellipticity are shown in the subsequent panels. The scale is such that $10'' = 1.01$ kpc, which is roughly the galaxy's major-axis half light radius.

Despite the obvious boxiness of the galaxy it has been challenging to quantify the unlikely nature of the rectangular shape of the emerald cut galaxy. There has however not been many large quantitative studies on the boxiness of galaxy isophotes. In the literature (Liu et al., 2008) the boxiness parameter generally was observed to be confined to > -0.02. Possibly the largest study found looking at the distribution of a_4/a[1] parameters is the analysis from Hao et al. (2006) of 847 luminous early type galaxies, in which the bulk have a_4/a > -0.01 with just 2.2% of the sample having $-0.02 < a_4/a < -0.01$. It has to be noted that a single boxiness parameter such as a_4/a can be somewhat limited as sometimes the boxiness parameter can show a radial change. This can lead to a misidentification of extremely boxy galaxies if only their outer or inner isophotes are boxy, which is the case with LEDA 074886. In figure 4.5 the location of LEDA 074886's outer isophotes in the ellipticity-a_4/a diagram

[1]The a_4/a is the intensity-weighted mean value across a galaxy, typically measured from 2 seeing radii to 1.5 half-light radii.

and the absolute magnitude-a_4/a diagram is shown. The values for the Virgo cluster galaxies are roughly the median values from 1.41 to 2.82 R_e, rather than the average value within 1.5 R_e. In further work the authors attempt to acquire deeper images of the more boxy Virgo galaxies, and determine how their A_4/a profiles behave with increasing radius. The authors also listed all found squarish galaxies they could find

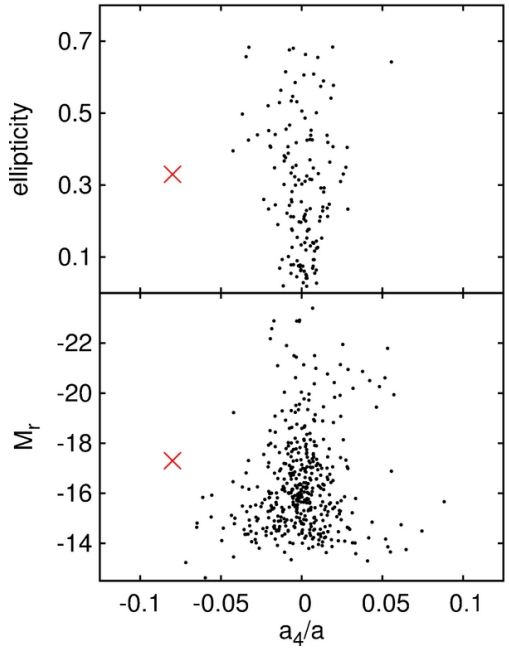

Figure 4.5.: The rare nature of LEDA 074886's rectangular-shape can be seen by contrasting its location, denoted by the cross, with that of Virgo cluster early-type galaxies in the ellipticity - (a_4/a) and magnitude - (a_4/a) diagram. The 475 Virgo cluster galaxies (lower panel) are described in Janz & Lisker (2008). For comparison with similarly bright galaxies, the upper panel shows the 166 Virgo cluster galaxies with $-19 < M_r < -16$ mag. Note: The R-band magnitude for LEDA 074886 (-17.3 mag) has been used here, along with its ellipticity and A_4/a values at $52''$.

in the literature

- SDSS J07418.17+282756.3
- Sextans A
- VCC 1699
- NGC 5322, NGC 4270
- NGC 4488

- UGC 5119
- IC 3370

Comparing all those galaxies with LEDA 074886 the authors noted that most of the galaxies listed above do not match their appearance. IC 3370 is however the closest match to LEDA 974886 although it is not a dwarf galaxy.

The authors suspect that the most possible scenario to explain the presence of LEDA 074886 is a near edge-on merger, coupled with the right viewing angle. The simulations by Naab et al. (2006a) which used inclined mergers of 30 degrees generated boxy galaxies. They therefore suspect that LEDA 074886 may have formed from disks that merged in a plane, coupled with gas that dissipated to form the new inner disk. This dissipation in the plane would preferentially adiabatically contract the long axis of the new galaxy. The work of several authors (Jesseit et al., 2005; Naab et al., 2006a; Hoffman et al., 2010) showed that major mergers of disk galaxies can, in the presence of $15\% - 20\%$ gas, generate early-type slowly rotating galaxies with kinematically distinct cores. They also showed that doubling this gas fraction results in galaxies with sharp embedded disks on the $\sim R_e$ scale. They however resemble dissipationless mergers, i.e., boxy, at large radii where no effect by gaseous star formation can be seen. Such a hybrid model with star formation in the inner regions and a 'dry' merger event at larger radii, may be plausible explanation for LEDA 074886.

5. Simulations

The numerical simulations described in this chapter were performed to study various scenarios that could have lead to the formation of LEDA 074886. Because of its boxy outer part and discy stellar central region, the galaxy shows characteristics of two different types of galaxy mergers. N-body simulations as discussed by Jesseit et al. (2005) have shown that boxy orbits are most likely to form by major mergers with an declination angle of 30 degree. They also found that a larger pericentral distance supports the formation of boxy galaxies. Because such dry mergers only contain collisionless particles they cannot explain the presence of a stellar discy center in the middle of the galaxy. Naab et al. (2006b) performed simulations with gas finding that the presence of gas in mergers has a significant impact on the orbital structure. Generally, they found that gas destroys the box orbits at the center of the galaxies and minor axis tubes become more populated. They have shown that in contrast to the collisionless case, equal mass mergers with gas do not result in very boxy remnants. Hoffman et al. (2010) showed that equal mass mergers of disk galaxies can in the presence of 15%-20% gas, generate early-type slowly rotating galaxies with kinematically distinct cores. They also noted that as the gas fraction increases, the box orbits in the center of the galaxy are increasingly replaced by a sharp embedded disk. It was also shown that the outer parts of the remnants are less relaxed than the inner parts, and are therefore largely unaffected by the gas content of the disks. Such a scenario described by Hoffman et al. (2010) therefore seems to be likely to have formed LEDA 074886.

Building on the work of Jesseit et al. (2005); Naab et al. (2006a); Hoffman et al. (2010) we have performed a variety of major mergers with a gas fraction of 10%, 15%, and 20%. The spins of the two merging galaxies either pointed along the same axis (up-up; s_1) or opposite to each other (up-down; s_2). The initial condition code introduced by Springel & Hernquist (2005) was used to produce the particle distribution of an isolated galaxy. The code assumes an NFW profile for the galaxy with an exponential disc, and a spherical, non rotating bulge. The general parameters to generate the isolated galaxy are

```
/*****************************************                    */
CC=      16.;      halo concentration    (NFW DM Halo only)    */
V200=    12.5;     circular velocity v_200 (in km/sec)         */
                   (NFW DM Halo + baryons)                     */
LAMBDA= 0.085;     spin parameter                              */
MD=      0.08;     disk mass fraction                          */
MB=      0.01;     bulge mass fraction                         */
JD= MD;            disk spin fraction                          */
                                                               */
GasFraction=0.1 ;relative content of gas in the disk           */
DiskHeight= 0.1 ;thickness of disk in units of radial scale length  */
```

```
BulgeSize=  1.0 ;bulge scale length in units of disk scale length    */
                                                                     */
N_HALO= 1000000; desired number of particles in dark halo            */
N_DISK=  500000; desired number of collisionless particles in disk   */
N_GAS=   100000; number of gas particles in disk                     */
N_BULGE=  62500; number of bulge particles                           */
                                                                     */
HI_GasMassFraction=      0.1;/* in terms of the total gas mass      */
HI_GasDiskScaleLength=   1.0;/* in terms of scale length of the disk */
                                                                     */
Qstabilizefactor=1.5;                                                */
/*************************************                               */
```

where v_{200} is the virial velocity of the galaxy which also sets the halo mass and the virial radius r_{200} through

$$M_{200} = 2.33 \times 10^5 V_{200}^3 M_\odot \tag{5.1}$$

and

$$v_{200} = \sqrt{\frac{GM_{200}}{r_{200}}} \tag{5.2}$$

The *cc* concentration determines the radial scale of the halo as $cc = r_{200}/r_s$ where r_s is the bulge radius.

The simulations have all been performed with the RAMSES code previously discussed and using the cooling mechanism as described by Sutherland & Dopita (1993). The functions implemented to describe the cooling mechanism covers a wide grid of temperature and metallicities using published atomic data and processes. For the AMR simulation, a minimum level of 7, and a maximum level of 15 was used. With a boxsize of 1.095×10^3 kpc, the highest spacial resolution per grid is $0.33\,kpc$[1].

An isolated dry disk was first simulated to test the stability of the initial conditions. Such an isolated run was repeated with gas and star particles in the galaxy with a gas fraction of 10%.

Next, two isolated galaxies were set up with the RAMSES **merger** patch. In doing so, the particle distribution of the isolated galaxy is translated and duplicated for the spacial distribution given in the MERGER_PARAMS in the namelist file and calculated as explained above. The gas distribution of the galaxy was calculated within the merger patch using an analytical function which is a function of the particle distribution. The initial total velocity `Vgal1` and `Vgal2` also had to be specified.

```
&MERGER_PARAMS
rad_profile='exponential'
z_profile='exponential'
gal_center1=0.0,75.0,0.0
gal_center2=0.0,-75.0,0.0
Mgas_disk1=0.039803
Mgas_disk2=0.039803
typ_radius1=0.505809
typ_radius2=0.505809
cut_radius1=1.5
```

[1] boxlen/($2^2 \cdot$ levelmax) = 0.33 kpc

```
cut_radius2=1.5
typ_height1=0.168603
typ_height2=0.168603
cut_height1=0.5
cut_height2=0.5
IG_density_factor=1.0d-4
Vcirc_dat_file1='Vcirc1.dat'
Vcirc_dat_file2='Vcirc2.dat'
ic_part_file_gal1='ic_part1'
ic_part_file_gal2='ic_part2'
gal_axis1=0.0,0.0,1.0
gal_axis2=0.0,0.0,-1.0
Vgal1=4.6752588471390348,-11.919618046329621,0.0
Vgal2=-4.6752588471390348,11.919618046329621,0.0
```

The merging of two galaxies was first demonstrated with a pure N-body simulation. The galaxies were placed on parabolic orbits with an initial separation of $r_{\text{sep}} = 300$ kpc and a pericenter distance of $r_p = 5$ kpc. With this initial configuration and assuming $z = 0$ the spacial position for galaxy 1 and 2, as well as the velocity can be calculated with as

$$\begin{aligned} r_{1y} &= 150 \\ r_{2y} &= -\frac{M_1}{M_2} r_{1y} \\ \dot{r}_{1y} &= \sqrt{\frac{GM_1}{r} - \frac{Gr_p M_1^2}{8\mu r_{1y}^2}} \\ \dot{r}_{2y} &= -\dot{r}_{1y} \\ \dot{r}_{1x} &= -\frac{M_1}{4\mu r_{1y}} \sqrt{2\mu G r_p} \\ \dot{r}_{2x} &= -\dot{r}_{1x} \end{aligned} \tag{5.3}$$

with $\mu = (M_1 M_2)/(M_1 + M_2)$.

Because of technical issues, these pure N-body simulations can, unfortunately, not be presented in this thesis. After testing the stability of the initial conditions as well as the plausibility of the merger path, simulations (merger_s1_fgas10, merger_s2_fgas10, merger_s1_fgas15, merger_s2_fgas15, merger_s1_fgas20, merger_s2_fgas20) with a gas fractions of 10%, 15%, and 20% were performed each with varying orientation (s_1, s_2) of the rotation angle of the galaxy.

Additionally two simulations (merger_s1_fgas10_fb, merger_s2_fgas10_fb) were performed using the feedback mechanism implemented in RAMSES described in Dubois & Teyssier (2008c). It accounts for star formation, supernova thermal feedback, and supernova kinetic feedback.

A further two simulations (merger_s1_box_fb, merger_s2_box_fb) were performed using the new initial condition code patch developed during this thesis. These simulations were also run with the feedback mechanism described above. The new initial conditions patch differs from the merger patch already in RAMSES because it extracts the AMR grid directly from a source output, rather than simply fitting an analytical function over the particle distribution.

A region from the last output of the feedback run was extracted, translated, rotated and duplicated such that the two galaxies merged with each other at an inclination angle of 15°. The initial condition parameters GALAXY_DUP_PARAMS had to be specified, indicating the spacial distance between the two boxes, initial position, and velocity as well as specifying the size of the box to be extacted:

```
&GALAXY_DUP_PARAMS
rad_profile='exponential'
z_profile='exponential'
galaxy_repository='../merger_s1_fgas10_fb3/output_00121/'
source_gal_center=0.0,0.0,0.0
source_gal_radius=12.0
gal_center1=0.0,75.0,0.0
gal_center2=0.0,-75.0,0.0
gal_axis1=0.0,1.0,1.504
gal_axis2=0.0,1.0,1.504
Vgal1=4.6752588471390348,-11.919618046329621,0.0
Vgal2=-4.6752588471390348,11.919618046329621,0.0
Vcirc_dat_file1='Vcirc1.dat'
Vcirc_dat_file2='Vcirc2.dat'
ic_part_file_gal1='ic_part1'
ic_part_file_gal2='ic_part2'
/
```

6. Results

In this chapter we present the results obtained throughout this thesis. We first discuss the results from analysing the boxiness of the observational data and compare this with the results presented in the original discovery paper. We show the analysis of the newly discovered rectangular galaxy BM^2. The main part of this chapter however, is the analysis of the simulated data. We performed various equal mass (major) mergers with three different gas fractions 10%, 15%, and 20%. Each gas fraction was simulated in two different ways by changing the rotation angle of the two galaxies, where s_1 denotes the same orientation (up, up) of the two rotation axes of the galaxies and s_2 denotes the counter orientation (up, down) of the two rotation axes. In order to study the effect of feedback mechanisms on merger remnants with regard of their boxiness two simulations were also performed with the feedback mechanism described by (Dubois & Teyssier, 2008b) with a gas fraction of 10%. Two other simulations have been performed by cutting out a box of the final output from the feedback simulation, rotating, translating and duplicating the galaxy to again merge them together with an equal orientation of the rotation axes as well as an opposite rotation of the two axes. Each individual simulation was analysed in various ways regarding its boxiness. First the boxiness as a function of the radius of one specific output was analysed. This analysis was only done for the star particles in the simulation as such an analysis is similar to the one performed in the paper of (Graham et al., 2012) and can also be compared to the analysis of the observations performed with our program BELLE. The program also was used to test whether in our simulations different orbit classes dominate at different radii inside the merger remnants, as claimed by several authors Barnes & Hernquist (1992). Secondly, the boxiness was analysed as a function of time for six different radii. The purpose of this analysis was to better understand the evolution of the boxiness over time and position within the galaxy. The third analysis was supposed to test the assumption of Jesseit et al. (2005) regarding the different viewing angle. They claimed that the principal axis of the merger remnants would result in the most extreme boxiness values of all possible projections. For this purpose the galaxy was analysed at different radii from different viewing angles by sampling a sphere or line-of-sight (los) axis. In order to make this five dimensional analysis understandable, the calculated maximum, minimum, and mean value of the boxiness parameter a_4 was plotted as a function of four different radii.

6.1. Observations

6.1.1. LEDA 074886

In figure 6.1 the analysis of the boxiness parameter is shown. Comparing this analysis with the analysis done in the paper shown in figure 4.4 one can immediately see the difference in scales. The maximum boxiness in (Graham et al., 2012) is calculated to be -0.08 at 53", where the scale is such that 10" = 1.01 kpc, which is roughly the galaxy's major-axis half light radius. The maximum boxiness calculated with BELLE and shown in the lower plot of figure 6.1 is however -0.8 around 5.2kpc. We could not explain this order of magnitude of difference, despite private communications with the original authors. A few things are of note. In the paper they stated that they plotted the A_4 coefficient to the $\cos 4\theta$ Fourier component normalised by the semi-major axis length a to give A_4/a. This parameter was used to quantify the isophotal shape. Looking at the the units of the two variables where A_4 must be in units of luminosity and a is in units of length it is clear that A_4/a is not a unitless number. The parameter A_4/I_0 however is a unitless number. In the upper plot of figure 6.1 the parameter A_4/a is shown as a function of the radius. Comparing with the shape of the curve presented in the paper those two curves look nothing alike. If however the A_4/I_0 parameter is compared with the A_4/a parameter presented in the paper the two curves look very much alike having maxima at similar positions and showing the same trend of boxier galaxies the further out one goes in radius. For all the future comparisons of the simulations the normalised parameter A_4/I_0 was used.

6.1.2. BM^2

In figure 6.2 the analysis of the parameter A_4/a, and A_4/I_0 is shown as a function of the radius. It can be seen that the boxiness of BM^2 is not a strong as the boxiness of LEDA 074886. In fact the maximum boxiness is around -0.2 at 2.2kpc whereas the maximum boxiness of LEDA 074886 was calculated to be -0.8. The analysis of this galaxy shows that the boxiness of a galaxy cannot be purely determined by eye. A boxy looking galaxy does not necessarily give rise to a big boxiness parameter.

6.2. Collisional Runs

In order to study various scenarios that could have lead to the formation of LEDA 074886 a number of simulations have been carried out. It already has been found that the presence of gas has a significant impact on the orbital structure of the merger remnant (Naab et al., 2006a). Generally, they found that gas destroys the box orbits at the center of the galaxies and minor axis tubes become more populated. In contrast to collisionless equal mass mergers, major mergers with gas do not result in very

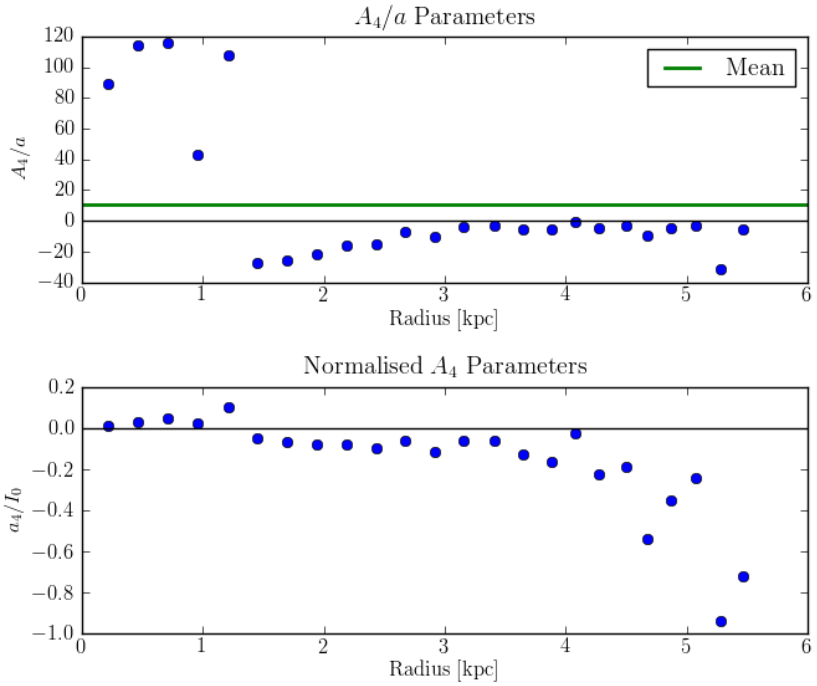

Figure 6.1.: Analysis of the boxiness parameter for LEDA 074886. The upper plot shows the A_4/a parameter as a function of the radius. The lower plot shows the A_4/I_0 parameter as a function of the radius.

boxy remnants. Building on the work of Naab et al. (2006a), Hoffman et al. (2010) found that equal mass mergers of disk galaxies can in the presence of 15%-20% gas, generate early-type slowly rotating galaxies with kinematically distinct cores. They also noted that as the gas fraction increases, the box orbits in the center of the galaxy are increasingly replaced by a sharp embedded disk. They however also show that the outer parts of the remnants are largely unaffected by the gas content of the disks leading to a more boxy outer region. Since LEDA 074886 shows a boxy outer part and a discy stellar central region the scenario described by Naab et al. (2006a) seems to be likely. Building on this work and to further test the effect of gas we performed collisional simulations with a various gas fraction of 10%, 15%, and 20%. For all the simulations the same analysis has been carried out. In each case the different density maps of the stellar as well as the dark matter distributions are shown for the different los axis directions. The A_4/I_0 parameter was analysed as a function of the radius at one given output for the stellar density distribution. The results of the analysis are again shown for the different los axis directions. Additionally the A_4/I_0 was studied as a function of time for different radii for the stellar as well as the dark matter

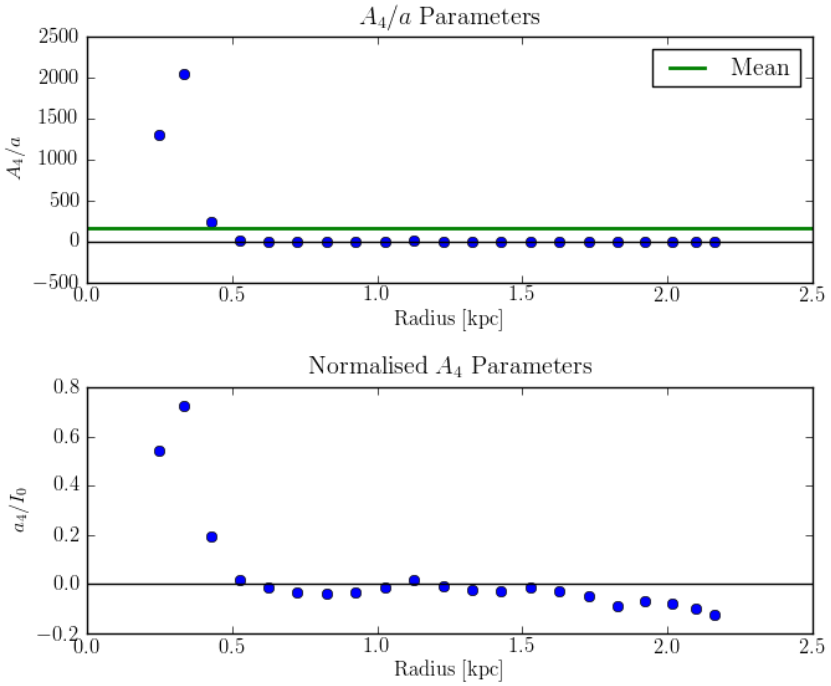

Figure 6.2.: Analysis of the boxiness parameter for BM^2. The upper plot shows the A_4/a parameter as a function of the radius. The lower plot shows the A_4/I_0 parameter as a function of the radius.

distribution. In all the plots $r_i = i/6 \cdot r_{\mathrm{hl}}$, for $i \in [1, 6]$ and where r_{hl} is the half light radius of the last output for the stellar and dark matter distribution calculated for all the los axis directions accordingly. It is important to stress that each noted radii (r_i) of one los axis direction is the same as the noted radii r_i of another los axis direction. For the stellar particles the effect of the viewing angle on the boxiness parameter is also calculated. For this the surface of the sphere of all the possible los axis directions had to be sampled uniformly. To sample one vector, the points x, y, and z are calculated by choosing

$$\begin{aligned} x &= \sqrt{1-u^2}\cos\theta \\ y &= \sqrt{1-u^2}\sin\theta \\ z &= u \end{aligned} \tag{6.1}$$

with $\theta \in [0, 2\phi)$ and $u \in [-1, 1]$. In the analysis presented here 20 different θ angles as well as 10 different u were uniformly chosen. The pictures show the possible change of the boxiness as a function of the different radii. The errorbars are calculated as the

maximum and minimum value of all the possible A_4/I_0 parameters found when varying θ and u. The circle in the middle denotes the mean value of all the different A_4/I_0 parameters. For the dark matter distribution the study of the triaxiality as a function of time is also shown for different radii. Here again $r_i = i/6 \cdot r_{\rm hl}$, for $i \in [1, 6]$ for the half light radius for the dark matter distribution calculated from the last output.

6.2.1. merger_s1_fgas10

The analysis of the stellar particles from the simulation with a 10% gas fraction and the two rotation vectors pointing in the same direction can be seen in figure 6.3. Looking at the parameter A_4/I_0 as a function of the radius for the different los axis (x-direction, 6.3d, 6.3e, and 6.3f) one can see that this remnant is not boxy. This can also be confirmed when looking at the stellar density map of the merger remnant (6.3a, 6.3b, and 6.3c). Only in the los axis in z direction (6.3c) a slightly negative A_4/I_0 value can be observed. The position of these negative values correspond however to the star forming sites within the galaxy. It can be assumed that the forming stars disturb the isophotal shape which can lead to a negative A_4/I_0 parameter. The analysis of the A_4/I_0 parameter as a function of time for different radii is shown in in the plots (6.3g, 6.3h, and 6.3i). Looking at the different los axis directions one can generally see that the fluctuations at smaller radii are smaller than at larger radii, but they never become significantly negative. In the analysis of the A_4/I_0 parameter as a function of the angle it can be seen that the A_4/I_0 parameter varies more at the outskirts of the galaxy. The range of the parameter is from -0.3 to 0.3 in the outer parts of the galaxy and from -0.15 to 0.1 in the inner parts of the galaxy.

The A_4/I_0 parameter analysis as a function of time for the different los in directions of the dark matter particles is shown in figures (6.3g, 6.3h, and 6.3i). Finding a significant trend in the analysis of the A_4/I_0 parameter with time is difficult. One can see that the A_4/I_0 parameter only ever becomes negative for the los axis in the z direction, otherwise the fluctuations are in the positive region and span a range from 0.0 to 0.4, and a range from -0.1 to 0.6 for the A_4/I_0 parameter for the los axis in the x direction, and y direction, respectively. The triaxiality as a function of time for different radii is shown in figure 6.4g. Here it can be seen that the triaxiality at different radii are faintly tracing each other. The shape of the dark matter halo therefore does not change as a function of radius. The triaxiality ranges from a minimum of 0.85 to a maximum of 1.0 bearing a prolate shape of the halo.

6.2.2. merger_s2_fgas10

The full analysis of the simulations of the stellar particles, and the dark matter particles for a gas fraction of 10% and the two rotation vectors pointing opposite to each other can be seen in figures 6.5, and 6.6, respectively. Observing the parameter A_4/I_0 over time (6.5d, 6.5e, and 6.5f) one can see that the parameter is above zero at all the different radii for this output for the two los axis directions x, and y. The A_4/I_0 parameter ranges from 0.01 - 0.05, and 0.02 - 0.06 at the two los axis directions x, and y. Only in the los axis direction of z does the parameter become zero, at

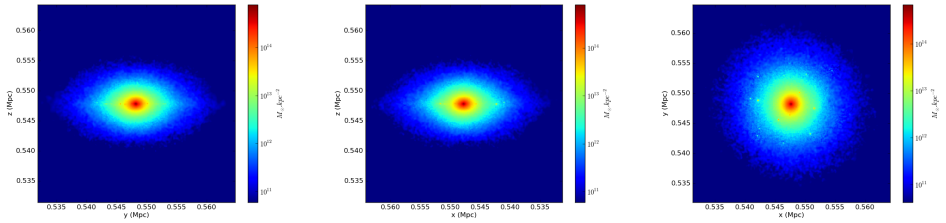

(a) Density map of the stars with los axis in x direction.

(b) Density map of the stars with los axis in y direction.

(c) Density map of the stars with los axis in z direction.

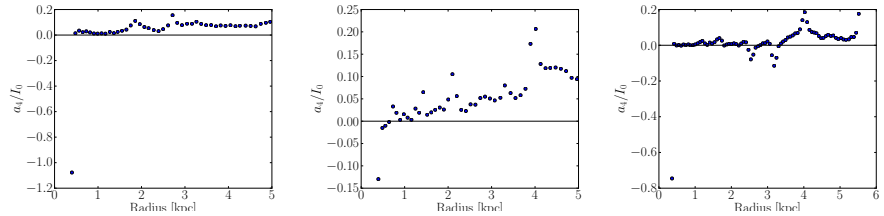

(d) Analysis of the A_4/I_0 parameter as a function of radius for the los axis in x direction.

(e) Analysis of the A_4/I_0 parameter as a function of radius for the los axis in y direction.

(f) Analysis of the A_4/I_0 parameter as a function of radius for the los axis in z direction.

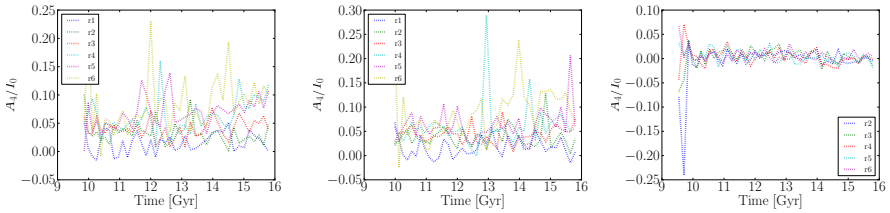

(g) Analysis of the A_4/I_0 parameter as a function of time for different radii in x direction.

(h) Analysis of the A_4/I_0 parameter as a function of time for different radii in y direction.

(i) Analysis of the A_4/I_0 parameter as a function of time for different radii in z direction.

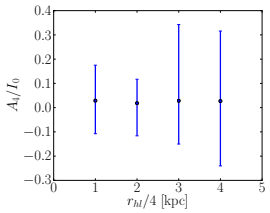

(j) Analysis of the A_4/I_0 parameter as a function of the different viewing angle and the radii.

Figure 6.3.: Analysis of the stars from the simulation with a 10% gas fraction and the two rotation vectors pointing in the same direction.

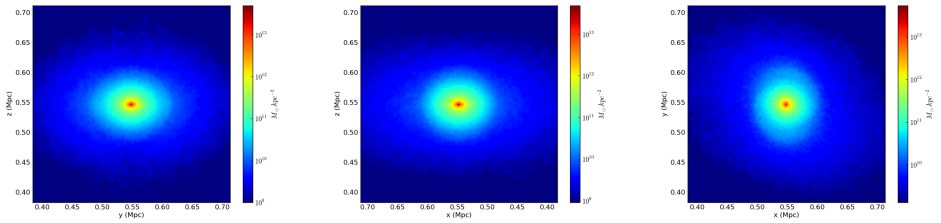

(a) Density map of the dark matter praticles with los axis in x direction.

(b) Density map of the dark matter particles with los axis in y direction.

(c) Density map of the dark matter particles with los axis in z direction.

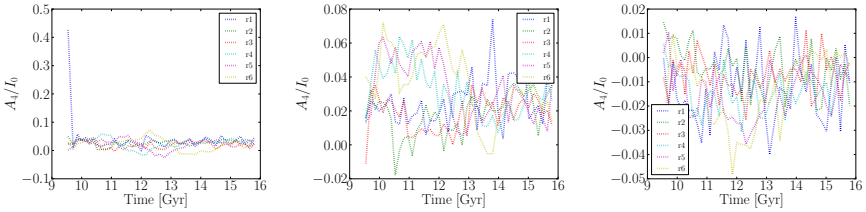

(d) Analysis of the A_4/I_0 parameter as a function of time for different radii in x direction.

(e) Analysis of the A_4/I_0 parameter as a function of time for different radii in y direction.

(f) Analysis of the A_4/I_0 parameter as a function of time for different radii in z direction.

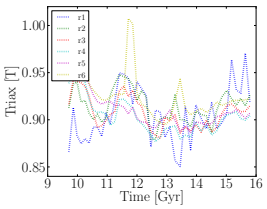

(g) Analysis of the triaxiality parameter as a function of time for different radii.

Figure 6.4.: Analysis of the dark matter from the simulation with a 10% gas fraction and the two rotation vectors pointing in the same direction.

times reaching its most negative part at small radii with an A_4/I_0 parameter of -0.01. Comparing the position of the negative parameters and the star formation sites one can again see a correlation. It can be assumed that the star formation again caused the A_4/I_0 parameter to reach negative values. Looking at the analysis of the A_4/I_0 parameter with time (6.5g, 6.5h, and 6.5i) for different radii one observes that the different parameters at the different radii remarkably track each other for both los axis directions x, and y. Looking at the analysis for the los axis direction z one can see that the outer most radii almost inversely track the inner regions. Especially for the los axis direction z the A_4/I_0 parameter reaches very low numbers. An analysis of the output with the most negative parameter has been attempted. The parameters at this output generally fluctuated very strongly for most of the radii reaching very high and very low values at the same time. Because of this observed chaos one can assume that the galaxy was not relaxed at the time where a lot of movement was still underway until the galaxy relaxed in its state (last output). From the ranges of the different parameter when observing the different los axis orientations (6.5j) one can see that the range between the maximum and minimum value at the different radii is comparable, where the maximum difference at the smallest radius ranges from -0.06 to 0.06.

The A_4/I_0 parameter as a function of time for the dark matter particle distribution is harder to interpret as no significant tracking can be observed (6.6a, 6.6b, and 6.6c). For all of the los axis directions no significant trend can be observed. Looking at the triaxiality parameter as a function of time (6.6g) one can however see that the inner part of the galaxy has a lower triaxiality, 0.85 at the minimum, than the outer part of the galaxy with a maximum value being 1.0 (prolate orbit).

6.2.3. merger_s1_fgas15

The results of the stellar analysis of the simulations with a gas fraction of 15% and the two rotation axes of the galaxies pointing in the same direction can be seen in figure 6.7. Figures 6.7d, 6.7e, and 6.7f show the result of the analysis of the A_4/I_4 parameter as a function of the radius at a given output. Where the A_4/I_0 parameter for the los axis direction x and y is not negative it is negative for some intermediate radius and large radius for the los axis direction z. The range of the parameter in the los axis direction z lies between 0.01 and -0.09. The results of the A_4/I_0 parameter analysis as a function of time is shown in figures 6.7g, 6.7h, and 6.7i. It can be observed that the general trend of this galaxy for the A_4/I_0 parameter is to oscillate around zero with the mean value at zero. Specially when looking at the analysis of the A_4/I_0 parameter in the los axis orientation in direction z one can see that the largest fluctuations are in the center of the galaxy. This observation is opposite to the observation made when looking at the range of the possible parameters for different los axis directions as a function of the radius (6.7j. Here it can be observed that the parameter has the largest fluctuations for larger radii where the maximum range lies between -0.2 to 0.2. These observations suggest that even though the galaxy obviously experiences stages where the A_4/I_0 parameter at larger radii could be useful when comparing with the observational data, the boxiness of this galaxy is surely not stable. Nevertheless this

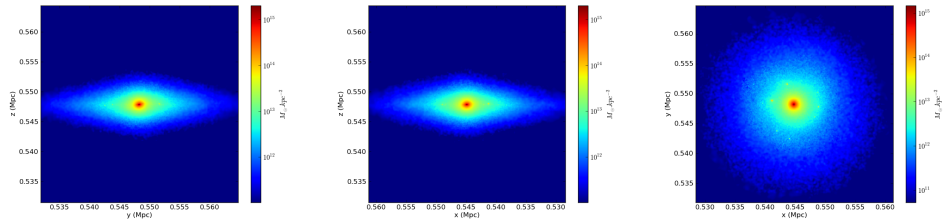

(a) Density map of the stars with los axis in x direction.

(b) Density map of the stars with los axis in y direction.

(c) Density map of the stars with los axis in z direction.

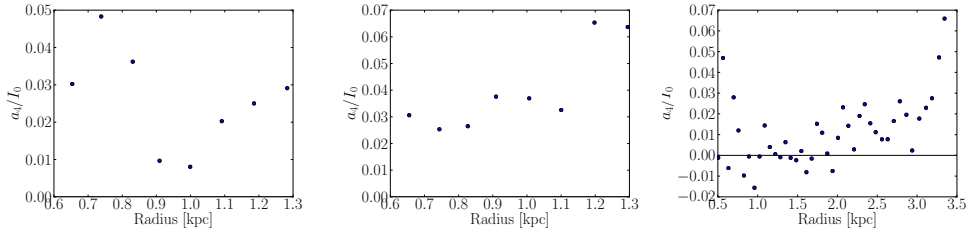

(d) Analysis of the A_4/I_0 parameter as a function of radius for the los axis in x direction.

(e) Analysis of the A_4/I_0 parameter as a function of radius for the los axis in y direction.

(f) Analysis of the A_4/I_0 parameter as a function of radius for the los axis in z direction.

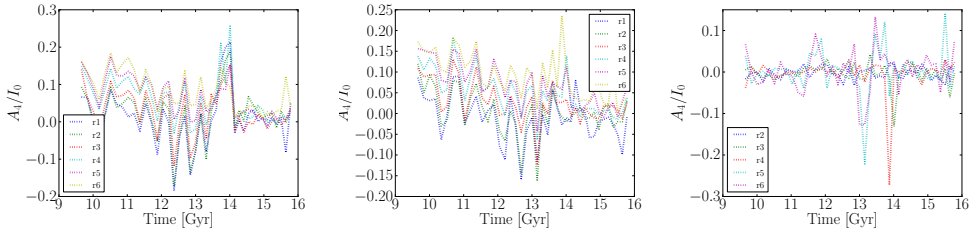

(g) Analysis of the A_4/I_0 parameter as a function of time for different radii in x direction.

(h) Analysis of the A_4/I_0 parameter as a function of time for different radii in y direction.

(i) Analysis of the A_4/I_0 parameter as a function of time for different radii in z direction.

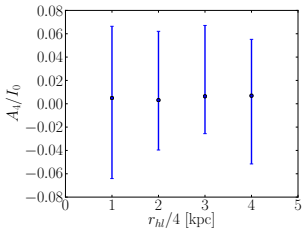

(j) Analysis of the A_4/I_0 parameter as a function of the different viewing angle and the radii.

Figure 6.5.: Analysis of the stars from the simulation with a 10% gas fraction and the two rotation vectors pointing in the opposite direction.

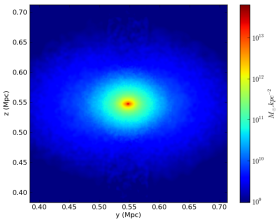

(a) Density map of the dark matter particles with los axis in x direction.

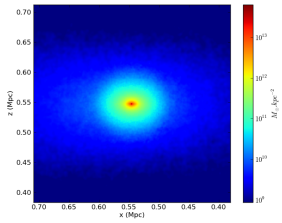

(b) Density map of the dark matter particles with los axis in y direction.

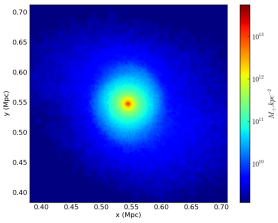

(c) Density map of the dark matter particles with los axis in z direction.

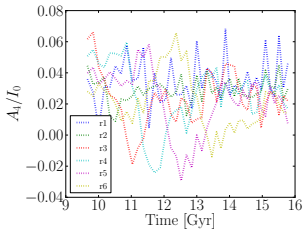

(d) Analysis of the A_4/I_0 parameter as a function of time for different radii in x direction.

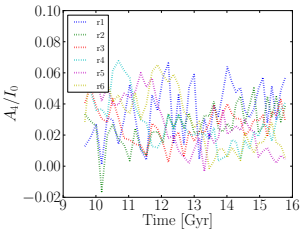

(e) Analysis of the A_4/I_0 parameter as a function of time for different radii in y direction.

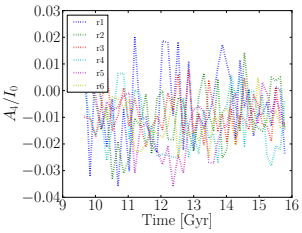

(f) Analysis of the A_4/I_0 parameter as a function of time for different radii in z direction.

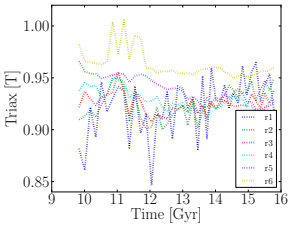

(g) Analysis of the triaxiality parameter as a function of time for different radii.

Figure 6.6.: Analysis of the dark matter from the simulation with a 10% gas fraction and the two rotation vectors pointing in the opposite direction.

analysis did not show signs of a discy inner region.

Looking at the evolution of the A_4/I_0 parameter for the dark matter distribution with time for different radii (6.4d, 6.4e, and 6.4f) one can see a similar picture of the parameter fluctuating around zero where the relaxed state seems to be around zero. Comparing these results with the analysis of the triaxiality (6.8g) where the triaxiality seems to fluctuate around 0.95 and remembering that prolate objects are usually supported elliptical galaxies confirms that the galaxy is not boxy. Nevertheless it is important to note that the observation of LEDA 074886 is only at one point in its lifetime and we may have been extremely lucky and observed an unrelaxed state of the galaxy.

6.2.4. merger_s2_fgas15

Looking at the analysis of the A_4/I_0 parameter as a function of radius for a given output of the simulation with a 15% gas fraction and the two rotation angle pointing into the opposite direction one can see that the general value of the parameter for the los axis direction x, and y lies above zero (6.9d, and 6.9e). The values for the los axis direction z however lie chaotically scattered above and below zero (6.9f). Even even a trend can be observed it can be said that the parameter values tend to be lower at larger radii than at small radii. The values of the A_4/I_0 for the los axis direction z lie between -0.04 and 0.02. These fluctuations almost look like a statistical scattering around zero indicating for the galaxy to be generally not boxy. Looking at the figures 6.9g, 6.9h and 6.9i one can see that specially for the los axis directions x, and y the A_4/I_0 parameter is lowest at small radii and largest at large radii. They range from -0.5 to 0.1 for the los axis direction x, and -0.35 to 0.05 for the los axis direction y. The A_4/I_0 axis parameter analysis as a function of the different viewing angles for the los axis direction shows that the maximum range lies between -0.12 and 0.1 for the largest radius, where the other radii lie within a similar range. The remnant of this merger simulation can therefore show a boxy side. From the analysis it is however very unlikely for the galaxy to have a discy inner region and a boxy outer part.

The analysis of the dark matter distribution is shown in figure 6.10. Looking at the A_4/I_0 parameter as a function of time for different radii one can see a reversed picture for the los axis directions x and y than from the same analysis for the stellar particles. In other words, the A_4/I_0 parameter values are lowest for larger radii and higher for smaller radii. The minimum value is -0.03, and -0.01 whereas the maximum value is 0.08, and 0.09 for the los axis direction x and y, respectively. The boxiness of the galaxies looking from the los x and y is therefore not significant. Looking at the analysis for the los axis direction z it is hard to distinguish a general trend. The range of the possible A_4/I_0 values is from -0.04 to 0.02.

6.2.5. merger_s1_fgas20

The analysis of the stellar particles of the merger simulation with a 20% gas fraction and the rotation vectors pointing in the same direction can be seen in figure 6.11.

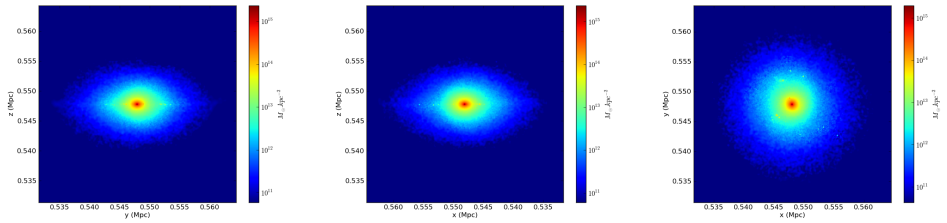

(a) Density map of the stars with los axis in x direction.

(b) Density map of the stars with los axis in y direction.

(c) Density map of the stars with los axis in z direction.

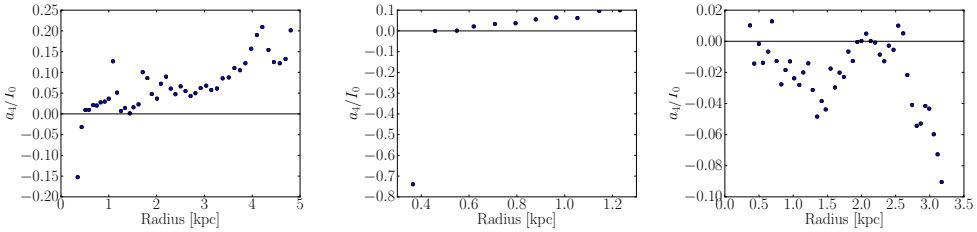

(d) Analysis of the A_4/I_0 parameter as a function of radius for the los axis in x direction.

(e) Analysis of the A_4/I_0 parameter as a function of radius for the los axis in y direction.

(f) Analysis of the A_4/I_0 parameter as a function of radius for the los axis in z direction.

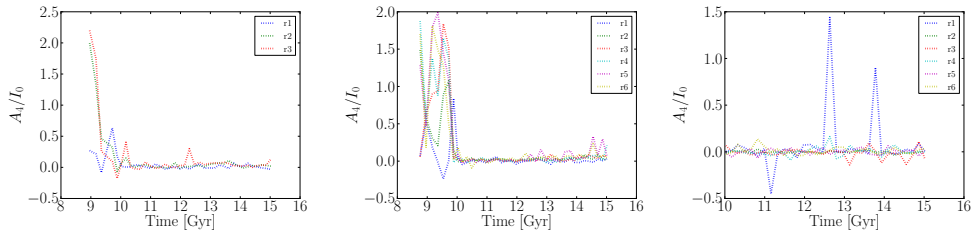

(g) Analysis of the A_4/I_0 parameter as a function of time for different radii in x direction.

(h) Analysis of the A_4/I_0 parameter as a function of time for different radii in y direction.

(i) Analysis of the A_4/I_0 parameter as a function of time for different radii in z direction.

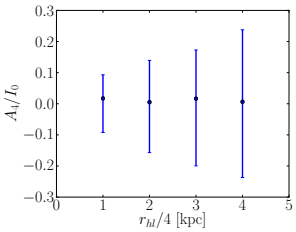

(j) Analysis of the A_4/I_0 parameter as a function of the different viewing angle and the radii.

Figure 6.7.: Analysis of the stars from the simulation with a 15% gas fraction and the two rotation vectors pointing in the same direction.

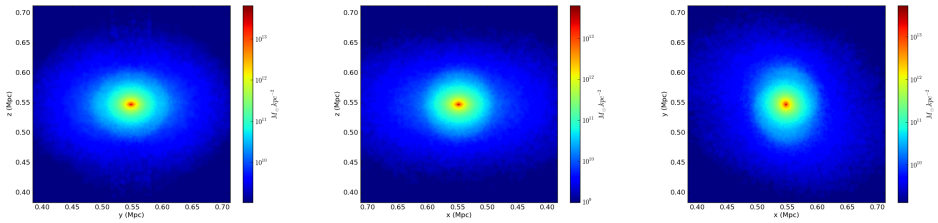

(a) Density map of the dark matter praticles with los axis in x direction.

(b) Density map of the dark matter praticles with los axis in y direction.

(c) Density map of the dark matter praticles with los axis in z direction.

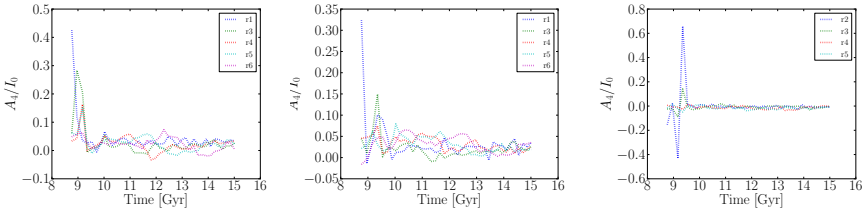

(d) Analysis of the A_4/I_0 parameter as a function of time for different radii in x direction.

(e) Analysis of the A_4/I_0 parameter as a function of time for different radii in y direction.

(f) Analysis of the A_4/I_0 parameter as a function of time for different radii in z direction.

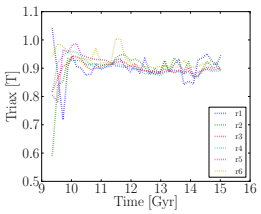

(g) Analysis of the triaxiality parameter as a function of time for different radii.

Figure 6.8.: Analysis of the dark matter from the simulation with a 15% gas fraction and the two rotation vectors pointing in the same direction.

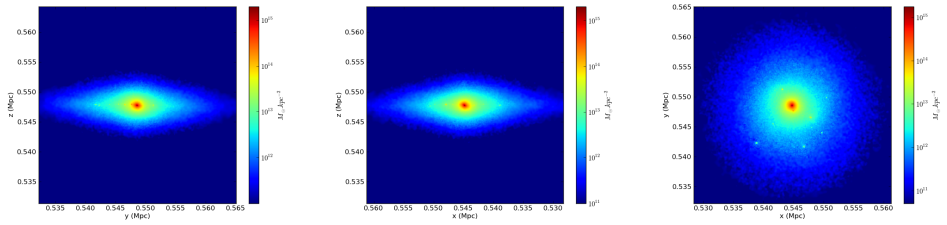

(a) Density map of the stars with los axis in x direction.

(b) Density map of the stars with los axis in y direction.

(c) Density map of the stars with los axis in z direction.

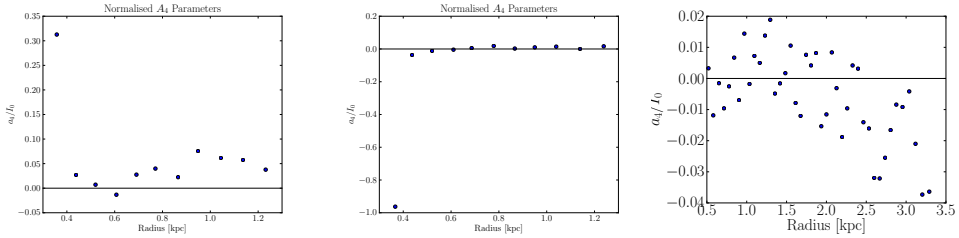

(d) Analysis of the A_4/I_0 parameter as a function of radius for the los axis in x direction.

(e) Analysis of the A_4/I_0 parameter as a function of radius for the los axis in y direction.

(f) Analysis of the A_4/I_0 parameter as a function of radius for the los axis in z direction.

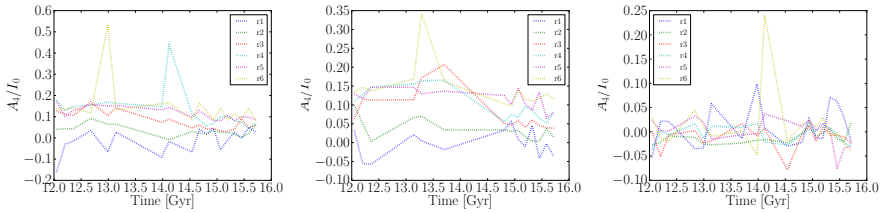

(g) Analysis of the A_4/I_0 parameter as a function of time for different radii in x direction.

(h) Analysis of the A_4/I_0 parameter as a function of time for different radii in y direction.

(i) Analysis of the A_4/I_0 parameter as a function of time for different radii in z direction.

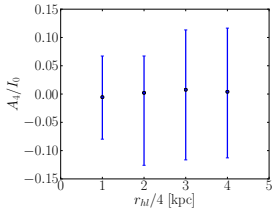

(j) Analysis of the A_4/I_0 parameter as a function of the different viewing angle and the radii.

Figure 6.9.: Analysis of the stars from the simulation with a 15% gas fraction and the two rotation vectors pointing in the opposite direction.

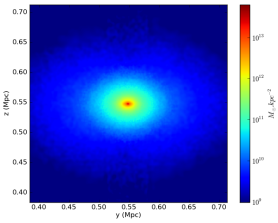

(a) Density map of the dark matter particles with los axis in x direction.

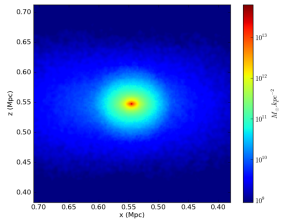

(b) Density map of the dark matter particles with los axis in y direction.

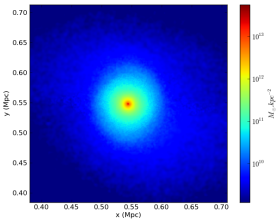

(c) Density map of the dark matter particles with los axis in z direction.

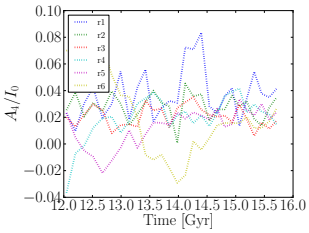

(d) Analysis of the A_4/I_0 parameter as a function of time for different radii in x direction.

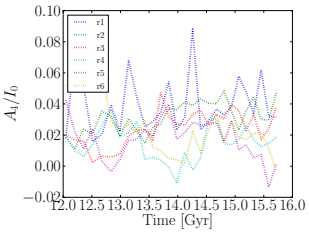

(e) Analysis of the A_4/I_0 parameter as a function of time for different radii in y direction.

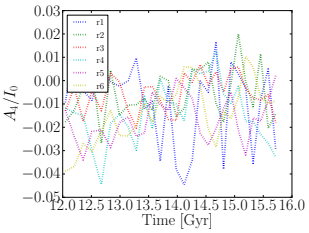

(f) Analysis of the A_4/I_0 parameter as a function of time for different radii in z direction.

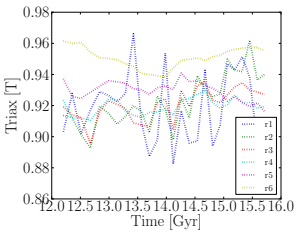

(g) Analysis of the triaxiality parameter as a function of time for different radii.

Figure 6.10.: Analysis of the dark matter from the simulation with a 15% gas fraction and the two rotation vectors pointing in the opposite direction.

Looking at the density map of the stellar particles (6.11a, 6.11b, and 6.11c) one generally does not expect the galaxy to have high negative A_4/I_0 parameter values. This assumption is confirmed when looking at the A_4/I_0 parameter values as a function of the radius (6.3d, 6.3e, and 6.3f) as well as as a function of time for different radii (6.11g, 6.11h, and 6.11i). The A_4/I_0 parameter values for the los axis direction x and y as a function of the radius are scattered around zero whereas the negative values tend to arise at small radii. The scale of these fluctuations is, however, not high with a maximal amplitude of 0.015, and 0.03 for the los axis direction x and y, respectively. For the los axis direction z one can see that the A_4/I_0 parameter values lie in the low range negative side, with a range between -0.025 and 0.0. Looking at the trend from the analysis of the A_4/I_0 parameter as a function of time for different radii one can generally say that the values of the parameter fluctuate around zero with small deviations after the galaxy seems to have reached its relaxed state. Only in the los axis direction z are bigger fluctuations for the smallest radii ranging from -0.3 to 0.4 observed. The analysis of the A_4/I_0 parameter for different viewing angles is shown in figure 6.11j. One can see that the largest A_4/I_0 parameter value is 0.15 and can be observed at the second largest radii. The smallest parameter value is -0.1 and is observed at the largest radii. The larger radii therefore span the largest range of the possible A_4/I_0 parameter values for a given radii.

The analysis of the dark matter particles are shown in figure 6.12. The plots of the dependence of the A_4/I_0 parameter on the radius (6.12d, 6.12e, and 6.12f) show that the parameter values generally lie close to zero, whereas a few spikes for smaller times can also be observed. They however are less frequent when the galaxy seems to be in a relaxed state. The triaxiality analysis shown in figure 6.12g shows a similar picture where the triaxial parameter seems to converge to 0.9 with increasingly smaller fluctuations at later times. The dark matter system is therefore observed to be prolate.

Looking at the stellar density distribution in figures 6.11a, 6.11b, and 6.11c and taking into account the analysis above, one can say that this merger remnant from two galaxies with a gas fraction of 20% and and rotation vectors pointing into the same direction is not boxy.

6.2.6. merger_s2_fgas20

The simulations presented in this section have been carried out with a gas fraction of 20% and the two rotation vectors pointing opposite to each other. The analysis of the stellar distribution of the merger remnants is shown in figure 6.13. Looking at the stellar density map (6.13a, 6.13b, and 6.13c) one can already assume that this galaxy is not boxy. The different star formation sites which can also be spotted in figure 6.13c give rise to the expectation that at those positions the boxiness parameter might become negative. These assumptions are indeed confirmed when looking at the A_4/I_0 parameter as a function of the radii for a given output. Looking at the A_4/I_0 parameter as a function of time (6.13g and 6.13h) for different radii one can see that for the los axis directions x and y the galaxy system merges towards a parameter value of zero with increasingly smaller fluctuations of the parameter. The fluctuations of the A_4/I_0 parameters for the los axis direction z are larger, ranging from -0.2 to 0.1, and

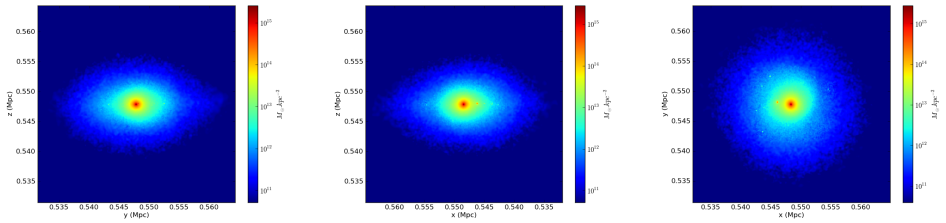

(a) Density map of the stars with los axis in x direction.

(b) Density map of the stars with los axis in y direction.

(c) Density map of the stars with los axis in z direction.

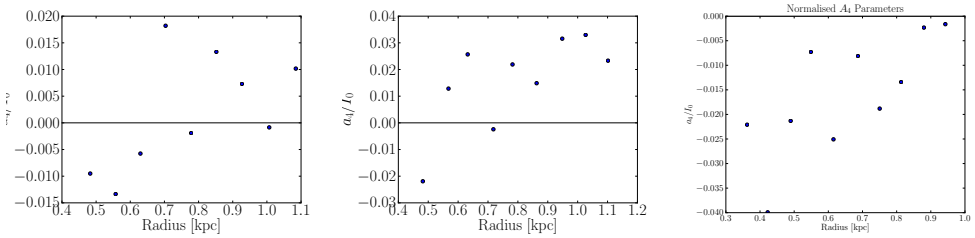

(d) Analysis of the A_4/I_0 parameter as a function of radius for the los axis x direction.

(e) Analysis of the A_4/I_0 parameter as a function of radius for the los axis y direction.

(f) Analysis of the A_4/I_0 parameter as a function of radius for the los axis z direction.

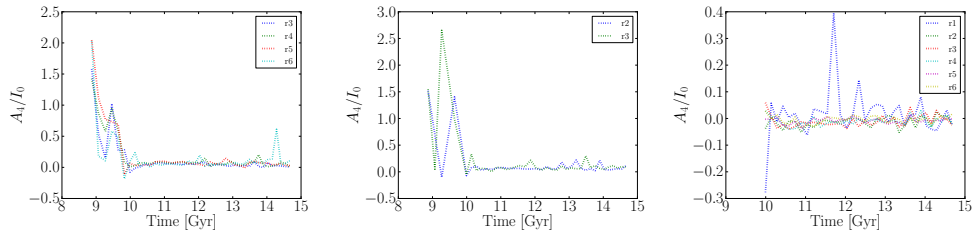

(g) Analysis of the A_4/I_0 parameter as a function of time for different radii in x direction.

(h) Analysis of the A_4/I_0 parameter as a function of time for different radii in y direction.

(i) Analysis of the A_4/I_0 parameter as a function of time for different radii in z direction.

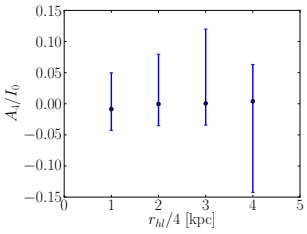

(j) Analysis of the A_4/I_0 parameter as a function of the different viewing angle and the radii.

Figure 6.11.: Analysis of the stars from the simulation with a 20% gas fraction and the two rotation vectors pointing in the same direction.

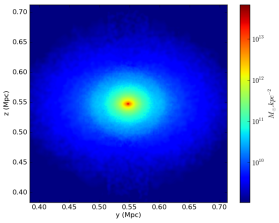

(a) Density map of the dark matter praticles with los axis in x direction.

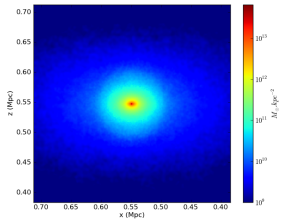

(b) Density map of the dark matter praticles with los axis in y direction.

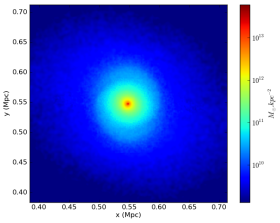

(c) Density map of the dark matter praticles with los axis in z direction.

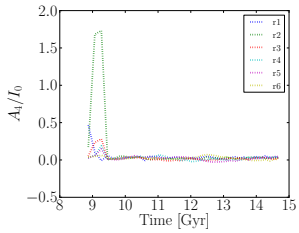

(d) Analysis of the A_4/I_0 parameter as a function of time for different radii in x direction.

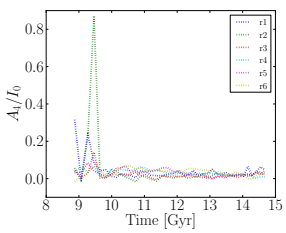

(e) Analysis of the A_4/I_0 parameter as a function of time for different radii in y direction.

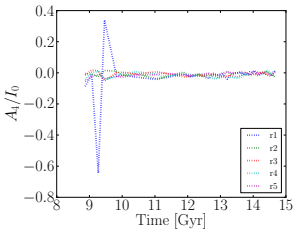

(f) Analysis of the A_4/I_0 parameter as a function of time for different radii in z direction.

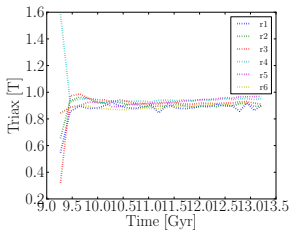

(g) Analysis of the triaxiality parameter as a function of time for different radii.

Figure 6.12.: Analysis of the dark matter from the simulation with a 20% gas fraction and the two rotation vectors pointing in the same direction.

no obvious trend can be noted. The analysis of the A_4/I_0 parameter as a function of the different viewing angles (6.13j) reveals the change in the parameter is the largest for large radii ranging from -0.2 to 0.2.

Looking at the analysis of the A_4/I_0 parameter for the dark matter particles as a function of time one cannot observe any obvious trend. It can, however, be noted that for the los axis orientation x and y the parameter values are generally above zero, whereas for the los axis orientation z the parameter values are mostly below zero. Looking at the triaxiality analysis as a function of time in figure 6.14g one can see that the small radii has the smallest triaxiality (mean value of 0.91) whereas the largest radii has the largest triaxiality (mean value of 0.97). The dark matter distribution is therefore prolate.

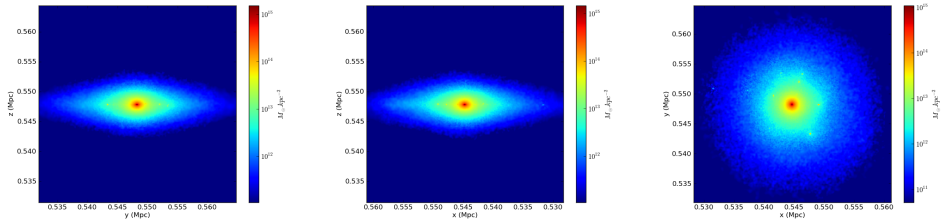

(a) Density map of the stars with los axis in x direction.

(b) Density map of the stars with los axis in y direction.

(c) Density map of the stars with los axis in z direction.

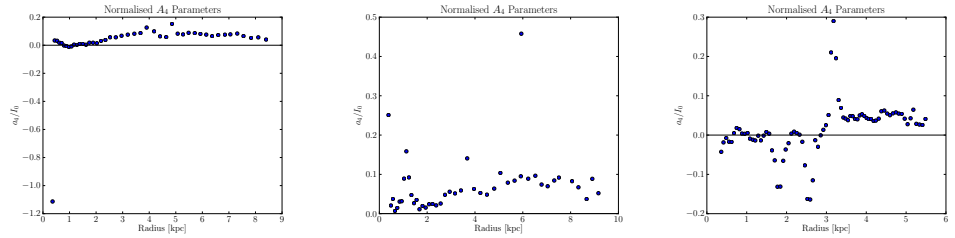

(d) Analysis of the A_4/I_0 parameter as a function of radius for the los axis x direction.

(e) Analysis of the A_4/I_0 parameter as a function of radius for the los axis y direction.

(f) Analysis of the A_4/I_0 parameter as a function of radius for the los axis z direction.

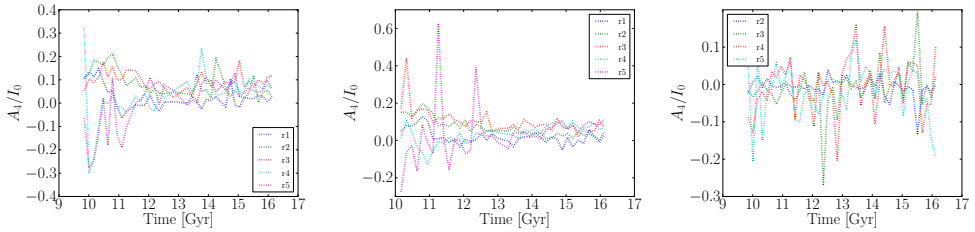

(g) Analysis of the A_4/I_0 parameter as a function of time for different radii in x direction.

(h) Analysis of the A_4/I_0 parameter as a function of time for different radii in y direction.

(i) Analysis of the A_4/I_0 parameter as a function of time for different radii in z direction.

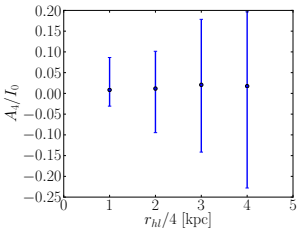

(j) Analysis of the A_4/I_0 parameter as a function of the different viewing angle and the radii.

Figure 6.13.: Analysis of the stars from the simulation with a 20% gas fraction and the two rotation vectors pointing in the opposite direction.

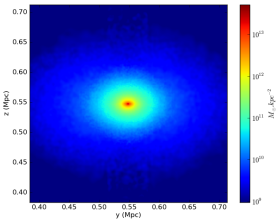

(a) Density map of the dark matter praticles with los axis in x direction.

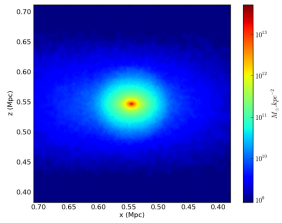

(b) Density map of the dark matter praticles with los axis in y direction.

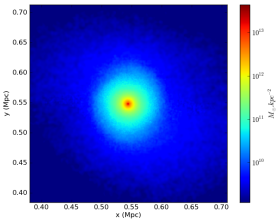

(c) Density map of the dark matter praticles with los axis in z direction.

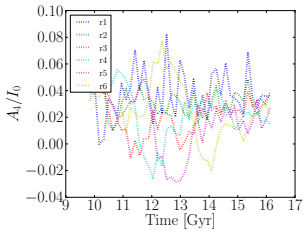

(d) Analysis of the A_4/I_0 parameter as a function of time for different radii in x direction.

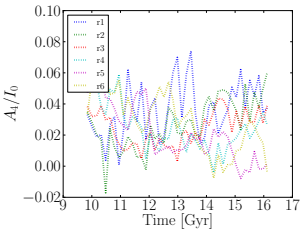

(e) Analysis of the A_4/I_0 parameter as a function of time for different radii in y direction.

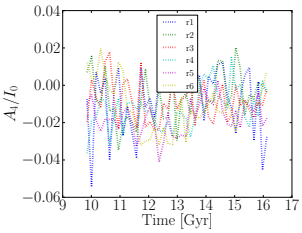

(f) Analysis of the A_4/I_0 parameter as a function of time for different radii in z direction.

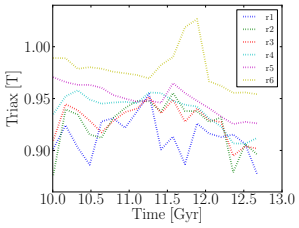

(g) Analysis of the triaxiality parameter as a function of time for different radii.

Figure 6.14.: Analysis of the dark matter from the simulation with a 20% gas fraction and the two rotation vectors pointing in the opposite direction.

6.3. Gaseous Feedback Run

Mergers are believed to advance the accumulation of cold gas into the center of a merger remnant resulting in an increase in the star formation rate (SFR). A fraction of newly formed stars is short-lived and these stars explode in supernovae which again feed heat back into the surrounding gas. This can in turn again result in the reducing the efficiency of star formation and in some cases blow gas out of the galaxy in a galactic wind. These supernovae-driven winds are thought to suppress the formation of low-gas galaxies. Another potential source of feedback is provided by the accretion of gas onto a supermassive black hole in the center of the galaxy, called an active galactic nucleus (AGN). In all the simulations presented above such feedback mechanism have been neglected. In order to analyse the effect of feedback mechanisms on merger remnants with regard of their boxiness two simulations with a gas fraction of 10% have been performed with the angular momentum vector pointing in the same and opposite direction. The used feedback mechanism is described in Dubois & Teyssier (2008b) where the effect of AGN's has been neglected for the simulations presented here. Additionally, two other simulations have been performed by cutting out a box of the final output from the feedback simulation, rotating, translating, and duplicating the galaxy to again merge them together with an equal orientation of the rotation axes as well as an opposite rotation of the two axes.

6.3.1. merger_s1_fgas10_fb

The stellar analysis of the feedback simulations with a gas fraction of 10% and the two rotation vectors pointing in the same direction can be seen in figure 6.15. Looking at the density map of the stars (6.20a, 6.20b) one can already assume that the A_4/I_0 parameter values are below zero for the outer part of the galaxy. This is confirmed by the analysis of the A_4/I_0 parameter seen in the plots (6.20d, 6.20e, 6.20f). For the los axis directions x and y one can see that the A_4/I_0 parameter reaches from positive values at small radii to negative values at larger radii. This is very promising as the positive parameter values suggest that the inner region hosts a discy inner part where the outer region is clearly boxy. The A_4/I_0 parameters for the los axis direction z are only zero ranging from -0.1 to 0.0. Looking at the A_4/I_0 parameter as a function of time for different radii one can observe that the parameter values are lowest for large radii and highest for small radii for the los axis directions x and y (6.15g, and 6.15h). At large radii the values range from -0.13 to 0.05, and -0.13 to 0.15 for the los axis directions x and y, respectively. At small radii the values range from 0.1 to 0.1 for the los axis direction x and from 0.1 to 0.2 for the los axis direction y. These ranges also indicate the disk like structure in the inner region of the galaxy as the A_4/I_0 parameter never reaches negative values for small radii. At large radii however the parameter values are mostly negative. The fluctuations of the A_4/I_0 parameters also decrease with increasing time in correspondence with when the galaxy reaches a stable configuration. This indicates that although the galaxy seems to be boxy it is still stable for a few Gyr. The analysis of the A_4/I_0 parameter for the los axis direction can also be seen in plot 6.15i. For this los it is harder to distinguish a trend. The

parameter value ranges from -0.11 to 2.5 whereas the fluctuations also seem to decrease with increasing time. The A_4/I_0 parameter value as a function of the different viewing angles also reveals that the mean value for all the different radii is close to zero. There are however huge fluctuations for parameter values to be below zero. For instance, the minimum value of the A_4/I_0 parameter when looking from different angles is -1.1. This motivated further analysis of this galaxy further. In figure 6.17 the analysis of the viewing angle where the most negative parameter for the largest radii was observed is shown[1]. In plot 6.17c one can see that for this galaxy the A_4/I_0 parameter goes from positive values at large radii to small values at large radii. The minimum value of the parameter is comparable with the minimum boxiness parameter of LEDA 074886.

The analysis of the dark matter distribution is shown in figure 6.16 where the parameter A_4/I_0 is shown as a function of time for different radii in the plots 6.16d, 6.16e, and 6.16f. It is hard to see a trend for all the different los axis directions. The A_4/I_0 parameters range from -0.02 to 0.08, -0.02 to 0.06, and -0.05 to 0.02 for the los axis directions x, y, and z, respectively. Looking at the triaxiality as a function of time one can generally see that the triaxiality of the galaxy is lower at early times and higher at later times for small radii. The triaxiality of the inner part of the galaxy is rising from the lowest value of 0.84 at the beginning to the highest value of 0.98 in the middle and falling again onto a mean value of 0.9. Similar behavior can be seen for the second and third smallest radii. The triaxiality of the outer parts of the galaxy is however more stable compared with the inner part.

We can conclude that a possible scenario for the formation of LEDA 074886 is by merging two galaxies with a low gas fraction of around 10% and the two rotation angles pointing into the same direction. It can be assumed that it is important that the simulations are done with a feedback mechanism. The slightly triaxial halo of the galaxy at the beginning of the formation can be understood to support the building of a boxy galaxy, whereas the prolate halo in the middle phase might be responsible for the stability of the galaxy. Further analysis to test this hypothesis in more detail would have to be carried out.

6.3.2. merger_s2_fgas10_fb

The analysis of the stellar distribution for the feedback run with a gas fraction of 10% and rotating vectors pointing in the opposite direction is shown in figure 6.18. Looking at the density maps of the stars (6.18a, 6.18b, and 6.18c) one can see that this galaxy is highly unlikely to show any sign of boxiness. It also seems that this galaxy is unstable (also when looking at density maps at earlier times). The analysis of the A_4/I_0 parameter as a function of the radius at a given output reveals that the nonboxiness of the merger remnant as the majority of the calculated parameter values are above zero (6.18d, 6.18e, and 6.18f). The analysis of the A_4/I_0 parameter as a function of time for different radii (6.18g, 6.18h, and 6.18i) shows that the boxiness is for the majority of the time above zero for the los axis orientations x and y. There are, however, a

[1] It is important to note that the gas distribution is slightly tilted in the x-y axis from our line-of-sight axis z for reasons still unknown.

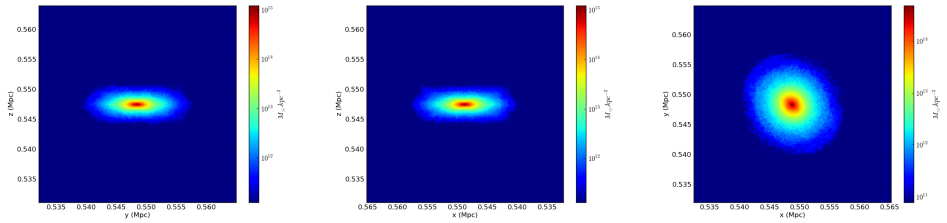

(a) Density map of the stars with los axis in x direction.

(b) Density map of the stars with los axis in y direction.

(c) Density map of the stars with los axis in z direction.

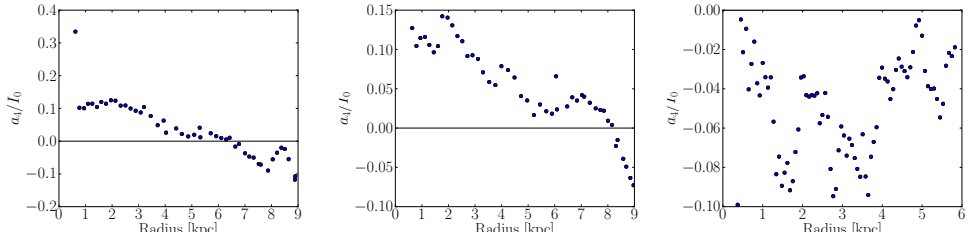

(d) Analysis of the A_4/I_0 parameter as a function of radius for the los axis in x direction.

(e) Analysis of the A_4/I_0 parameter as a function of radius for the los axis in y direction.

(f) Analysis of the A_4/I_0 parameter as a function of radius for the los axis in z direction.

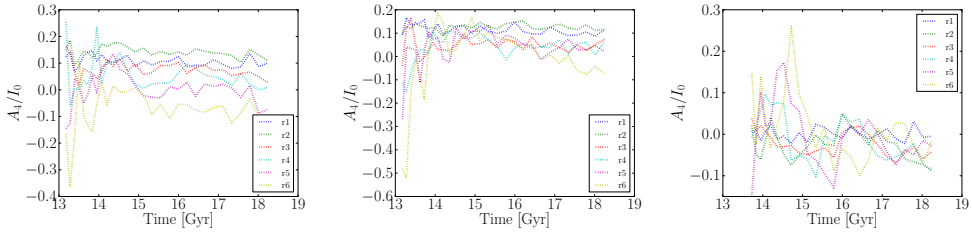

(g) Analysis of the A_4/I_0 parameter as a function of time for different radii in x direction.

(h) Analysis of the A_4/I_0 parameter as a function of time for different radii in y direction.

(i) Analysis of the A_4/I_0 parameter as a function of time for different radii in z direction.

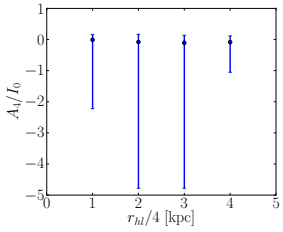

(j) Analysis of the A_4/I_0 parameter as a function of the different viewing angle and the radii.

Figure 6.15.: Analysis of the stars from the feedback simulation with a 10% gas fraction and the two rotation vectors pointing in the same direction.

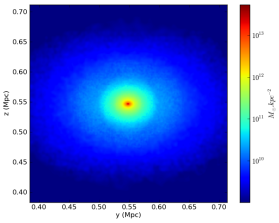

(a) Density map of the dark matter praticles with los axis in x direction.

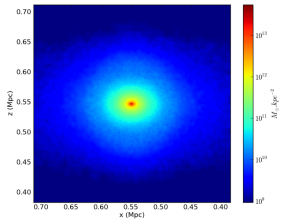

(b) Density map of the dark matter praticles with los axis in y direction.

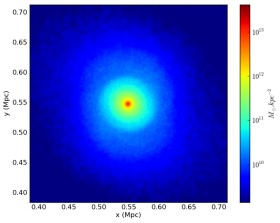

(c) Density map of the dark matter praticles with los axis in z direction.

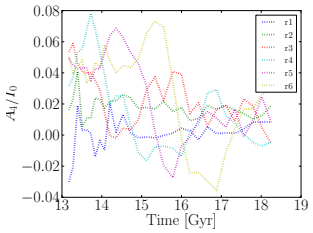

(d) Analysis of the A_4/I_0 parameter as a function of time for different radii in x direction.

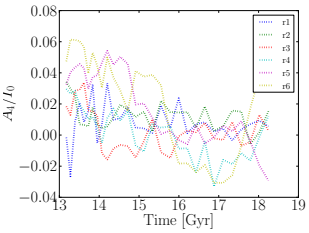

(e) Analysis of the A_4/I_0 parameter as a function of time for different radii in y direction.

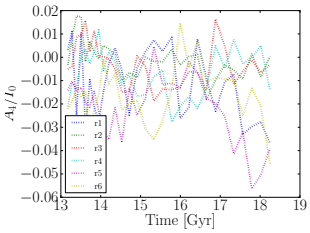

(f) Analysis of the A_4/I_0 parameter as a function of time for different radii in z direction.

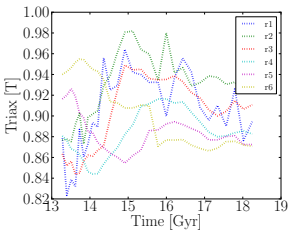

(g) Analysis of the triaxiality parameter as a function of time for different radii.

Figure 6.16.: Analysis of the dark matter from the feedback simulation with a 10% gas fraction and the two rotation vectors pointing in the same direction.

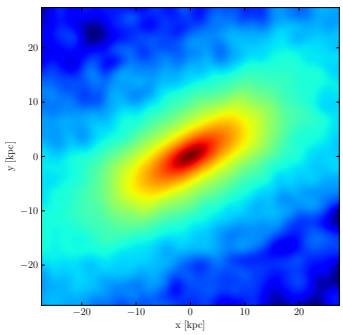

(a) Density map of the stars with los in the direction of the most boxiness value.

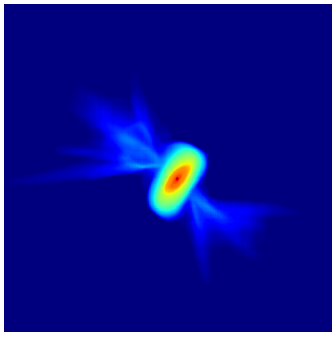

(b) Density map of the gas with los in the direction of the most boxiness value.

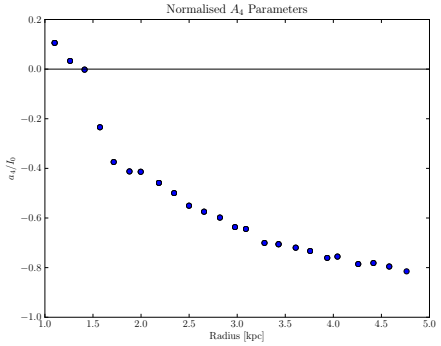

(c) Analysis of the A_4/I_0 parameter as a function of radius for the los in the direction of the most boxiness value.

Figure 6.17.: Analysis of the star and gas distribution from the feedback simulation with a 10% gas fraction and the two rotation vectors pointing in the same direction.

few spikes that needed to be analysed in further detail for these los axis orientations. When looking at the evolution of the parameter for the los axis orientation z one can see that the A_4/I_0 parameter values are going down twice to -0.25. Because of these observations above the boxiness parameter of the different los axis directions x, y, and z was analysed for the output with the corresponding lowest A_4/I_0 parameter observed. The parameters obtained in this way where however extremely noisy making it impossible to analyse properly. This supports the assumption of the galaxy is still not in a relaxed state. From this analysis it can however be noted that if the galaxy has shown a low A_4/I_0 parameter value it was mostly at low radii. In either direction a discy inner region was not detected making it very unlikely to provide a possible explanation for the formation of LEDA 074886.

The analysis of the A_4/I_0 parameter with time for the dark matter distribution (6.19d, 6.19e, and 6.19f) is again hard to interpret. It can be noted that the A_4/I_0 parameter values for the los axis directions x, and x are generally above zero whereas for the los axis direction z the values fluctuate around -0.01. The amplitude of the fluctuation are 0.04, 0.05, and 0.02 for the los axis directions x, y, and z, respectively. The triaxiality of the dark matter distribution does not fluctuate much and is around 0.94 indicating a prolate halo for this galaxy.

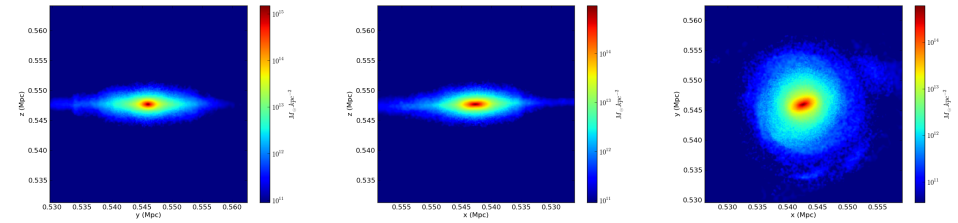

(a) Density map of the stars with los axis in x direction.

(b) Density map of the stars with los axis in y direction.

(c) Density map of the stars with los axis in z direction.

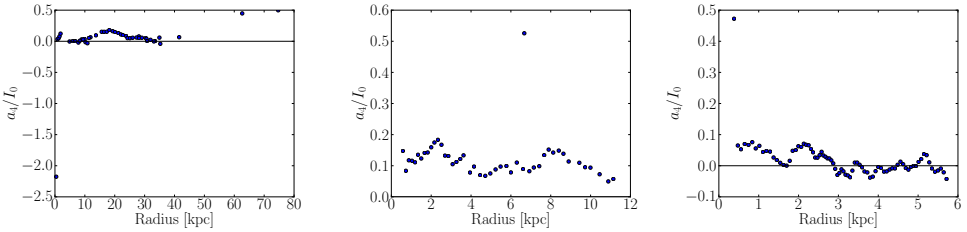

(d) Analysis of the A_4/I_0 parameter as a function of radius for the los axis in x direction.

(e) Analysis of the A_4/I_0 parameter as a function of radius for the los axis in y direction.

(f) Analysis of the A_4/I_0 parameter as a function of radius for the los axis in z direction.

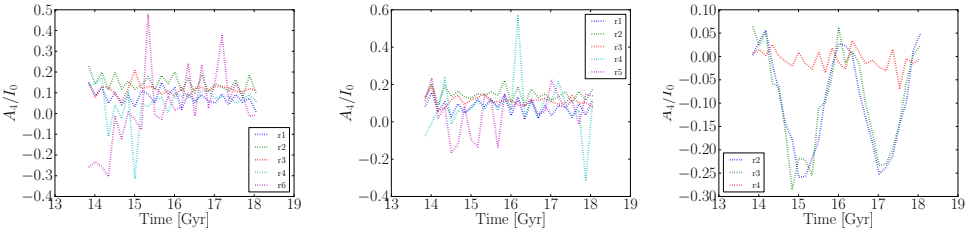

(g) Analysis of the A_4/I_0 parameter as a function of time for different radii in x direction.

(h) Analysis of the A_4/I_0 parameter as a function of time for different radii in y direction.

(i) Analysis of the A_4/I_0 parameter as a function of time for different radii in z direction.

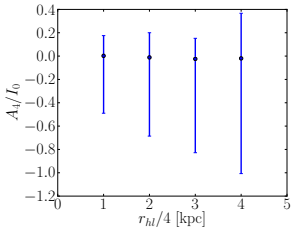

(j) Analysis of the A_4/I_0 parameter as a function of the different viewing angle and the radii.

Figure 6.18.: Analysis of the stars from the feedback simulation with a 10% gas fraction and the two rotation vectors pointing in the opposite direction.

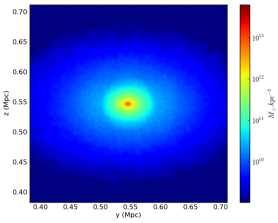

(a) Density map of the dark matter praticles with los axis in x direction.

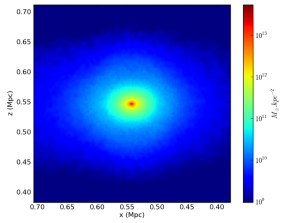

(b) Density map of the dark matter praticles with los axis in y direction.

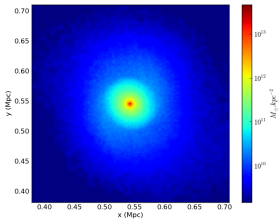

(c) Density map of the dark matter praticles with los axis in z direction.

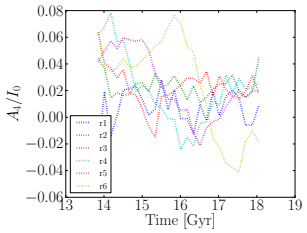

(d) Analysis of the A_4/I_0 parameter as a function of time for different radii in x direction.

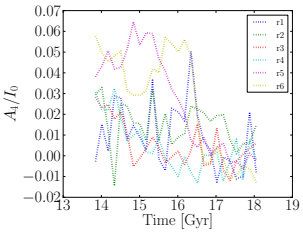

(e) Analysis of the A_4/I_0 parameter as a function of time for different radii in y direction.

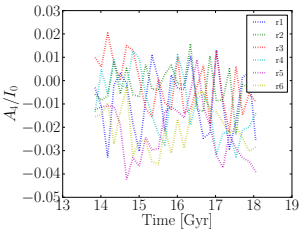

(f) Analysis of the A_4/I_0 parameter as a function of time for different radii in z direction.

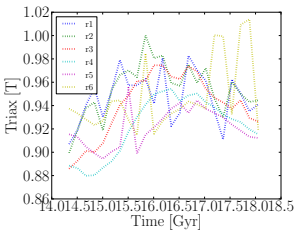

(g) Analysis of the triaxiality parameter as a function of time for different radii.

Figure 6.19.: Analysis of the dark matter from the feedback simulation with a 10% gas fraction and the two rotation vectors pointing in the same direction.

6.4. Restart simulations with cut out box and feedback

6.4.1. merger_s1_box_fb

The density map of the star distribution of the merger remnant of the restart run indicates a very elliptical galaxy (6.18a, 6.18b, and 6.18c). The analysis of the A_4/I_0 parameter as a function of the radius as well as the analysis of the A_4/I_0 parameter as a function of time at different radii supports this assumption. The parameter does not reach negative values for los axis directions x and y (6.18d, 6.18g, and 6.18e, 6.18h). For the los axis direction z (6.18f) negative values can be observed with a minimum A_4/I_0 parameter of -0.04 for the inner most radius of the galaxy when looking at the analysis of the A_4/I_0 parameter as a function of time. The analysis of the A_4/I_0 parameter as a function of the viewing angle reveals once more that the los axis does not necessarily give rise to the most extreme A_4/I_0 value. One can see that the range of the parameter can be from -0.3 to 0.1 in the most extreme case. The different ranges for the different radii are however similar in range and do not differ significantly.

The dark matter distribution analysis can be seen in figure 6.21. The A_4/I_0 parameter of the los axis direction x is observed to be lowest for the middle of the galaxy and higher for the outer as well as the inner part of the galaxy. Looking at the A_4/I_0 parameter of the los axis direction y no general trend can be observed whereas the A_4/I_0 parameter for the los z is observed to be lowest for larger radii than smaller radii. Generally the different values span a range of 0.1, 0.1, and 0.8 for the los axis direction x, y, and z, respectively. The triaxiality of the halo as a function of time is observed to be stable with one spike from the middle of the galaxy ranging from 0.9 to 1.1.

Because of the elliptically of the dark matter distribution as well as the stellar distribution and the other analysis made above it seems to be unlikely that a merging of two merger remnants with an inclination angle of 15° provides a possible solution for the formation of LEDA 074886.

6.4.2. merger_s2_box_fb

The analysis of the stellar distribution of the merger simulation of two merger remnants merged with an inclination angle of 15° is shown in figure 6.22. Looking at the density distribution of the stars (6.22a, 6.22b, and 6.22c) the galaxy looks very much elliptical. The analysis of the A_4/I_0 parameter as a function of the radius (6.22d, 6.22e, and 6.22f) supports this picture specially for the los axis directions x and y where the parameter values are all above zero. The same picture for those los axis direction arises when looking at the evolution of the A_4/I_0 parameter with time (6.22g, and 6.22h) where one can see that the parameter values never reach below zero. For the los axis direction x the A_4/I_0 parameter as a function of radius fluctuates around zero, similar to the analysis of the A_4/I_0 parameter as a function of time where the fluctuations are again around zero more often being on the positive side. The analysis of the ranges of the A_4/I_0 parameter as a function of the viewing angle reveals a similar picture where it can be seen that the most negative number found is -0.1.

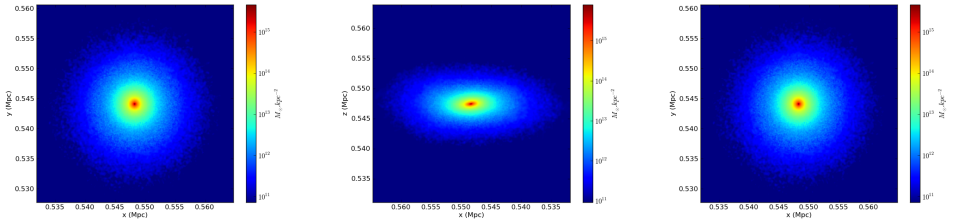

(a) (b) (c)

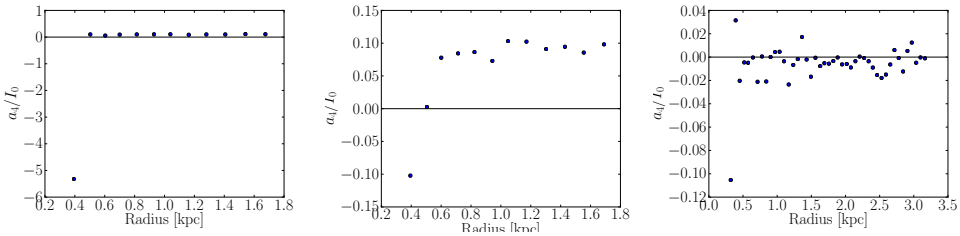

(d) Analysis of the A_4/I_0 parameter as a function of radius for the los axis in x direction.

(e) Analysis of the A_4/I_0 parameter as a function of radius for the los axis in y direction.

(f) Analysis of the A_4/I_0 parameter as a function of radius for the los axis in z direction.

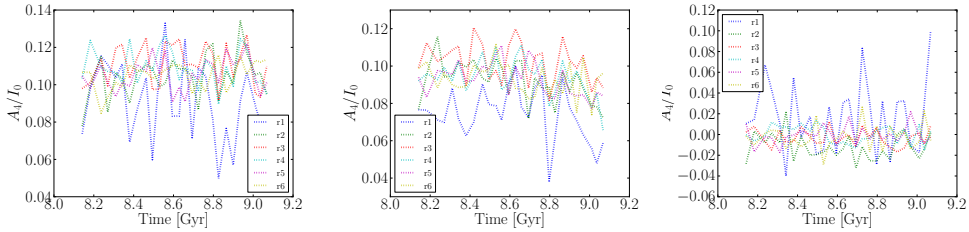

(g) Analysis of the A_4/I_0 parameter as a function of time for different radii in x direction.

(h) Analysis of the A_4/I_0 parameter as a function of time for different radii in y direction.

(i) Analysis of the A_4/I_0 parameter as a function of time for different radii in z direction.

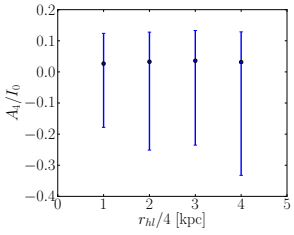

(j) Analysis of the A_4/I_0 parameter as a function of the different viewing angle and the radii.

Figure 6.20.: Analysis of the stars from the restart simulation of a rotated, translated and duplicated cut out box. Simulations were done with a 10% gas fraction, feedback and the two rotation vectors pointing in the same direction.

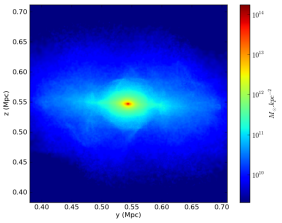

(a) Density map of the dark matter praticles with los axis in x direction.

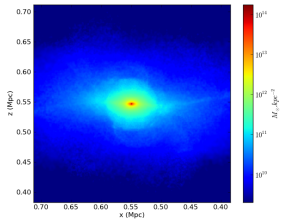

(b) Density map of the dark matter praticles with los axis in y direction.

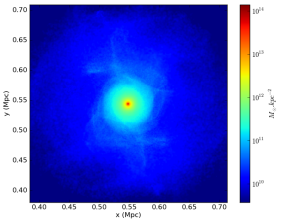

(c) Density map of the dark matter praticles with los axis in z direction.

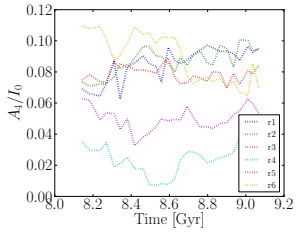

(d) Analysis of the A_4/I_0 parameter as a function of time for different radii in x direction.

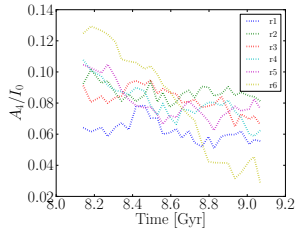

(e) Analysis of the A_4/I_0 parameter as a function of time for different radii in y direction.

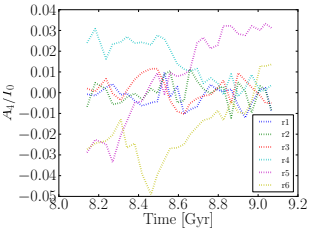

(f) Analysis of the A_4/I_0 parameter as a function of time for different radii in z direction.

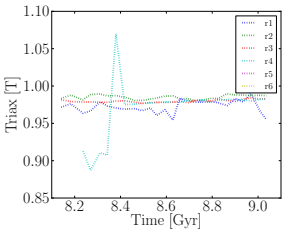

(g) Analysis of the triaxiality parameter as a function of time for different radii.

Figure 6.21.: Analysis of the dark matter from the restart simulation of a rotated, translated and duplicated cut out box. Simulations were done with a 10% gas fraction, feedback and the two rotation vectors pointing in the same direction.

The A_4/I_0 parameter as a function of radius for the dark matter distribution also never reaches negative values for the los axis directions x and y. It is also mostly positive for the los axis direction z. Looking at the triaxiality as a function of time and taking the absolute value of the triaxiality one can see that whereas the inner part is prolate the outer part is triaxial. Note that although the outer part of the dark matter distribution is triaxial this did not lead to a boxy outer region in the stellar distribution.

From the stellar analysis described above we can assume that the possibility that two merger remnants with a rotation angle pointing at opposite directions merging with an inclination angle of 15° is unlikely to have lead to the formation of LEDA 074886.

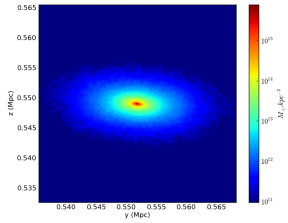

(a) Density map of the stars with los axis in x direction.

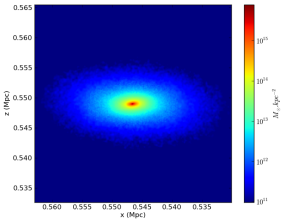

(b) Density map of the stars with los axis in y direction.

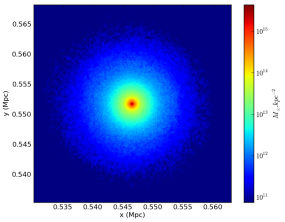

(c) Density map of the stars with los axis in z direction.

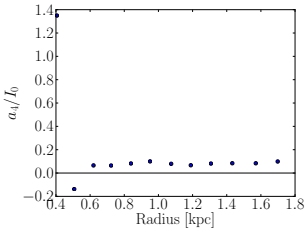

(d) Analysis of the A_4/I_0 parameter as a function of radius for the los axis in x direction.

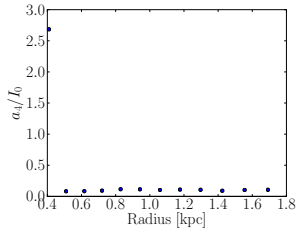

(e) Analysis of the A_4/I_0 parameter as a function of radius for the los axis in y direction.

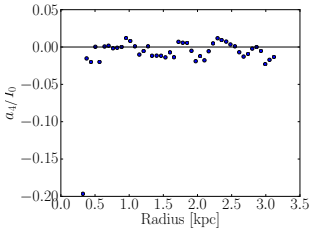

(f) Analysis of the A_4/I_0 parameter as a function of radius for the los axis in z direction.

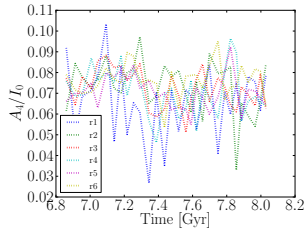

(g) Analysis of the A_4/I_0 parameter as a function of time for different radii in x direction.

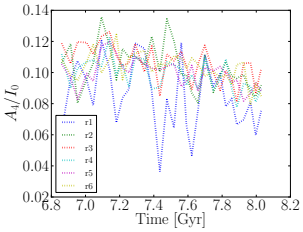

(h) Analysis of the A_4/I_0 parameter as a function of time for different radii in y direction.

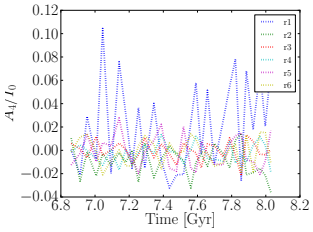

(i) Analysis of the A_4/I_0 parameter as a function of time for different radii in z direction.

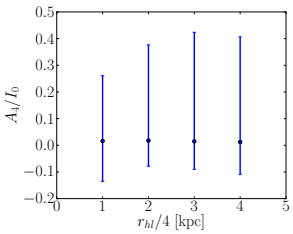

(j) Analysis of the A_4/I_0 parameter as a function of the different viewing angle and the radii.

Figure 6.22.: Analysis of the stars from the restart simulation of a rotated, translated and duplicated cut out box. Simulations were done with a 10% gas fraction, feedback and the two rotation vectors pointing in the opposite direction.

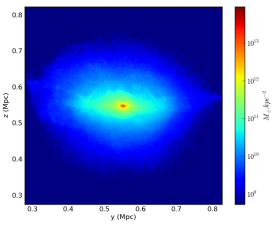

(a) Density map of the dark matter praticles with los axis in x direction.

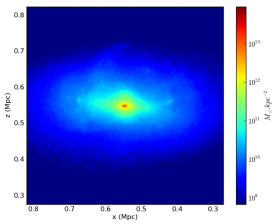

(b) Density map of the dark matter praticles with los axis in y direction.

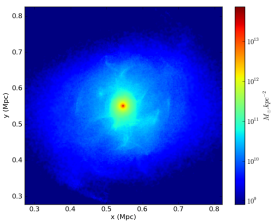

(c) Density map of the dark matter praticles with los axis in z direction.

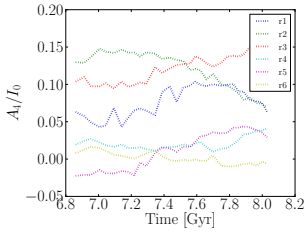

(d) Analysis of the A_4/I_0 parameter as a function of time for different radii in x direction.

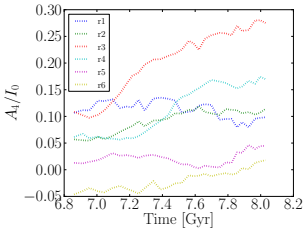

(e) Analysis of the A_4/I_0 parameter as a function of time for different radii in y direction.

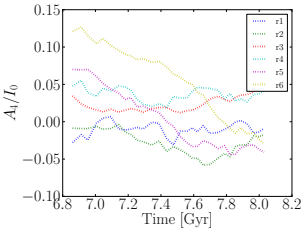

(f) Analysis of the A_4/I_0 parameter as a function of time for different radii in z direction.

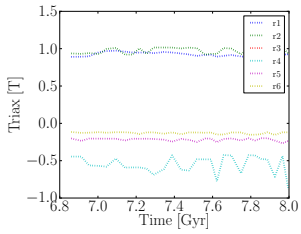

(g) Analysis of the triaxiality parameter as a function of time for different radii.

Figure 6.23.: Analysis of the dark matter from the restart simulation of a rotated, translated and duplicated cut out box. Simulations were done with a 10% gas fraction, feedback and the two rotation vectors pointing in the opposite direction.

7. Code

Within this thesis two main program projects have been developed. The first project BELLE (**B**oxy **ELL**ipse **E**xtraction), written in Python, is a collection of smaller programmes which analyse the boxiness of the galaxy. The main program is similar to the task ELLIPSE in IRAF. In addition, the evolution of the boxiness of the galaxy, triaxiality over time, and/or rotation angle of the line-of-sight axis can be studied.

The second project involved writing a new patch to generate initial conditions for RAMSES simulations. It includes two patch subroutines for RAMSES. The new initial conditions are generated by cutting out a cube of a given RAMSES output. If desired, the cut out box can be duplicated, translated and rotated.

7.1. BELLE

The program BELLE (Boxy ELLipse Exraction) approximates the isophotes and analyses the boxiness of a galaxy. It fits the isophotes using the Fourier series:

$$I(\theta) = I_0 + \sum_{n=1}^{\infty} (A_n \cos n\theta + B_n \sin n\theta) \tag{7.1}$$

where θ is the azimuthal angle and I_0 the average intensity over the ellipse. The A_4 coefficient to the $\cos 4\theta$ Fourier component is used to quantifying the isophotal deviation from an ellipse and therefore gives a parameter to analyse the boxiness of the galaxy. If the A_4 parameter is positive (negative) the isophotes are said to be discy (boxy). In figure 7.1, an example of a negative A_4 parameter is shown in comparison with a positive parameter. One has to be careful, however, as the ratio between the other parameters A_i where $i \in [1, 2, 3, 5, ..]$ as well as B_j with $j \in [1, n]$ also depends the shape of the isophotes.

BELLE is flexible in how it processes a map of a galaxy. Depending on the data to process, one can choose between reading a general RAMSES output, FITS[1] files, or a test-case galaxy made with genMap.py. In each case, the settings in the makeContours.py program have to be changed accordingly.

- To read a **RAMSES output**, a generated map, directory, half-light-radius, as well as the line-of-sight have to be given as an input. The map as well as the profile can, for example, be generated with the Pymses package or with the fortran routine within RAMSES. The program can then be started with

[1] For further Informations about the FITS Data Format read for example `http://fits.gsfc.nasa.gov/fits_primer.html`.

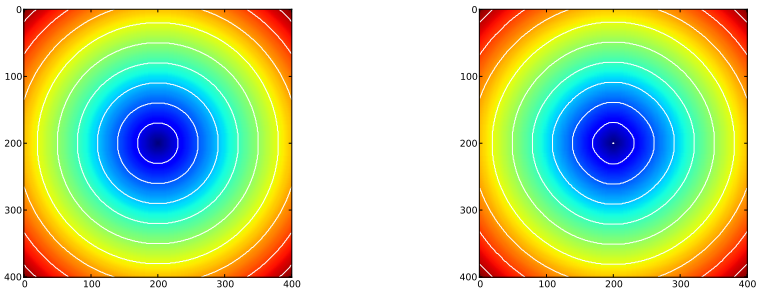

(a) Test map of with a positive A_4 parameter. $A_1 = 0.1$, $A_2 = 0.1$, $A_3 = 0.1$, $A_4 = 10$, $A_5 = 0.1$, $B_1 = 0.1$, $B_2 = 0.1$, $B_3 = 0.1$, $B_4 = 0.1$, $B_5 = 0.1$]

(b) Test map of with a negative A_4 parameter. $A_1 = 0.1$, $A_2 = 0.1$, $A_3 = 0.1$, $A_4 = -100$, $A_5 = 0.1$, $B_1 = 0.1$, $B_2 = 0.1$, $B_3 = 0.1$, $B_4 = 0.1$, $B_5 = 0.1$

Figure 7.1.: Comparison between a positive and negative A_4 parameter. It can be seen that a negative A_4 parameter can lead to boxy isophotes whereas a positive A_4 parameter can lead to discy (round) isophotes.

```
python ~/PythonProgrammes/BELLE/makeContours.py $map $dir $r_hl
    $los
```

The half-light radius is needed to calculate the maximum and minimum radius for which the isophotes should be analysed. To be able to compare the experimental results with the simulated results the maximum (minimum) radius $r_{\max}$ ($r_{\min}$) is calculated as

$$r_{\max} = r_{\max\_p} * f_{\mathrm{hl}} \qquad r_{\min} = r_{\min\_p} * f_{\mathrm{hl}} \tag{7.2}$$

where $r_{\max\_p}$ ($r_{\min\_p}$) is the maximum (minimum) radius given in the paper used to analyse the isophotes and f_{hl} is the ratio between the half-light-radius of the observational results given in the paper and the half-light-radius of the simulated galaxy. The half-light-radius has to be calculated from the cumulative mass-profile of the galaxy where the half-light-radius is defined to be the radius containing half of the mass of the cumulative profile.

- To generate and analyse a **test map** the program can be run for a given number of Fourier parameters a_n, b_n with the command

```
python ~/PythonProgrammes/BELLE/makeContours.py $n $a_1 $a_2 $a_3
    $a_4 $a_5 ... $a_n $b_1 $b_2 $b_3 $b_4 $b_5 ...
```

where n is the number of parameters in this case. MAKECONTOURS.PY calls the program GENMAP.PY which outputs a matrix that represents a galaxy with a known luminosity distribution and a known boxiness. It can be used to test the program BELLE as well as combinations of Fourier parameters.

- To read the **FITS files** the python library PYFITS has been used. It can, amongst other things, read the primary array of a FITS file and convert the data into a python array that can further be processed. To analyse the boxiness of the observational galaxy the program can be run with the command

```
python ~/PythonProgrammes/BELLE/makeContours.py i.fits
```

The general outline of the program BELLE is the following

```
* read data, call it A
* make sure there is no zero in A otherwise give it a small number
* take logarithm of A, call it C
* smooth C
* get the contours of C
* fit the contours with ellipses
* get real data (no logarithm data) of densities along the ellipse
* fit density data along ellipse with the Fourier expansion
* get A_4 parameter
* get semi major axis, major axis and other ellipse parameter data
```

In figure 7.2 an example of the fitting process is shown for a simulated map whereas in figure 7.3 an example is shown for the FITS map from a real galaxy. There are four possible outputs from the program shown in figure 7.4. The program MAKECONTOURS.PY generates a map of the boxiness versus radius as shown in plot (a). Another possibility is to plot the boxiness of the galaxy at different radii as a function of time made with the program MAKECONTOURSTIME.PY as shown in (b). The plots shown in (c) and (d) correspond to the boxiness as viewed from different angles. To uniformly sample line-of-sight vectors, points x, y, z are uniformly sampled over a sphere by choosing

$$\begin{aligned} x &= \sqrt{1-u^2}\cos\theta \\ y &= \sqrt{1-u^2}\sin\theta \\ z &= u \end{aligned} \tag{7.3}$$

with $\theta \in [0, 2\phi)$ and $u \in [-1, 1]$. Plot (c) shows the boxiness with respect to θ of six different u at one radius. Since this picture is hard to analyse, a fourth picture (d) was made. This picture shows the possible change of the boxiness as a function of the different radii. The errorbars are calculated as the maximum and minimum of the possible boxiness when varying θ and u. The results presented in this thesis will only show plot (d) because of easier readability. The program MAKETRIAX.PY calculates the triaxiality of the galaxy from projections along different axes. The triaxiality parameter is defined as

$$T = \frac{a^2 - b^2}{a^2 - c^2} \tag{7.4}$$

where a, b, and c are the major, semi-major, and minor axis of the galaxy. The usual technique to calculate the triaxiality is by diagonalising the inertia tensor, but since MAKECONTOURS.PY already calculated the major, and semi-major axis of the different ellipses at a given radius and line-of-sight axis, this information was used to calculate T. A typical output of MAKETRIAX.PY is shown in plot (e) of figure 7.5.

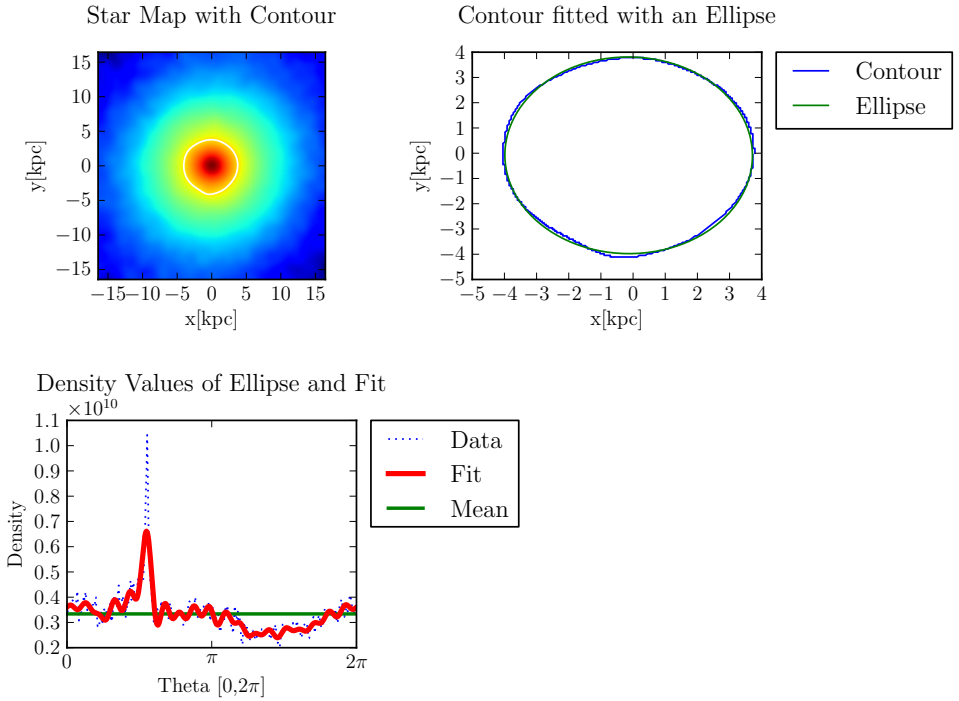

Figure 7.2.: Outline of the program BELLE. In the first picture a specific contour of the galaxy map is shown. In the second picture a fit of the contour with the ellipse is shown. In the third picture a fit of the density values along the ellipse is shown.

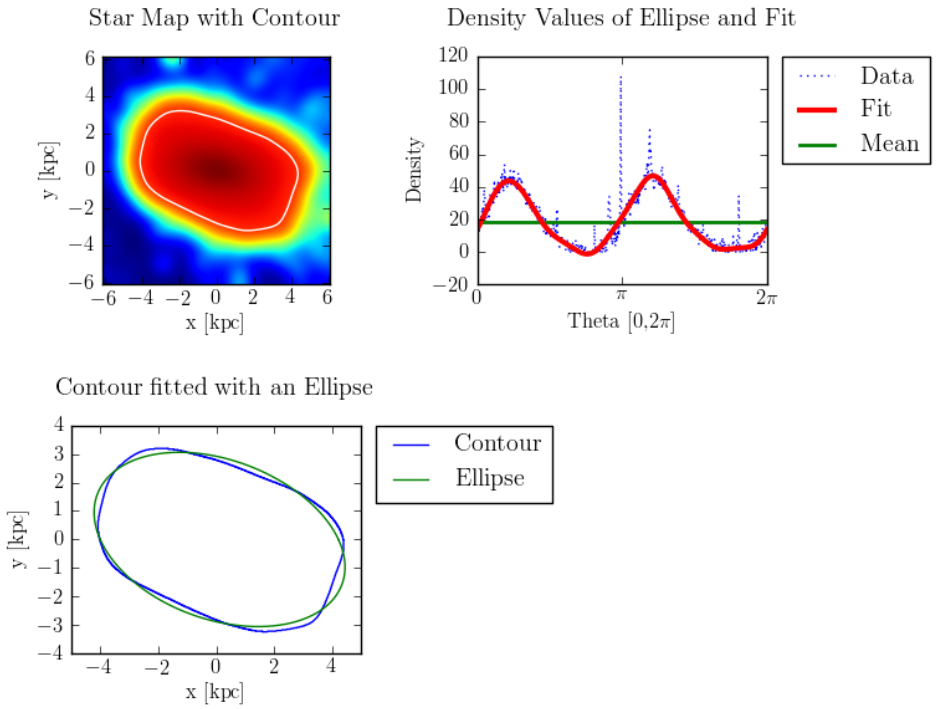

Figure 7.3.: Example plots from the program BELLE using a FITS file of a real galaxy. The upper-left picture shows a specific contour of LEDA. In the upper-right, a fit of the contour with the ellipse is shown. In the lower-left, a fit of the density values along the ellipse is shown.

7.2. Initial conditions

The new initial conditions subroutines is a patch that includes a new way to generate initial AMR conditions. The patch is designed to cut out a cube of a RAMSES output and then load it using the RAMSES starting routine. The new grid can be translated, rotated, and replicated as many times as desired. Unlike the standard starting procedure, the number of cores can be changed with this routine. To initialise the patch, the &GALAXY_DUP_PARAMS namelist has to be added. An example of the &GALAXY_DUP_PARAMS for duplicating a galaxy with a spacial separation and an initial velocity is given below.

```
 &GALAXY_DUP_PARAMS
rad_profile='exponential'
z_profile='exponential'
galaxy_repository='../merger_s1_fgas10_fb3/output_00121/'
source_gal_center=0.0,0.0,0.0
```

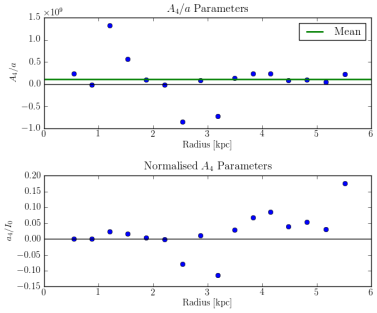

(a) Boxiness parameter as a function of the radius. The upper picture shows the A_4/a parameter where the lower picture shows the normalised A_4/I_0 parameter

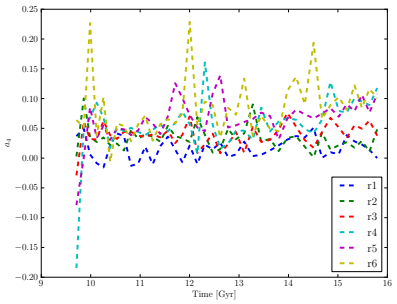

(b) Boxiness parameter as a function of time for different radii.

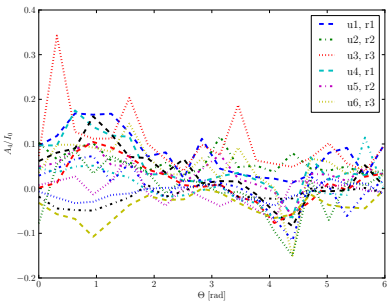

(c) Boxiness parameter as a function of different viewing angles θ as a function of u, as well as r.

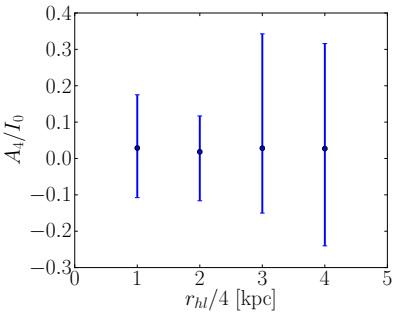

(d) Maximum and minimum boxiness parameter when changing the line-of-sight. The viewing angle was chosen uniformly over a sphere. The possible change of the boxiness parameter is shown as a function of the radius.

Figure 7.4.: Representative outputs and maps of the simulations.

```
source_gal_radius=12.0
gal_center1=0.0,75.0,0.0
gal_center2=0.0,-75.0,0.0
gal_axis1=0.0,1.0,1.504
gal_axis2=0.0,1.0,1.504
Vgal1=4.6752588471390348,-11.919618046329621,0.0
Vgal2=-4.6752588471390348,11.919618046329621,0.0
Vcirc_dat_file1='Vcirc1.dat'
Vcirc_dat_file2='Vcirc2.dat'
ic_part_file_gal1='ic_part1'
ic_part_file_gal2='ic_part2'
```

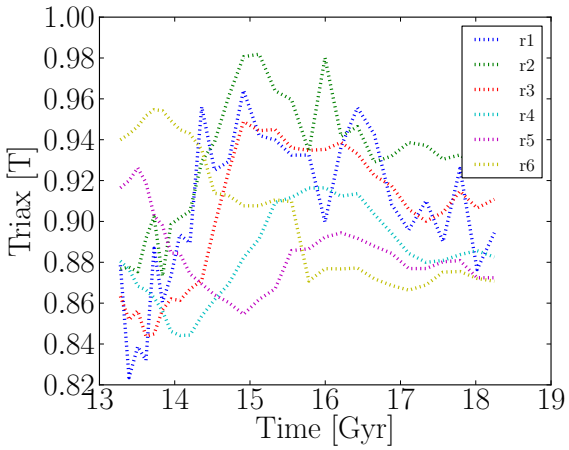

Figure 7.5.: Triaxiality parameter as a function of time for different radii.

Here, `Vgal1` (`Vgal2`) is an initial velocity added to all particles, which can also be set to zero. The specification about the size of the box size to cut out is given by `source_gal_radius`. The `ic_part_file_gal1` (`ic_part_file_gal2`) are the initial positions of the particles from the excised box. The `Vcirc_dat_file1` (`Vcirc_dat_file2`) are the circular velocities of the particles in the box which must be calculated in advance. A further possible improvement of the patch is to combine the routines generating the `Vgal1`, and `ic_part_file_gal1` files with the patch for the initial gas distribution. If one only wants to restart a certain box, the parameters `Vgal2`, `Vcirc_dat_file2`, and `ic_part_file_gal2` have to be set to zero. To compile the RAMSES code the 'Galaxy DUplication OBJects' (`GDUPOBJ`) have to be defined in the MAKEFILE

```
GDUPOBJ = amr2cube.o load_amr.o amr2cube_mem.o
```

and compiled with all the other object files

```
AMRLIB = $(AMROBJ) $(GDUPOBJ) $(HYDROOBJ) $(PMOBJ) $(POISSONOBJ)
```

A pseudo-code version of the new initial conditions is given below:

```
  ! Load amr structure at the beginning
  ! (ONLY done once per cpu)
  call load_amr(repository, ramses_struct, ...)
  ! Load hydro variables within bounds
  call amr2cube_mem(ramses_struct, input bounds, ...)
  ! Loop over given set of Mid-Points
      ! Interpolate input cube or assign analytic function
      call RTA(output cells, input cube, output bounds, centers, ...)

  ! Convert primitive to conservative variables
end subroutine condinit
```

In figure 7.6 the basic outline is also seen in a picture. The initial condition routine in RAMSES calls the subroutine INIT_FLOW_FINE which calls the subroutine CONDINIT with a set of center points (Hilbert key), the conservative variables, the grid size (dx), and the number of grid points. Within the initial condition routine of RAMSES, CONDINIT is called several times with different Hilbert keys. At the beginning of the CONDINIT subroutine, LOAD_AMR is called which loads the AMR data from disk and saves it in an `amr_structure` called `ramses_struct`. This structure contains all the important grid information to obtain the hydro variables. In the program, the input grid and the output grid variables are separated:

```
type(real_bound) :: galaxy_bnd
type(int_bound)  :: galaxy_ibnd

type(real_bound) :: amr_bnd
type(int_bound)  :: amr_ibnd
```

where `galaxy_bnd` is the box in the input grid to be extracted and `amr_bnd` are the bounds in the output grid. To cut out a simple box, as is done for calculations used for the simulations in this thesis, the `galaxy_bnd` may be the same as the `amr_bnd` (amr_bnd is always increased by dx on both sides for boundary issues when doing the smearing described later). One can also decide to run in a second way where `galaxy_bnd` is not the same as the `amr_bnd` as maybe wanted for zoom simulations.

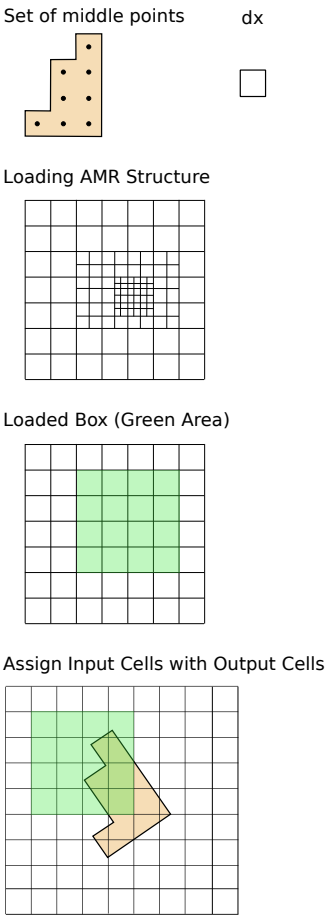

Figure 7.6.: Outline of the CONDINIT program in pictures.

After the AMR structure is loaded, the subroutine AMR2CUBE_MEM is called which extracts the hydro information within the given bounds. Note that in this version the entire cube within the bounds is extracted each time CONDINIT is called. The subroutines LOAD_AMR and AMR2CUBE_MEM are based on the program AMR2CUBE written by Romain Teyssier. The main difference is that with the new separate routines, data is only read from disk once.

Once the box is loaded it can be processed in different ways including being translated, rotated, and replicated. An example of one translated and rotated box is given below. To assign the right hydro variables to the right grid cells from the output box to the input box the subroutine RTA (**R**otate, **T**ranslate, **A**ssign) is called

```
subroutine RTA(output cells, input cube, output bounds, centers, phi,
    Axis)
    call translate(input cube,gal_centers)
    call rotate(input cube, phi, Axis)
    !Assign translated input cube to output cube and hydro variables if
        pixel is in box
```

An input and corresponding output can be seen in figure 7.7. The new patch is

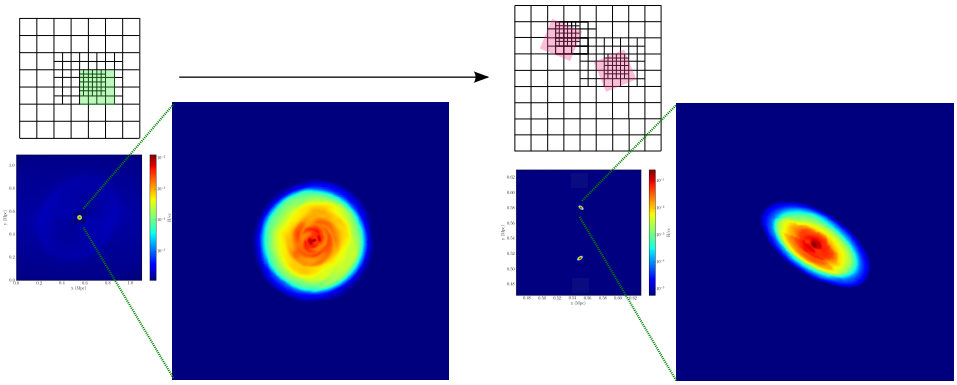

Figure 7.7.: Cut out Input box gets translated, rotated, and duplicated and set as new initial conditions for a new simulation.

currently only programmed such that the cell sizes must be the same in both the output box as well as the input box. The routine could therefore be improved to allow varying cell sizes. Another improvement for the future would be to call AMR2CUBE_MEM only once per each cell when looping over a given set of center points instead of loading the whole box each time CONDINIT is called.

8. Code Tests

In this chapter, we review a series of tests performed on each of the programs developed during this thesis. For BELLE, the boxiness recovery was tested with a fake galaxy generated with a known boxiness. The initial conditions patches were tested by comparing a Sedov 3d simulation with a restart run. We also demonstrate the ability to rotate, translate, and duplicate a region of the AMR grid. We additionally show the feature allowing a region to be extracted from the AMR grid and resimulated in isolation.

8.1. BELLE

To test the recovery of the boxiness of an input galaxy, a fake galaxy with a known boxiness was generated using the program GENMAP.PY. A test with a positive $A_4 = 10$ parameter is shown in figure 8.1, and a test with a negative $A_4 = -10$ parameter is shown in figure 8.2. In general, it can be seen that the boxiness is overestimated for small radii, but at larger radii the calculated A_4 parameter agrees better with the actual boxiness parameter. When interpreting the boxiness of the simulated galaxies one can generally assume that at large radii the calculated value has a smaller errorbar than at small radii. This is good since we particularly want to look at the boxiness parameter at large radii.

8.2. Initial conditions

8.2.1. Sedov 3d run

To test the initial conditions patches, the Sedov 3d test in RAMSES was run. First, the initial run was made from time t_i to t_e. Second, at some time $t_r \in (t_i, t_e)$ the initial run was restarted. The restart simulation was run from time t_r to t_e. The mesh information at the first output after t_r was compared with the same information from the same time from the first complete run. The last output of both simulations at time t_e were also compared. Comparing the node information from the initial run with the restart run one can see that it is possible to change the number of nodes when restarting the simulation. Comparing the mesh structure at the time of restart t_r in the initial run and the restart run at t_r one can see small deviations. These deviations can be explained with the slightly different time stepping between the two runs. Comparing the mesh structure of the initial run at time t_e of the simulation with the mesh structure at time t_e of the restart run one can again see some deviations.

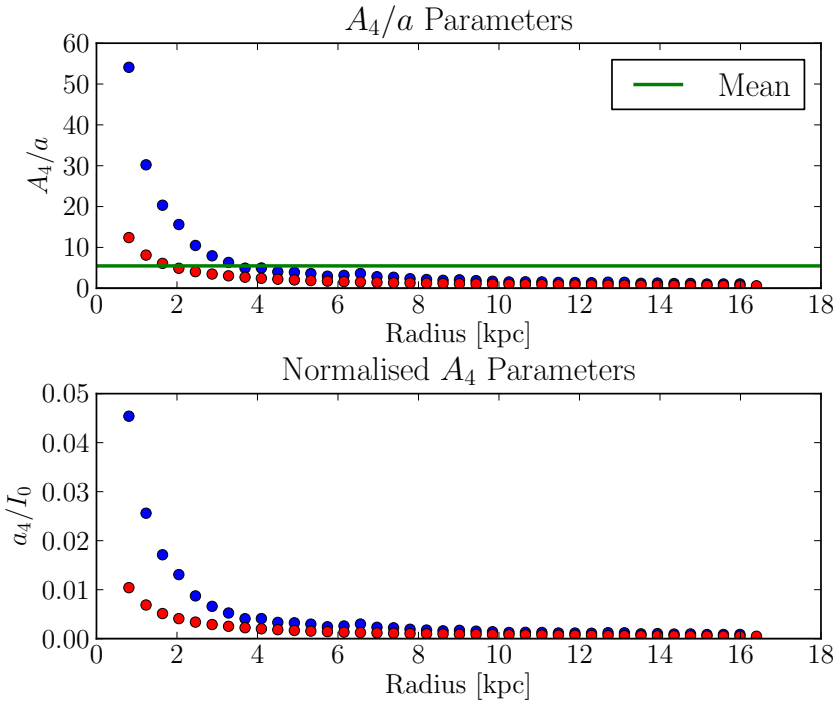

Figure 8.1.: Test of the boxiness analysis with a positive A_4 parameter. In both pictures the blue dots are the calculated parameters whereas in the upper picture the red dots are the actual values and in the lower picture the green line is the actual boxiness parameter.

These can be explained with the slight deviations at the beginning of the run. However, it is important to note that the differences do not start to deviate from each other and that the two mesh structures at time t_e still are comparable with each other. In figure 8.3 one can see the first output after time t_e of the initial run and the restart run. Looking closely at the grid structure one can see some minor deviations. A similar situation arises when looking at the last outputs at time t_e of the initial run as well as the restart run. Looking at the level map as well as the temperature map in figure 8.3, however, one can hardly see any deviations.

Initial Run

Node information

```
#!/bin/bash
#SBATCH -t 1-0:00:00 --mem=64000
#SBATCH --ntasks=64
#SBATCH --ntasks-per-node=4
```

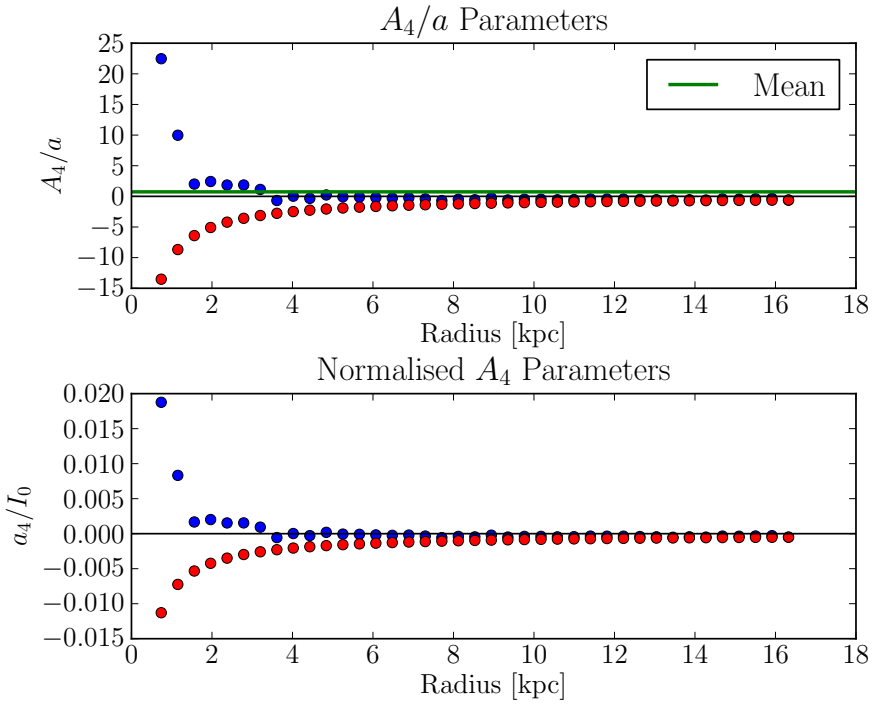

Figure 8.2.: Test of the boxiness analysis with a negative A_4 parameter. In both pictures the blue dots are the calculated parameters whereas in the upper picture the red dots are the actual values and in the lower picture the green line is the actual boxiness parameter.

Grid information

```
&AMR_PARAMS
levelmin=4
levelmax=8
ngridmax=1000000
npartmax=2000000
ngridtot=3000000
nexpand=1
boxlen=0.5
/
```

Restart Run

Node information

```
#!/bin/bash
#SBATCH -t 1-0:00:00 --mem=64000
```

```
#SBATCH --ntasks=32
#SBATCH --ntasks-per-node=2
```

Grid and Box information

```
&AMR_PARAMS
levelmin=4
levelmax=8
ngridmax=1000000
npartmax=2000000
ngridtot=3000000
nexpand=1
boxlen=0.5
/

&GALAXY_DUP_PARAMS
rad_profile='exponential'
z_profile='exponential'
galaxy_repository='/zbox/data/rbieri/MASTERTHESIS/condinit_test/sedov/
    output_00025/'
source_gal_center=0.0,0.0,0.0
source_gal_radius=0.25
gal_center1=0.0,0.0,0.0
gal_center2=0.0,0.0,0.0
gal_axis1=0.0,0.0,1.0
gal_axis2=0.0,0.0,1.0
Vgal1=0.0,0.0,0.0
Vgal2=0.0,0.0,0.0
Vcirc_dat_file1='Vcirc1.dat'
Vcirc_dat_file2='Vcirc2.dat'
ic_part_file_gal1='ic_part1'
ic_part_file_gal2='ic_part2'
/
```

Comparison between Initial run and Restart run

Mesh structure of the initial run at the time the simulation got restarted t_r.

```
 Load balancing AMR grid...
 Mesh structure
 Level    1 has           1 grids (        0,        1,        0,)
 Level    2 has           8 grids (        0,        1,        0,)
 Level    3 has          64 grids (        0,        3,        1,)
 Level    4 has         512 grids (        3,       15,        8,)
 Level    5 has        4096 grids (       29,      116,       64,)
 Level    6 has       32672 grids (      235,      928,      510,)
 Level    7 has      215247 grids (     1883,     5328,     3363,)
 Level    8 has      472063 grids (     4941,     9170,     7375,)
 Main step=  2940 mcons=-4.44E-16 econs=-1.33E-15 epot= 0.00E+00 ekin=
     1.25E-01
 Fine step=  2940 t= 4.89527E-01 dt= 1.607E-04 a= 1.000E+00 mem= 1.8%
 Time elapsed since last coarse step:  0.74289202690124512
 Used memory:    1.2 Gb
```

Mesh structure at the beginning of the restarted run at time t_r

```
Initial mesh structure
Level  1 has           1 grids (        0,       1,       0,)
Level  2 has           8 grids (        0,       1,       0,)
Level  3 has          64 grids (        1,       4,       2,)
Level  4 has         512 grids (       11,      25,      16,)
Level  5 has        4096 grids (       89,     197,     128,)
Level  6 has       32672 grids (      711,    1571,    1021,)
Level  7 has      215085 grids (     5380,    9946,    6721,)
Level  8 has      472063 grids (    10907,   16353,   14751,)
Starting time integration
Load balancing AMR grid...
Fine step=      0 t= 0.00000E+00 dt= 1.607E-04 a= 1.000E+00 mem= 3.5%
```

Mesh structure at the initial run at the end of the simulation t_e.

```
Mesh structure
Level  1 has           1 grids (        0,       1,       0,)
Level  2 has           8 grids (        0,       1,       0,)
Level  3 has          64 grids (        0,       4,       1,)
Level  4 has         512 grids (        2,      26,       8,)
Level  5 has        4096 grids (       15,     207,      64,)
Level  6 has       27850 grids (      119,    1273,     435,)
Level  7 has       86887 grids (      931,    1994,    1357,)
Level  8 has      178146 grids (     1237,    3583,    2783,)
Main step=  4690 mcons= 2.22E-16 econs=-1.44E-15 epot= 0.00E+00 ekin=
    1.25E-01
Fine step=  4690 t= 9.95978E-01 dt= 5.488E-04 a= 1.000E+00 mem= 0.9%
```

Mesh structure at the restart run at the end of the simulation t_e.

```
Mesh structure
Level  1 has           1 grids (        0,       1,       0,)
Level  2 has           8 grids (        0,       1,       0,)
Level  3 has          64 grids (        0,       5,       2,)
Level  4 has         512 grids (        4,      39,      16,)
Level  5 has        4096 grids (       34,     310,     128,)
Level  6 has       27850 grids (      276,    1908,     870,)
Level  7 has       86887 grids (     2176,    3421,    2715,)
Level  8 has      178153 grids (     3615,    6807,    5567,)
Main step=  1750 mcons= 2.22E-16 econs= 4.44E-16 epot= 0.00E+00 ekin=
    1.25E-01
Fine step=  1750 t= 5.06451E-01 dt= 5.488E-04 a= 1.000E+00 mem= 1.5%
Time elapsed since last coarse step:  0.63109993934631348
Used memory:    1.1 Gb
```

8.2.2. Translation, Rotation, and Duplication

In figure 8.5 an example of a translation, rotation and duplication of a galaxy is shown.

8.2.3. Zoom into a Cosmo Run

An output from Davide Martizzi's cosmology run was taken and zoomed in to check whether such a process is in principle feasible. The full picture as well as the zoomed in version can be seen in figure 8.6.

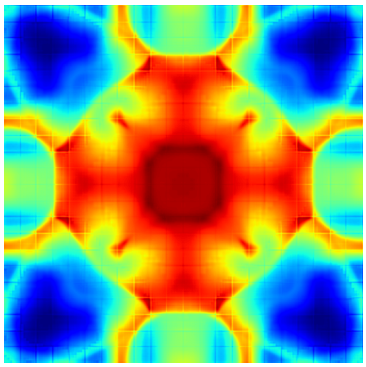

(a) First output after time t_r of the initial run, boxlen=0.5

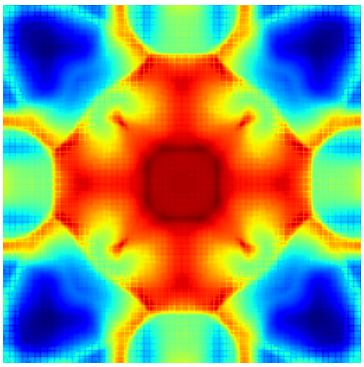

(b) First output of the restart run after time t_r, boxlen=0.5

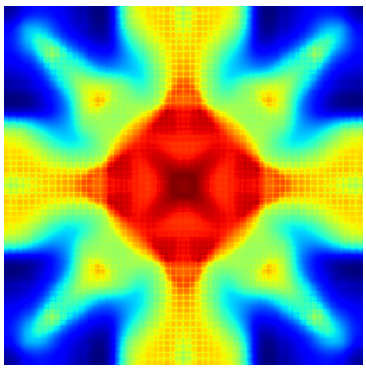

(c) Last output of the initial run at time t_e, boxlen=0.5

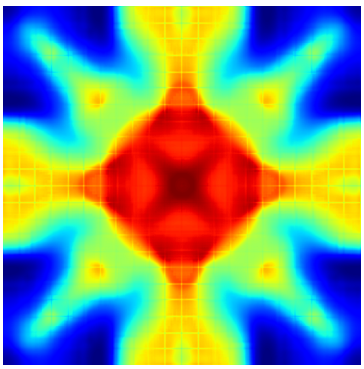

(d) Last output of the restart run at time t_e, boxlen=0.5

Figure 8.3.: Represantive outputs of the initial run and the restart run at time t_r, and t_e.

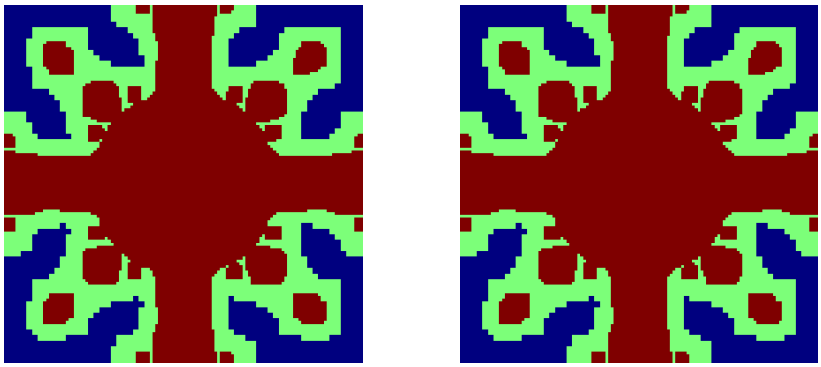

(a) Level map of the initial run at time t_r, boxlen=0.5

(b) Level of the restart run at time t_r, boxlen=0.5

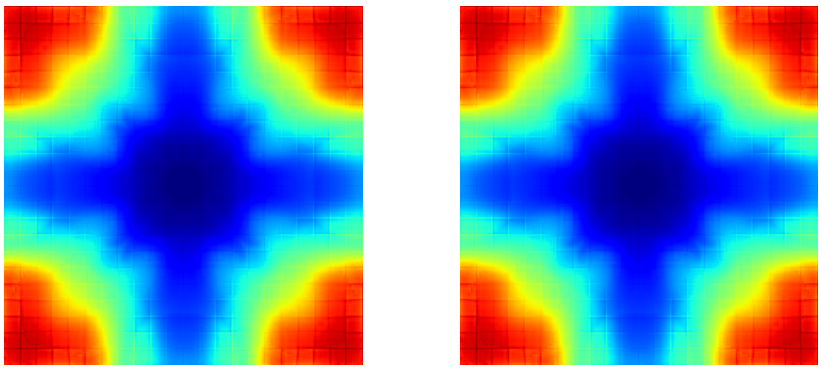

(c) Temperature map of the initial run at time t_r, boxlen=0.5

(d) Temperature map of the restart run at time t_r, boxlen=0.5

Figure 8.4.: Represantive level and temperature maps of the initial run and the restart run at time t_r.

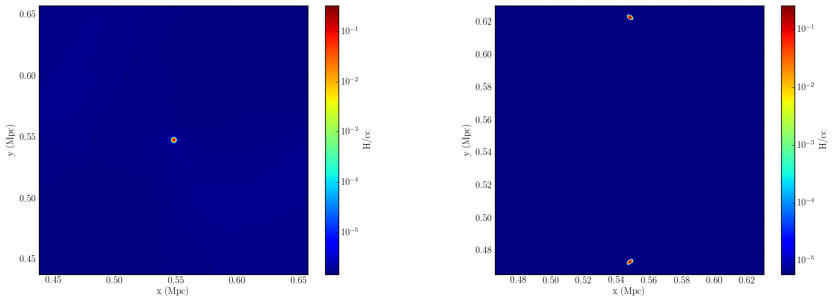

(a) Initial Output from which a box was cut out containing the galaxy.

(b) Restart where the cut out box got translated, rotated, and duplicated during the new initial condition process.

Figure 8.5.: A translation, rotation, and duplication of a cut out box. The initial output can be seen as well as the new initial condition after the translation, rotation, and duplication.

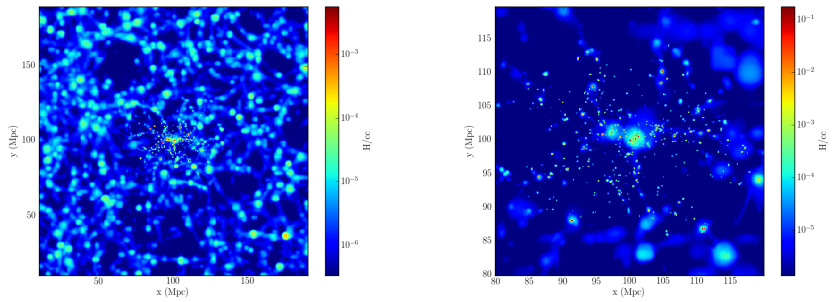

(a) Initial Output from the cosmo run.

(b) Restart where a smaller box was cut out and put into as a new restart.

Figure 8.6.: A zoom in example of the initial condition routine. The initial output can be seen as well as the new initial condition after the zooming.

9. Conclusion

Motivated by the observation of LEDA 074886 (Graham et al., 2012) a number of simulations have been performed to better understand the possible formation scenario. Merger simulations have been performed with a varying gas fraction of 10%, 15%, and 20% as well as with rotation axes pointing in the same and opposite directions. The detailed discussion about the individual simulations can be read in the chapter.

Generally speaking, the merger remnants of two galaxies with rotation axis pointing opposite to each other show more fluctuations in the A_4/I_0 parameters indicating that those galaxies are less relaxed as the remnants calculated with rotation axis pointing in the same direction. They are also observed to be more disky in appearance when comparing them with the simulations with rotation axis pointing in the same direction. An exception of this trend is in the simulation performed with the new initial condition code. Two merger remnants from a previous feedback run were merged together with rotation axis pointing in the same as well as opposite direction. The remnants from those simulations both result in an elliptical galaxy where only one significant difference between the two simulations can be observed: The triaxiality parameter for the dark matter halo surrounding the galaxies of the simulation with the two rotation axis pointing opposite of each other shows a triaxial dark matter distribution whereas the triaxiality parameter of the simulation with the rotation axis pointing in the same direction show a prolate dark matter distribution.

We also tested the assumption of Jesseit et al. (2005) regarding different viewing angles. We observed that, unlike their claim, the line-of-sight along the principal axes does not always show the most extreme cases of the boxiness A_4 parameters. In fact, the boxiness parameter can vary significantly when looking at the galaxy from different angles. Generally a negative A_4 coefficient can be found for the majority of the merger remnants. It is, however, noteworthy that most of the resulting remnants did not show the desired features of a discy inner region and a boxy outer part even when varying the different viewing angles. Unlike other authors (e.g., Jesseit et al., 2005) a significant change between the different gas fractions was not observed with the simulations presented here.

There is, however, one specific example where the analysis has shown a discy inner region with a boxy outer part. This remnant resulted from the simulation of a feedback run with a gas fraction of 10% and the two rotation axes pointing in the same direction. Given the similar properties analysed for LEDA 074886 and the simulated galaxy we can assume that merging two galaxies with a low mass fraction and rotation axis pointing in the same direction could have led to the formation of LEDA 074886. The simulations leading to the formation of a rectangular galaxy were performed with a feedback mechanism and it can be assumed that this feedback mechanism played an important role in the formation of the rectangular merger remnant. The exact

influence however still has to be studied in further detail. When observing the halo structure of the dark matter particles around the galaxy one notices a slightly triaxial halo at the time the two galaxies merged. This barely triaxial halo can be understood to support the building of the boxy galaxy. Whereas the prolate halo observed in the middle phase might be responsible for the stability also observed of the galaxy. Further analysis to test this hypothesis again has to be carried out in more detail.

Appendices

A. Sphere Point Picking

To uniformly pick points such that the sphere is uniformly distributed is has to be with $U \in (0.1)$ and $V \in (0.1)$:

$$\theta = 2\pi u \tag{A.1}$$
$$\phi = \cos^{-1}(2v - 1) \tag{A.2}$$

This gives the spherical coordinated for a set of points which are uniformly distributed over S^2. It is such since the differential element of the solid angle is given by

$$d\Omega = \sin\phi d\theta d\phi = -d\theta d(\cos\phi)$$

The distribution P_ϕ of polar angles can be found from

$$P_\phi d\phi = P_\nu \left| \frac{d\nu}{d\phi} \right| d\phi \tag{A.3}$$

by taking the derivative of A.2 with respect to ν and solving it for ν and plugging the result into equation A.3 with $P_\nu = 1$ to finally obtain the distribution

$$P_\phi = \frac{1}{2}\sin\phi$$

By substitution of $u = \cos\phi$ to be uniformly distributed (from which wwe have $ddu = \sin\phi d\phi$ one obtains the poins

$$x = \sqrt{1-u^2}\cos\theta \tag{A.4}$$
$$y = \sqrt{1-u^2}\sin\theta \tag{A.5}$$
$$z = u \tag{A.6}$$

with $\theta \in [0, 2\phi)$ and $u \in [-1, 1]$ which also is uniformly distributed over S^2.

B. PYMSES routines

Here is an example of how to generate a gas map with PYMSES from an RAMSES output.

```
#This line must come before other matplotlib (pylab) imports
from __future__ import division
from matplotlib import rc
import numpy as np
import pylab as pl
import scipy as sc
import scipy.fftpack
from math import atan2
import math
import numpy
import sys
from os import path
import pymses
from pymses.analysis.visualization import *
from pymses import RamsesOutput
from pymses.utils import constants as C
import os.path

#import pyfits as pf

rc('text', usetex=True)
rc('font', **{'family':'serif','serif':['Computer Modern Roman']})

# Ramses data
fname = sys.argv[1]
print >>sys.stderr, 'Reading Data of',sys.argv[1]
#ioutput = raw_input("Enter output: ")
ioutput = sys.argv[2]
ioutput = int(ioutput)
ro = RamsesOutput(fname, ioutput)
amr = ro.amr_source(["rho", "P"])
xc = float(sys.argv[3])
yc = float(sys.argv[4])
zc = float(sys.argv[5])
ax = float(sys.argv[6])
ay = float(sys.argv[7])
az = float(sys.argv[8])
up_vector=sys.argv[9]
rs1 = float(sys.argv[10])
rs2 = float(sys.argv[11])
print rs1, rs2

fname = os.path.split(os.path.normpath(fname))[-1]

# Map operator : mass-weighted density map
```

```
up_func = lambda dset: (dset["rho"]**2 * dset.get_sizes()**3)
down_func = lambda dset: (dset["rho"] * dset.get_sizes()**3)
scal_func = FractionOperator(up_func, down_func)

# Map region
center = [xc, yc, zc ]
axes = {"los": np.array([ ax, ay, az ])}

# Map processing
mp = fft_projection.MapFFTProcessor(amr, ro.info)
for axname, axis in axes.items():
        cam  = Camera(center=center, line_of_sight_axis=axis, up_vector=
            up_vector, region_size=[rs1, rs2],  map_max_size=512)
        map = mp.process(scal_func, cam, multiprocessing=False)
        factor = ro.info["unit_density"].express(C.H_cc)
        scale = ro.info["unit_length"].express(C.Mpc)

        #pl.imshow(map)
        #pl.xlabel('x')
        #pl.ylabel('y' )

        #Save map into HDF5 file
        mapname = "gas_density_%s_out%03i_ax%03i_ay%03i_az%03i_rs1%04
            i_rs2%04i_uv%s"%(fname, ioutput, ax, ay, az, rs1*1000, rs2
            *1000, up_vector)
        h5fname = save_map_HDF5(map, cam, map_name=mapname)

        #Save map in txt file
        with open('mapNames.dat','a') as myfile:
            myfile.write(mapname+'\n')
        np.savetxt(mapname, map)

        # Plot map into Matplotlib figure/PIL Image
        fig = save_HDF5_to_plot(h5fname, map_unit=("H/cc",factor),
            axis_unit=("Mpc", scale), cmap="jet")

print >>sys.stderr, mapname
fig.savefig(mapname)
#pl.show()
```

Where here is an example of how to generate a stellar distribution map as well as a dark matter distribution map with PYMSES from a RAMSES output.

```
 #This line must come before other matplotlib (pylab) imports
#from __future__ import division
#from matplotlib import rc
from numpy import array, log10
import numpy as np
import pylab as pl
import scipy as sc
from pymses.analysis.visualization import *
from pymses import RamsesOutput
from pymses.utils import constants as C
import sys
import os.path

#rc('text', usetex=True)
```

```
#rc('font', **{'family':'serif','serif':['Computer Modern Roman']})

# Ramses data
fname = sys.argv[1]
print >>sys.stderr, 'Reading Data of',sys.argv[1]
#ioutput = raw_input("Enter output: ")
ioutput = sys.argv[2]
ioutput = int(ioutput)
ro = RamsesOutput(fname, ioutput)
parts = ro.particle_source(["mass", "level","epoch"])
mass_cut = 3.1E-06
xc = float(sys.argv[3])
yc = float(sys.argv[4])
zc = float(sys.argv[5])
ax = float(sys.argv[6])
ay = float(sys.argv[7])
az = float(sys.argv[8])
up_vector=sys.argv[9]
rs1 = float(sys.argv[10])
rs2 = float(sys.argv[11])

fname = os.path.split(os.path.normpath(fname))[-1]


# Map operator : mass
scal_func_s  = ScalarOperator(lambda dset: dset["mass"] * (dset["epoch"]
    > 0.0)+dset["mass"]<mass_cut)
scal_func_dm = ScalarOperator(lambda dset: dset["mass"] > mass_cut)

# Map region
center = [xc, yc, zc ]
axes = {"los": np.array([ ax, ay, az ])}

mp = fft_projection.MapFFTProcessor(parts, ro.info)

if 1:
    for axname, axis in axes.items():
        cam  = Camera(center=center, line_of_sight_axis=axis, up_vector=
            up_vector, region_size=[rs1, rs2], \
                    distance=2.0E-1, far_cut_depth=2.0E-1,
                        map_max_size=512)
        map_s  = mp.process(scal_func_s, cam, surf_qty=True)
        map_dm = mp.process(scal_func_dm, cam, surf_qty=True)
        print('type(ro.info["unit_length"]',ro.info["unit_length"])
        print('type(ro.info["unit_mass"]',ro.info["unit_mass"])
        factor = (ro.info["unit_mass"]/ro.info["unit_length"]**2).express
            (C.Msun/C.kpc**2)
        scale = ro.info["unit_length"].express(C.Mpc)

        # Save map into HDF5 file
        mapname_s  = "star_density_%s_out%03i_ax%03i_ay%03i_az%03i_rs1%03
            i_rs2%03i_uv%s"%(fname, ioutput, ax, ay, az, rs1*100, rs2
            *100, up_vector)
        mapname_dm = "darkMatter_density_%s_out%03i_ax%03i_ay%03i_az%03
            i_rs1%03i_rs2%03i_uv%s"%(fname, ioutput, ax, ay, az, rs1*100,
             rs2*100, up_vector)
```

```
    h5fname_s  = save_map_HDF5(map_s,  cam, map_name=mapname_s)
    h5fname_dm = save_map_HDF5(map_dm, cam, map_name=mapname_dm)

    # Plot map into Matplotlib figure/PIL Image
    fig_s  = save_HDF5_to_plot(h5fname_s,  map_unit=("$M_{\odot}.kpc
        ^{-2}$",factor), axis_unit=("Mpc", scale), cmap="jet")
    fig_dm = save_HDF5_to_plot(h5fname_dm, map_unit=("$M_{\odot}.kpc
        ^{-2}$",factor), axis_unit=("Mpc", scale), cmap="jet")

fig_s.savefig(mapname_s)
fig_dm.savefig(mapname_dm)
```

Bibliography

Agertz O. et al., 2007, MNRAS, 380, 963

Barnes J., Efstathiou G., 1987, ApJ, 319, 575

Barnes J. E., 1992, ApJ, 393, 484

Barnes J. E., Hernquist L., 1992, ARA&A, 30, 705

Barnes J. E., Hernquist L., 1996, ApJ, 471, 115

Bertschinger E., 1998, ARA&A, 36, 599

Binney J., Tremaine S., 2008, Galactic Dynamics: Second Edition. Princeton University Press

Bond J. R., Cole S., Efstathiou G., Kaiser N., 1991, ApJ, 379, 440

Bullock J. S., Kolatt T. S., Sigad Y., Somerville R. S., Kravtsov A. V., Klypin A. A., Primack J. R., Dekel A., 2001, MNRAS, 321, 559

Burkert A., Naab T., 2004, Coevolution of Black Holes and Galaxies, 421

Cole S., Lacey C., 1996, MNRAS, 281, 716

Coles P., Melott A. L., Shandarin S. F., 1993, MNRAS, 260, 765

Debattista V. P., Moore B., Quinn T., Kazantzidis S., Maas R., Mayer L., Read J., Stadel J., 2008, ApJ, 681, 1076

Dehnen W., 2001, MNRAS, 324, 273

Doroshkevich A. G., Kotok E. V., Poliudov A. N., Shandarin S. F., Sigov I. S., Novikov I. D., 1980, MNRAS, 192, 321

Dubinski J., 1998, ApJ, 502, 141

Dubinski J., Carlberg R. G., 1991, ApJ, 378, 496

Dubois Y., Devriendt J., Slyz A., Teyssier R., 2012, in Astronomical Society of the Pacific Conference Series, Vol. 453, Advances in Computational Astrophysics: Methods, Tools, and Outcome, Capuzzo-Dolcetta R., Limongi M., Tornambè A., eds., p. 281

Dubois Y., Teyssier R., 2008a, A&A, 482, L13

Dubois Y., Teyssier R., 2008b, A&A, 477, 79

Dubois Y., Teyssier R., 2008c, in Astronomical Society of the Pacific Conference Series, Vol. 390, Pathways Through an Eclectic Universe, Knapen J. H., Mahoney T. J., Vazdekis A., eds., p. 388

Einasto J., 1965, Trudy Astrofizicheskogo Instituta Alma-Ata, 5, 87

Eke V. R., Navarro J. F., Steinmetz M., 2001, ApJ, 554, 114

Franx M., 1988, MNRAS, 231, 285

Frenk C. S., White S. D. M., Davis M., Efstathiou G., 1988, ApJ, 327, 507

Fulton E., Barnes J. E., 2001, Ap&SS, 276, 851

Gao L., Navarro J. F., Cole S., Frenk C. S., White S. D. M., Springel V., Jenkins A., Neto A. F., 2008, MNRAS, 387, 536

Gerhard O. E., 1981, MNRAS, 197, 179

Gerin M., Combes F., Athanassoula E., 1990, A&A, 230, 37

Gingold R. A., Monaghan J. J., 1977, MNRAS, 181, 375

Gnedin O. Y., 2003, ApJ, 582, 141

Graham A. W., Spitler L. R., Forbes D. A., Lisker T., Moore B., Janz J., 2012, ApJ, 750, 121

Gunn J. E., Gott, III J. R., 1972, ApJ, 176, 1

Hao C. N., Mao S., Deng Z. G., Xia X. Y., Wu H., 2006, MNRAS, 370, 1339

Hernquist L., 1992, ApJ, 400, 460

Hernquist L., 1993, ApJS, 86, 389

Heyl J. S., Hernquist L., Spergel D. N., 1994, ApJ, 427, 165

Hoffman L., Cox T. J., Dutta S., Hernquist L., 2010, ApJ, 723, 818

Hubble E. P., 1926, ApJ, 64, 321

Janz J., Lisker T., 2008, ApJ, 689, L25

Jeans J. H., 1902, Royal Society of London Philosophical Transactions Series A, 199, 1

Jenkins A., Frenk C. S., White S. D. M., Colberg J. M., Cole S., Evrard A. E., Couchman H. M. P., Yoshida N., 2001, MNRAS, 321, 372

Jesseit R., Naab T., Burkert A., 2005, MNRAS, 360, 1185

Jing Y. P., Suto Y., 2002, ApJ, 574, 538

Kazantzidis S., Kravtsov A. V., Zentner A. R., Allgood B., Nagai D., Moore B., 2004a, ApJ, 611, L73

Kazantzidis S., Magorrian J., Moore B., 2004b, ApJ, 601, 37

Kereš D., Vogelsberger M., Sijacki D., Springel V., Hernquist L., 2012, MNRAS, 425, 2027

Khokhlov A., 1998, Journal of Computational Physics, 143, 519

Klypin A., Ceverino D., Tinker J., 2008, in Reviews in Modern Astronomy, Vol. 20, Reviews in Modern Astronomy, Röser S., ed., p. 64

Kravtsov A. V., Klypin A. A., Khokhlov A. M., 1997, ApJS, 111, 73

Liu F. S., Xia X. Y., Mao S., Wu H., Deng Z. G., 2008, MNRAS, 385, 23

Łokas E. L., Kazantzidis S., Klimentowski J., Mayer L., Callegari S., 2010, ApJ, 708, 1032

Lucy L. B., 1977, AJ, 82, 1013

Mayer L., Governato F., Colpi M., Moore B., Quinn T., Wadsley J., Stadel J., Lake G., 2001a, ApJ, 559, 754

Mayer L., Governato F., Colpi M., Moore B., Quinn T., Wadsley J., Stadel J., Lake G., 2001b, ApJ, 547, L123

Mayer L., Kazantzidis S., Mastropietro C., Wadsley J., 2007, Nature, 445, 738

Merritt D., Fridman T., 1996, ApJ, 460, 136

Merritt D., Navarro J. F., Ludlow A., Jenkins A., 2005, ApJ, 624, L85

Miyazaki S. et al., 2002, ApJ, 580, L97

Moore B., Calcáneo-Roldán C., Stadel J., Quinn T., Lake G., Ghigna S., Governato F., 2001, Phys. Rev. D, 64, 063508

Moore B., Ghigna S., Governato F., Lake G., Quinn T., Stadel J., Tozzi P., 1999, ApJ, 524, L19

Moore B., Katz N., Lake G., 1996a, ApJ, 457, 455

Moore B., Katz N., Lake G., Dressler A., Oemler A., 1996b, Nature, 379, 613

Moore B., Kazantzidis S., Diemand J., Stadel J., 2004, MNRAS, 354, 522

Moore B., Lake G., Katz N., 1998, ApJ, 495, 139

Moster B. P., Macciò A. V., Somerville R. S., Naab T., Cox T. J., 2011, MNRAS, 415, 3750

Naab T., Burkert A., 2003, ApJ, 597, 893

Naab T., Jesseit R., Burkert A., 2006a, MNRAS, 372, 839

Naab T., Khochfar S., Burkert A., 2006b, ApJ, 636, L81

Navarro J. F., Frenk C. S., White S. D. M., 1996, ApJ, 462, 563

Navarro J. F., Frenk C. S., White S. D. M., 1997, ApJ, 490, 493

Navarro J. F. et al., 2004, MNRAS, 349, 1039

Noguchi M., 1988, A&A, 203, 259

Nulsen P. E. J., 1982, MNRAS, 198, 1007

Prada F., Klypin A. A., Simonneau E., Betancort-Rijo J., Patiri S., Gottlöber S., Sanchez-Conde M. A., 2006, ApJ, 645, 1001

Press W. H., Schechter P., 1974, ApJ, 187, 425

Prugniel P., Simien F., 1997, A&A, 321, 111

Rampf C., Buchert T., 2012, JCAP, 6, 21

Read J. I., Hayfield T., 2012, MNRAS, 422, 3037

Read J. I., Wilkinson M. I., Evans N. W., Gilmore G., Kleyna J. T., 2006, MNRAS, 366, 429

Reed D., Gardner J., Quinn T., Stadel J., Fardal M., Lake G., Governato F., 2003, MNRAS, 346, 565

Rigopoulos G., Valkenburg W., 2012, Phys. Rev. D, 86, 043523

Scannapieco C., 2013, Astronomische Nachrichten, 334, 499

Scannapieco C. et al., 2012, MNRAS, 423, 1726

Seljak U., Zaldarriaga M., 1996, ApJ, 469, 437

Sheth R. K., Tormen G., 1999, MNRAS, 308, 119

Somerville R. S., Hopkins P. F., Cox T. J., Robertson B. E., Hernquist L., 2008, MNRAS, 391, 481

Springel V., 2010, MNRAS, 401, 791

Springel V., 2011, ArXiv e-prints

Springel V., Hernquist L., 2005, ApJ, 622, L9

Stadel J., Potter D., Moore B., Diemand J., Madau P., Zemp M., Kuhlen M., Quilis V., 2009, MNRAS, 398, L21

Sutherland R. S., Dopita M. A., 1993, ApJS, 88, 253

Teyssier R., 2002, A&A, 385, 337

Teyssier R., Pontzen A., Dubois Y., Read J. I., 2013, MNRAS, 429, 3068

Thomas P. A. et al., 1998, MNRAS, 296, 1061

Toomre A., Toomre J., 1972, ApJ, 178, 623

Tormen G., Diaferio A., Syer D., 1998, MNRAS, 299, 728

Vitvitska M., Klypin A. A., Kravtsov A. V., Wechsler R. H., Primack J. R., Bullock J. S., 2002, ApJ, 581, 799

Warren M. S., Quinn P. J., Salmon J. K., Zurek W. H., 1992, ApJ, 399, 405

Wechsler R. H., Bullock J. S., Primack J. R., Kravtsov A. V., Dekel A., 2002, ApJ, 568, 52

Weil M. L., Hernquist L., 1996, ApJ, 460, 101

White S. D. M., 1978, MNRAS, 184, 185

White S. D. M., Rees M. J., 1978, MNRAS, 183, 341

Zel'dovich Y. B., 1970, A&A, 5, 84

Zhao D. H., Jing Y. P., Mo H. J., Börner G., 2009, ApJ, 707, 354